TEMPLATE-ASSISTED ELECTRODEPOSITED NANOWIRES AND THEIR APPLICATIONS

A DISSERTATION

SUBMITTED TO THE FACULTY OF

THE UNIVERSITY OF MINNESOTA

BY

Joseph Um

IN PARTIAL FULFILLMENT OF THE REQUIREMENTS

FOR THE DEGREE OF

DOCTOR OF PHILOSOPHY

Bethanie J. H. Stadler, Advisor

June 2021

Acknowledgments

First and foremost, praise and thanks go to my Savior Jesus Christ for all the blessings and protection all through my life.

I would not have been able to complete this work without the people who supported and inspired me during my PhD at UMN.

I would like to express my most sincere appreciation to my advisor, Prof. Bethanie Stadler, for her invaluable and admirable patience, guidance, and support. I have learned a lot, both academically and personally, from her dedication and keen interest to help her students.

I would like to thank Prof. Rhonda Franklin for her guidance and mentoring. It has been a great pleasure and experience working closely with her research group. I also would like to thank my dissertation committee members, Prof. Valerie Pierre and Prof. Jeong-Hyun Cho for their helpful suggestions and discussion.

I am also indebted to my master's advisor, Prof. Sarah Eunkyung Kim at Seoul National University of Science and Technology, for stimulating my research interests in the semiconductor field and encouraging me to complete my PhD.

I appreciate all the contributions from the past and present members of the Stadler group, Dr. Daniel Shore, Dr. Sang-Yeob Sung, Dr. Karthik Srinivasan, Dr. Reza Zamani, Dr. Zohreh Nemati, and Dr. Javier Alonso. Good luck to junior students, Allison Harpel, Andrew Schwarz, and Yicong Chen. I am especially grateful to the Franklin group members, Yali Zhang and Wen Zhou, for their helpful discussions and interactive collaboration. I am also thankful to my colleagues, Dr. Wei-Heng Hsu and Aneesh Venugopal, for sharing their hands, ideas, and conversations on various topics during my studies.

Special thanks to the True Light of the Lord Church community for their love and help.

I thank my parents Ok-Sun and Seong-Jong, sister Hanna, and her family for their lifelong love, support, and encouragement. With all my love, I thank my beloved wife Goeun, my son Daniel, and the baby growing well in Goeun's belly for their support and patience in the good or hard times during my PhD. No words can express my deepest gratitude to them.

Dedication

To my parents and sister,

to my beloved wife Goeun,

and to my son Daniel and the baby in Goeun's belly.

Abstract

Nanowires (NWs), cylindrical-shaped nanostructures with nanometer-scale diameters and nano- and micrometer-scale lengths, have gathered great attention from a variety of fields for their unique material properties coming from their high length to diameter ratios, high surface to volume ratios, and nanometer-sized features. In addition, as the demand for increasingly smaller electronic devices grows, the production of small circuits will also be required. In achieving this and accelerating the advancement of electronics, NW-based designs have great potential as a field.

NWs can be fabricated via template-assisted electrochemical deposition with adjustable diameters and lengths, allowing them to have special properties for specific applications. Template-assisted electrodeposition is a relatively simple, efficient, convenient, and cost-effective technique to make nanomaterials and nanodevices, compared to lithographic techniques, since it is fast and does not require any special equipment. The templates used in this dissertation are mainly nanoporous anodic aluminum oxide (AAO). AAO templates can also directly affect the properties or performance of nanomaterials and nanodevices made from them due to their structural features.

In this dissertation, fabrication processes of AAO and NWs, application-driven magnetic properties of magnetic NWs, and several NW-based applications (e.g., magnetic NW biolabeling system by ferromagnetic resonance, AAO and NW fabrication for 3-D memory, NW-based interconnects) are explored. This research shows how NWs were fabricated, engineered, applied, and analyzed.

In particular, for the magnetic NW biolabeling system, ferromagnetic resonance identification (FMR-ID) was developed and optimized. This magnetic NW-based FMR-ID labeling system appears to be effective wherever small identification markers are needed. Also,

for future 3-D memory, simple and cost-effective double imprinting method for AAO with ordered pores and uniform Fe/Au multilayered NWs were investigated. Methods to grow NWs using small pore AAO templates and to characterize the NW array embedded in the AAO using scanning electron microscopy were also covered. Furthermore, for NW-based interconnects as the next-generation interconnects lowering power loss and RC delays, a method to integrate AAO on Si was studied and the electrical resistivity of Cu NWs in AAO on Si was estimated via DC resistance measurement. A trend of the experimental Cu NW resistivity with diameter size was introduced as well.

The proven applications of nanowires in this research show the potential of nanowires as the essential materials in future nanotechnology.

Table of Contents

List of Tables

List of Figures

Chapter 2

Chapter 3

Chapter 4

Chapter 5

Chapter 6

Chapter 1

Introduction

Nanoparticles (NPs) have emerged as important players in modern medicine, with clinical applications ranging from contrast agents in imaging to carriers for drug and gene delivery into tumors. It is estimated that the global nanoparticle drug market will reach over US $ 200 Billion by 2024 at a compound annual growth rate (CAGR) of 10%.[1] On the other hand, there is no nanowire (NW)-based medical market yet. However, many researchers, particularly those in biomedical-related fields, have shown their interest in NWs because they have several advantages over NPs of comparable volume. First, NWs have a higher surface to volume ratio per particle, which enables the loading of more coatings for drug delivery.[2,3] Second, multiple functionalities are possible with multilayered NWs with "barcoded" surface chemistries.[4] Third, magnetic NWs can be mechanically rotated for torque-induced dynamic cell therapy using a relatively weak external field due to the larger magnetic moment and higher aspect ratio.[2,3,5,6] In the near future, NWs and related nanotechnologies with those advantages could be used to prolong human life expectancy.

In addition, 3-D NAND flash memories have recently garnered significant attention as a solution to the limited storage capacity of hard disk drives and solid-state devices with 2-D device paradigm as the International Roadmap for Devices and Systems stated in 2017.[7] The summation of all data created, captured, or replicated in the world will grow from 33 Zettabytes (ZB) in 2018 to 175 ZB by 2025.[8] In this connection, the global 3-D NAND flash memory market is expected

to grow from $9,056.2 million in 2017 to $99,769.0 million by 2025 at a CAGR of 35.3% from 2018 to 2025.[9] Compared to 3-D flash memory, which can experience oxide crystal lattice damage by quantum tunneling and hot electron injection, leading to a finite lifespan, the NW-based 3-D memory (e.g., racetrack memory) does not experience a wear-out phenomenon. This is due to its use of electron spins and magnetic moments to read and write data, which give it the fundamental advantage of high reliability. It is also likely to be inexpensive because it can store 100 bits of memory or more in a single transistor.

Furthermore, NWs can be used as interconnects. Next-generation millimeter and sub-millimeter wave communication technology will utilize nano-transistors, which typically rely on vias for vertical interconnection in 3-D integrated circuits. Traditionally, vias of transistors and other devices can cause excessive power loss due to the skin effect, which is a serious issue that must be overcome. The skin effect is a tendency for alternating current to flow mostly near the outer surface of an electrical conductor as compared to the core of the conductor. The effect becomes more and more apparent as the frequency increases. NW-based interconnects offer a potential solution to this problem. Due to their small diameter, NWs are more transparent to electromagnetic fields at high frequency, which minimizes the skin effect. When used in bundles, Cu NWs can guarantee uniformity and lower power loss and parasitic inductance. As the demand for increasingly smaller electronic devices grows, the small circuit production will be required as well. NW-based designs would have great advantages in achieving this.

As in many cases previously described, there are many areas where NWs can be uniquely suited to solving challenges. This dissertation explores how NWs can be fabricated, engineered, and used in various applications with their unique properties. Chapter 2 explains the fabrication and characterization of NWs. Chapter 3 discusses various types of magnetic NWs and their properties for applications. Chapter 4 shows magnetic NW-based biolabeling system using

ferromagnetic resonance. Chapter 5 introduces fabrication of AAO and NWs for 3-D magnetic memory. Chapter 6 highlights NW-based interconnects with the promising DC resistance measurement results. Chapter 7 talks about other NW-based applications. Lastly, Chapter 8 provides conclusions and future work recommendations.

Chapter 2

Nanowire fabrication and characterization

2.1. Anodic aluminum oxide for nanowire growth

Nanomaterials and nanostructures have been researched extensively in most science-related areas due to their special material properties coming from nanometer-sized features. Among many fabrication processes to make nanomaterials or nanostructures, electrochemical deposition is a relatively simple and economic process. Electrochemical deposition is a well-known conventional chemical deposition method of thin films and can produce nanomaterials, such as nanowires (NWs), by using porous templates simply and cost-effectively compared to lithographic processes that require expensive equipment and many process steps. In other words, to make NWs by electrochemical deposition, nanoporous templates are required.

There are two popular kinds of templates: anodic aluminum oxide (AAO) and track-etched polycarbonate (TEPC). AAO is a porous aluminum oxide made by anodization of aluminum (Al) film or foil. Pores are hexagonally ordered and pore direction is fairly vertical. Pore size (i.e., pore diameter, usually 10–200 nm), interpore distance (i.e., interwire distance, usually 50–500 nm), and thickness (i.e., pore length, usually up to 100 μm) of AAO can be adjusted in anodization and pore widening processes. Also, AAO is relatively durable and a good insulator, which is ideal for electrodeposited materials inside AAO pores. AAO is shown in Figure 2.1. TEPC is made by ion bombardment and pore widening through polycarbonate membranes.

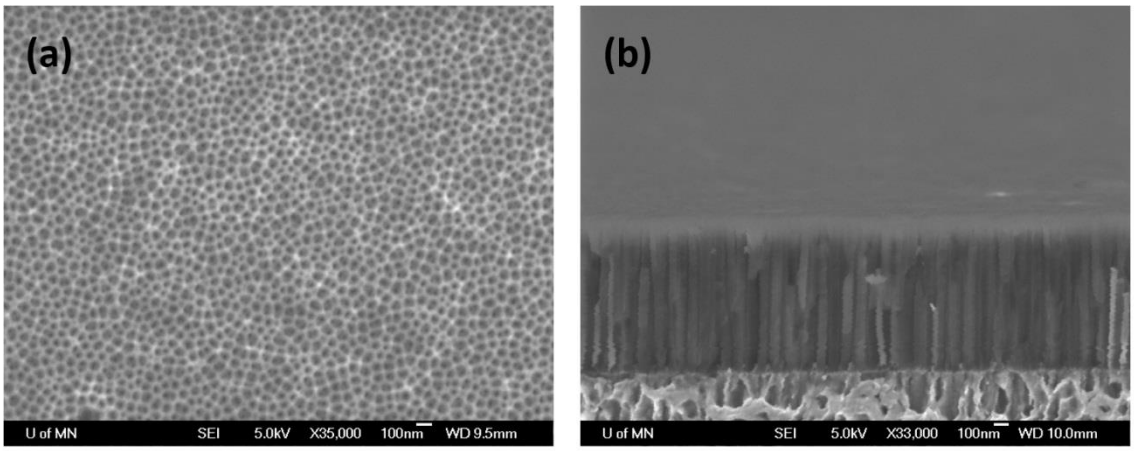

Figure 2.1. SEM images of (a) top view (surface) and (b) cross-sectional view of AAO.

Since it is hard to control the direction of accelerated ions in the fabrication process of TEPC, pores of TEPC are randomly distributed and pore direction is not always vertical. Pore size is usually from 10 nm to 10 μm and thickness is usually less than 20 μm.[10] TEPC membranes usually have large interpore spacings. In other words, they have small pore density or porosity compared to AAO. Also, TEPC is flexible. TEPC is shown in Figure 2.2.[11] In this dissertation, most of the applications under study require high densities of nanowires or mechanically and electrically

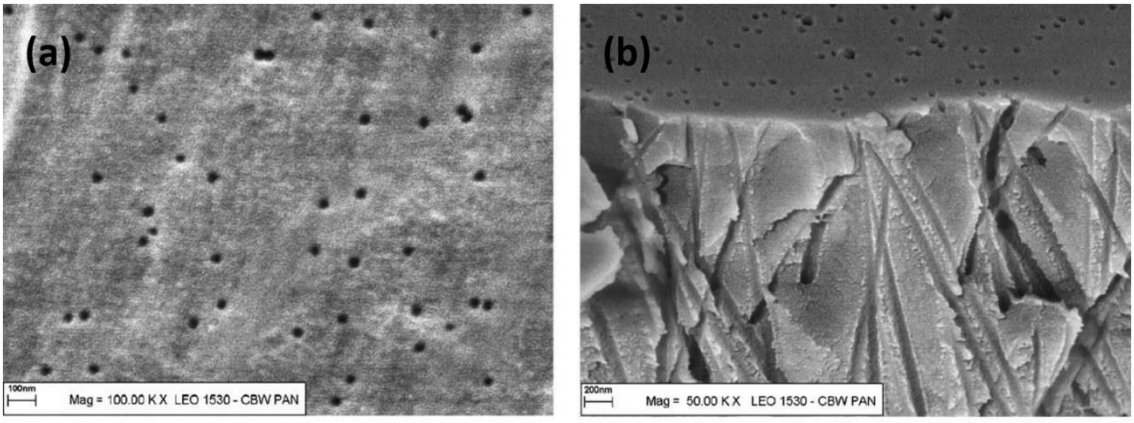

Figure 2.2. SEM images of (a) top view (surface) and (b) cross-sectional view of TEPC.[11]

stable insulators among nanowires. So, AAO templates were mainly used for nanowire growth in this dissertation.

2.1.1. AAO fabrication theory

Anodization is an electrochemical passivation process to grow natural oxide thicker on metal surfaces to enhance corrosion and wear resistance as a surface treatment, and it is broadly used for Al and its alloys in many industries. AAO is made by this anodization process as shown in Figure 2.3.

The electrochemical system for Al anodization consists of two electrodes: Al foil or film as a working electrode (anode) and platinum (Pt) mesh as a counter electrode (cathode). These two electrodes are immersed in acidic electrolytes, such as oxalic acid, sulfuric acid, and

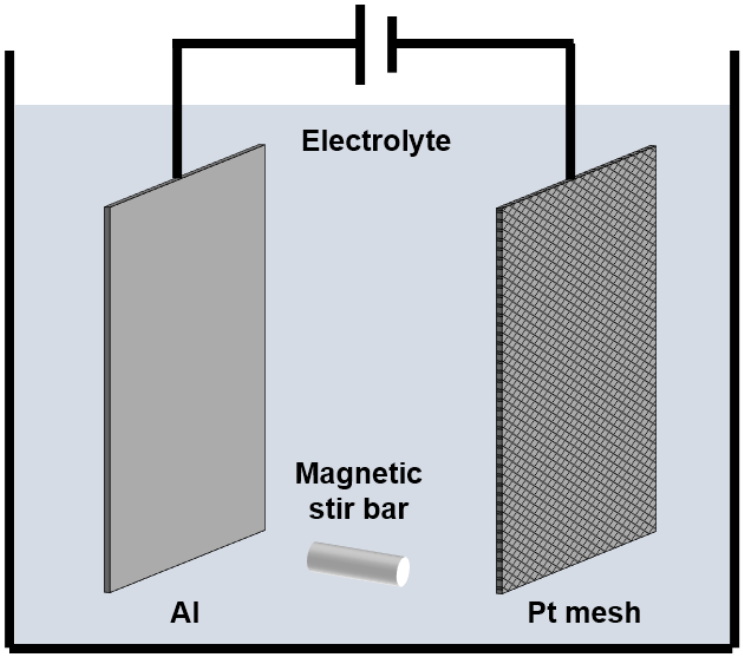

Figure 2.3. Schematic of Al anodization.

phosphoric acid. The temperature during the process is usually controlled by an external cryostat. A magnetic stir bar is used to keep the electrolyte concentration uniform.

As a result of the anodization, Al_2O_3 grows on the Al surface. If the Al_2O_3 is not soluble in the electrolyte, the barrier-type oxide (a thin, non-porous, and dense Al_2O_3) is formed on the Al surface, and if the Al_2O_3 is slightly soluble in the electrolyte, porous-type oxide (a nano porous Al_2O_3 that can grow with the duration of anodization) is formed on the alumina barrier layer.[12]

In the Al anodization process, Al^{3+} ions come from the metal/oxide interface and further move out from the oxide/electrolyte interface into the electrolyte. In the meantime, O^{2-} or OH^- ions move into the metal/oxide interface through oxide/electrolyte. Those ions can move within the aluminum oxide under the anodization electric field as shown in Figure 2.4.[13] Then, Al^{3+} and O^{2-} or OH^- ions meet together at both metal/oxide and oxide/electrolyte interfaces, which corresponds

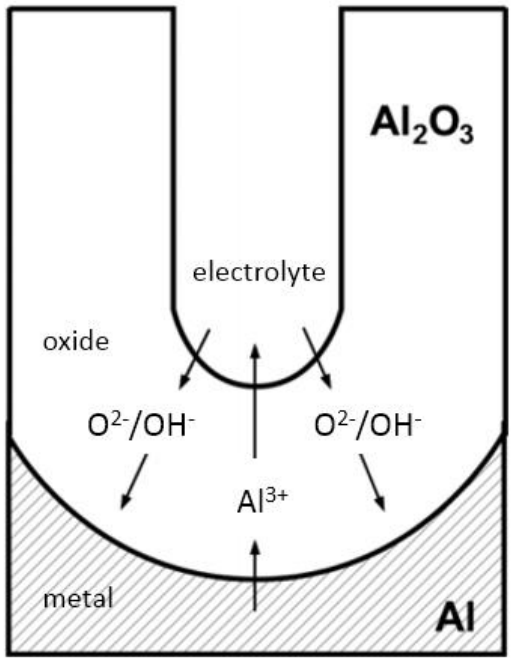

Figure 2.4. Schematic of ion transport for porous-type aluminum oxide.

to the formation of aluminum oxide at both interfaces. The following reactions are considered to be occurring at the interfaces.[13]

At the metal/oxide interface:

$$Al \rightarrow Al^{3+} + 3e^{-}$$

$$2Al^{3+} + 3O^{2-} \rightarrow Al_2O_3 \quad \text{or} \quad 2Al^{3+} + 3OH^{-} \rightarrow Al_2O_3 + 3H^{+}$$

At the oxide/electrolyte interface:

$$2Al^{3+} + 3O^{2-} \rightarrow Al_2O_3 \quad \text{or} \quad 2Al^{3+} + 3OH^{-} \rightarrow Al_2O_3 + 3H^{+}$$

$$Al_2O_3 + 6H^{+} \rightarrow 2Al^{3+} + 3H_2O$$

Last reaction at the oxide/electrolyte interface describes alumina dissolution by H^+ ions and it is heat or field-assisted dissolution at pore core in the formed oxide.[13] It is noted that the electric-field distribution depends on the topography of the surface.[14] This means that Al with less surface fluctuation will make better ordered pores in anodization. So, a nano porous AAO is made by repetition of formation and partial dissolution of Al_2O_3 in Al anodization process.

2.1.2. AAO fabrication process

2.1.2.1. One-step anodization

There are several stages in AAO growth by one-step anodization as in Figure 2.5. When Al is exposed to the anodization electrolyte, it forms a thin Al oxide barrier layer (also called barrier-type oxide) on the entire Al surface and the barrier layer decreases the current density rapidly since it is not conductive (Figure 2.5(a) and (e)). Pores nucleate in random positions at the oxide/electrolyte interface due to nonhomogeneous thickness of the barrier layer (Figure 2.5(b)).[12]

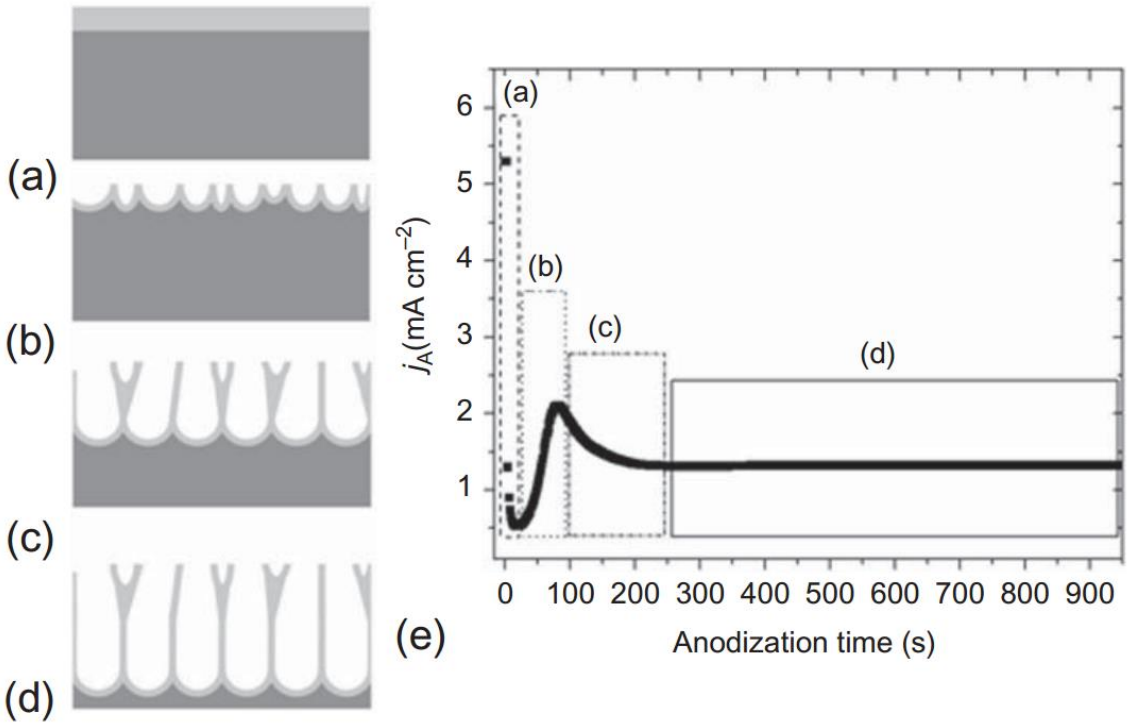

Figure 2.5. Schematic of pore formation in AAO: (a) formation of Al oxide barrier layer, (b) nucleation of pores, (c) pore homogenization, and (d) pore growth. (e) A plot of a typical transient current during pore nucleation and growth for a constant potential anodization.[12]

The local topographic irregularities shown in Figure 2.5(b) causes stronger electric fields that increase the Al_2O_3 formation and dissolution rates at their positions compared with the flat regions.[12] At this stage, the current density increases as in Figure 2.5(e). As seen in Figure 2.5(c), some pores stop growing because of the competition among the pores, and the current density decreases as in Figure 2.5(e). Then, the current density becomes constant (Figure 2.5(e)) when a steady-state equilibrium is established between the formation and dissolution of Al_2O_3 at the pore bottom as shown in Figure 2.5(d).[12] The barrier layer's thickness and shape don't change with the anodization time and the barrier layer thickness is estimated by $t_b = AR \times U$, where t_b is a barrier layer thickness, AR is the anodizing ratio (between 0.6 and 1.4 nm/V for mild and hard anodization processes, which is discussed later), and U is the applied anodization voltage.[12,13] Usually, the pore

arrangement at the bottom of AAO is better than that at the top surface of AAO as a result of the gradual rearrangement of the initially disordered pores as shown in Figure 2.5(d).[13]

2.1.2.2. Two-step anodization

In order to make the pore arrangements better at the AAO surface, two-step anodization process can be used, which was developed by Masuda and Fukuda in 1995.[15] The basic concept (Figure 2.6) is, growing AAO by first anodization, removing the AAO with disordered pores at surface to use arrays of hemispherical concaves at Al surface as pore nucleation sites in second anodization, and growing new AAO with ordered pores by second anodization at the same condition to the first one.[13] The scanning electron microscopy (SEM) images of AAO and Al during two-step anodization are shown in Figure 2.7.

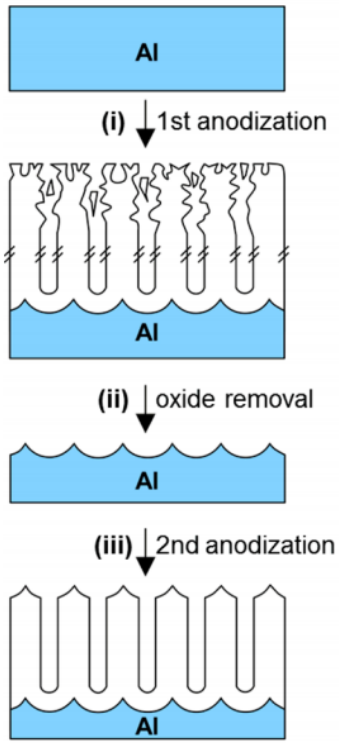

Figure 2.6. Schematic of two-step anodization.[13]

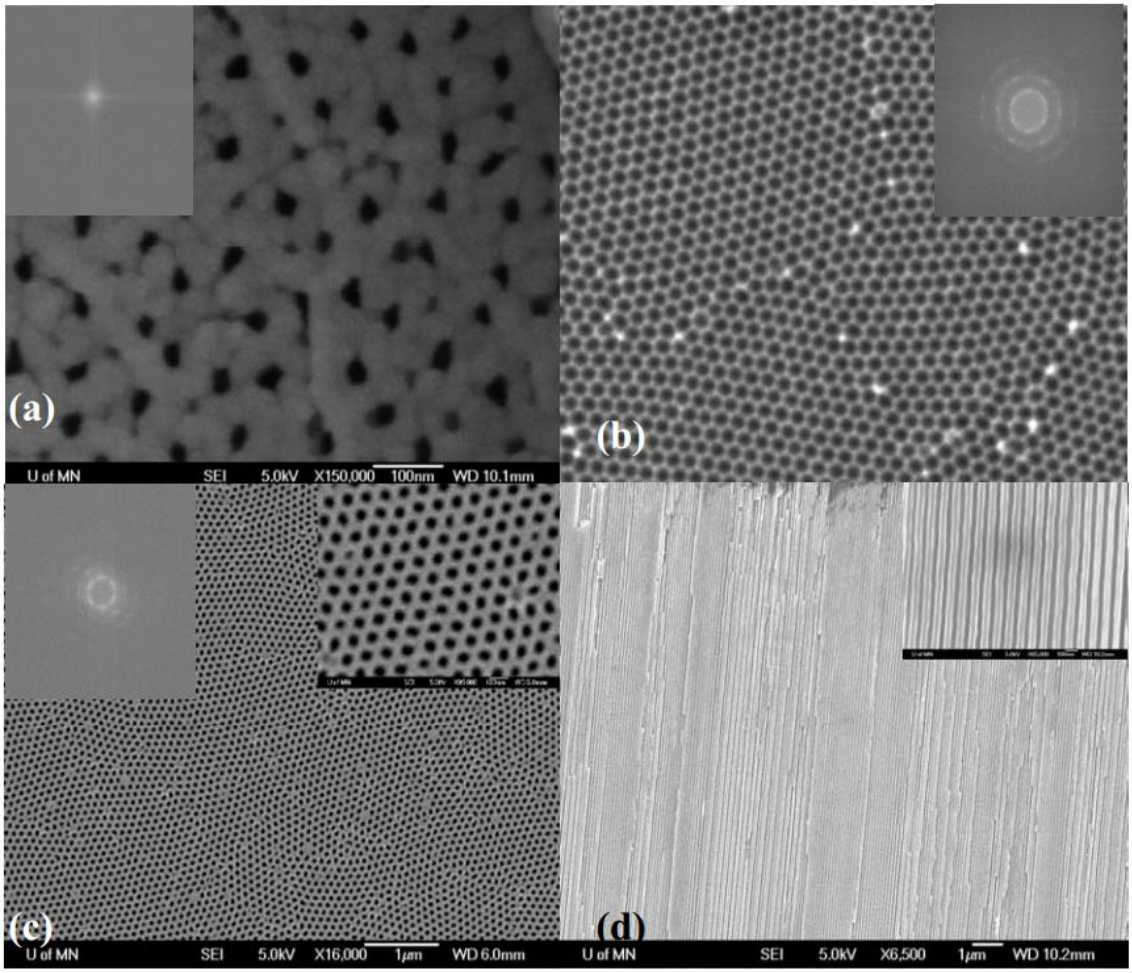

Figure 2.7. Top view SEM images of (a) AAO by 1st anodization, (b) Al surface after oxide removal, and (c) AAO by 2nd anodization. (d) cross-section view SEM image of AAO by 2nd anodization.[14]

AAO with ordered pores by two-step anodization, however, requires typically more than 10 hours for first anodization only to get the hexagonally closed-packed concaves on the Al surface. Considering the processing time more than 10 hours and the oxide growth rates of 1–10 μm/h in Al anodization,[13,16,17] Al foils should be used as a base material for self-ordered porous AAO by two-step anodization. The long 1st anodization cannot be applied to thin Al films on Si (such as Al films with thickness less than 5 μm). But, two-step anodization with the reduced 1st anodization time can be utilized in anodization of Al films. Figure 2.8(a) shows as-deposited Al by e-beam

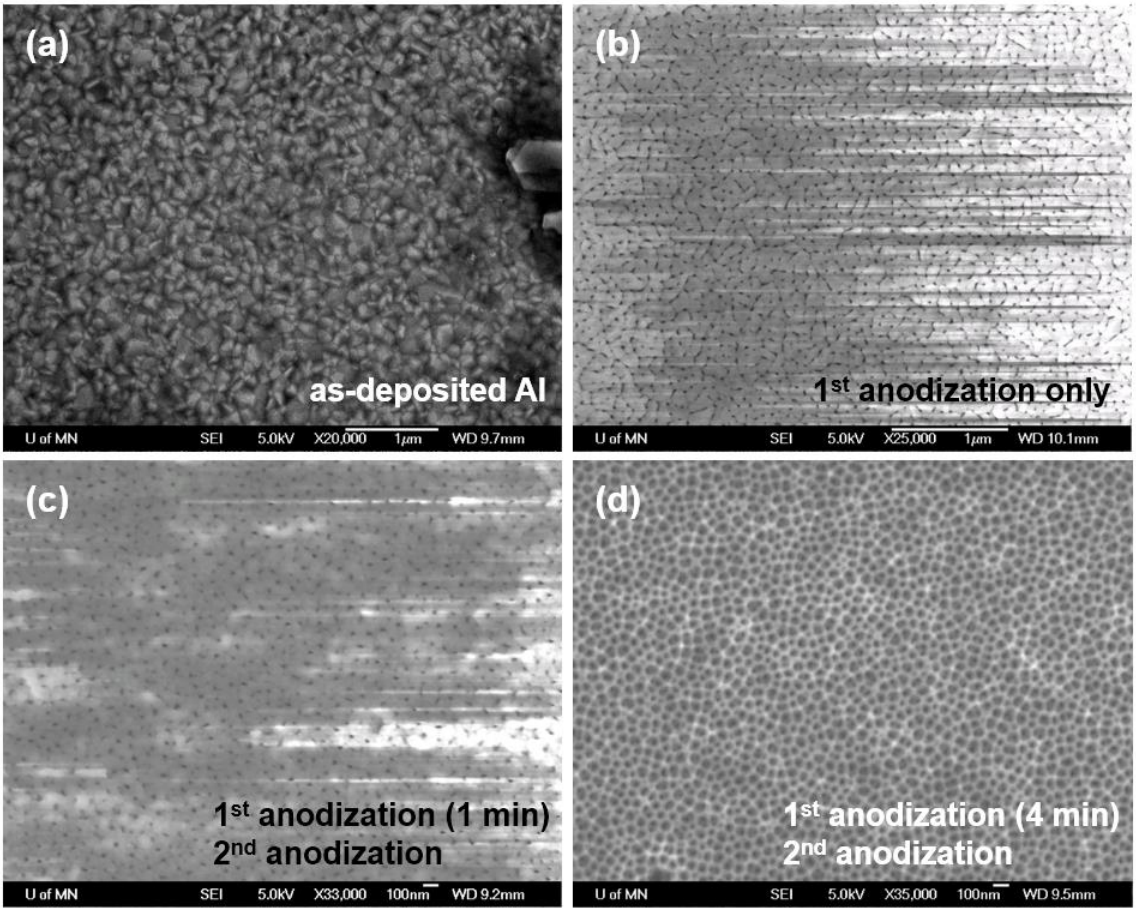

Figure 2.8. Top view SEM images of (a) as-deposited Al by evaporation, (b) AAO by 1st anodization only, and (c, d) AAO by two-step anodization with 1st anodization for (c) 1 min and (d) 4 min.

evaporation, which has a grainy surface. When this Al is anodized, then AAO looks like the one in Figure 2.8(b), which is still grainy. But, two AAO made by two-step anodization with 1st anodization for 1 min and 4 min are less and no grainy, respectively, as in Figure 2.8(c, d). Two-step anodization with short 1st anodization can still yield (not perfect but) better surface and pore arrangement on AAO. In case of Al film anodization, the amount of Al left by AAO removal after 1st anodization could be too thin for other further processing. So, one-step anodization can be used in some cases to reduce Al loss. AAO made of Al film and integrated on Si is covered in Chapter

6. Also, long-range ordered porous AAOs made by imprinting methods are covered in Chapters 3 and 5.

2.1.2.3. Mild and hard anodization

Anodization process broadly used in the surface finishing industry is by hard anodization (HA), which involves high current densities, typically larger than 100 mA/cm^2. HA processes show very fast oxide growth rates of 50–100 μm/h due to the high current density but the resulting AAO films by HA show also uneven surfaces with cracks and non-uniform pores.[13] On the other hand, mild anodization (MA) processes using small current densities less than 10 mA/cm^2 can yield better controlled AAO films and have been employed for nanotechnology applications in spite of slow oxide growth rates of 1–10 μm/h.[13,17,18] Recently, many developments in HA have been made to overcome HA's intrinsic problems.[12,13,16]

2.1.2.4. AAO structural properties

Interestingly, anodization electrolytes (such as sulfuric acid, oxalic acid, phosphoric acid, and selenic acid) have their own self-ordering regimes in both MA and HA as shown in Figure 2.9. This means that interpore distance in AAO can be adjusted by varying anodization electrolytes and potentials. There is a relationship between interpore distance (D_{int}) and anodization potential (U) in MA regardless of the electrolyte types, $D_{\mathrm{int}} = \zeta_{\mathrm{MA}} \times U$, where ζ_{MA} is a correlation parameter in MA and typically ~ 2.5 nm/V.[13,16,17] A correlation parameter in HA, ζ_{HA}, is 1.8–2.0 nm/V.[12,13,16] Besides the interpore distance, there are other important structural properties, such as pore diameter, barrier layer thickness, pore wall thickness, pore density, and porosity. They can

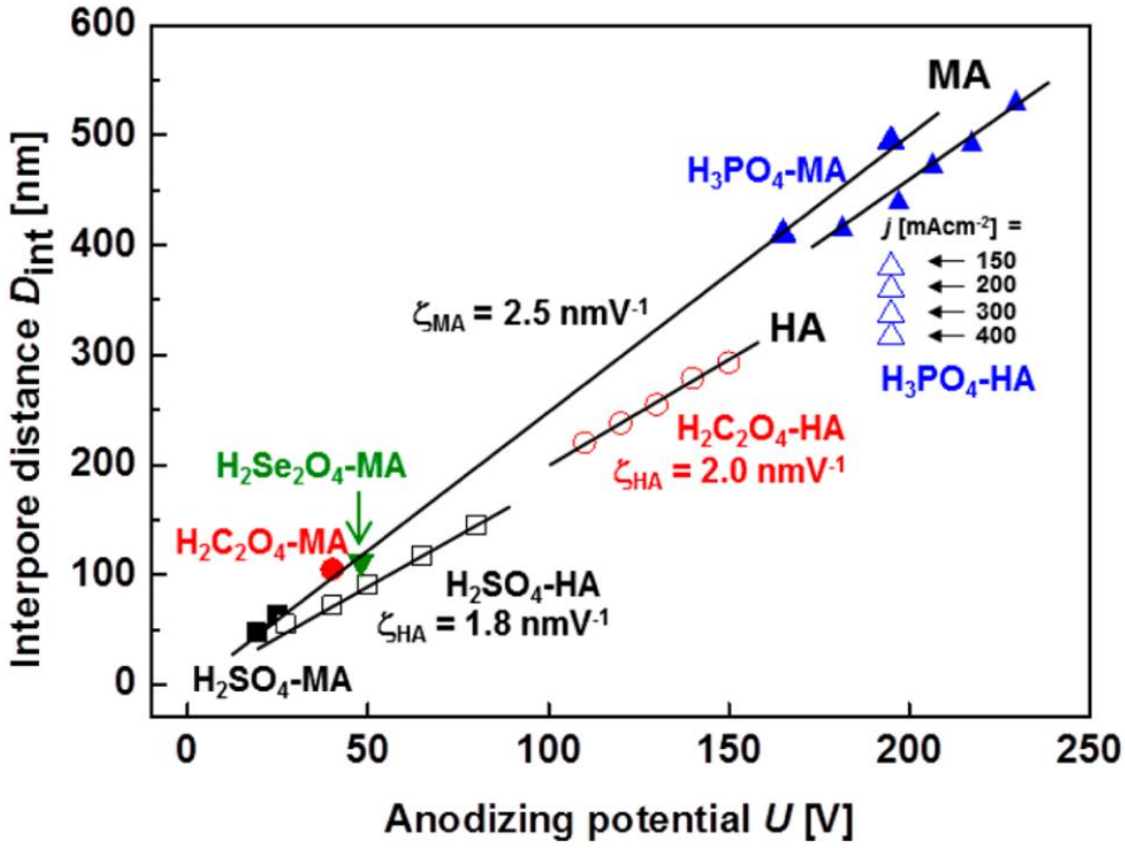

Figure 2.9. Self-ordering regimes in MA (filled symbols) and HA (open symbols) by using H_2SO_4 (black symbols), $H_2C_2O_4$ (red symbols), H_2SeO_4 (green symbol), and H_3PO_4 (blue symbols). The black solid lines represent the linear regressions of the data with correlation parameters, 2.5 nm/V for MA and 1.8−2.0 nm/V for HA. Data for H_3PO_4-HA (△) show current density (j) dependence of the interpore distance at a fixed anodizing potential, 195 V.[13]

directly affect the properties or performance of nanomaterials and nanodevices made from AAO templates.

Pore diameter (D_P) increases with anodization potential, for example, at the rate of 1.29 nm/V for potentiostatic (=using constant potential) anodization in phosphoric acid, and similarly, pore diameter also increases with current density.[13] It is because current density normally increases with potential. Temperature of the electrolyte is another variable that determines pore diameter,

and the pore diameter decreases when the temperature decreases.[13] Pore diameter of AAO also depends on the solubility of anodizing acid electrolyte, meaning that the weaker solubility of electrolyte is used, the smaller pores are formed in AAO.[13] The pore diameter can be increased after AAO formation by chemical wet etching of pore wall of AAO, for example, in 5 wt% H_3PO_4. By doing this, the barrier layer at the bottom of AAO can be thinned or removed at the same time.

Barrier layer thickness (t_b) is determined by $t_b = AR \times U$, where AR is the anodizing ratio and U is the applied anodization potential.[12,13] AR value ranges from 0.6 to 1.4 nm/V for MA and HA processes.[12,13] The average anodizing ratio for various electrolytes in both MA and HA is determined to be ~ 1 nm/V as shown in Figure 2.10.[13]

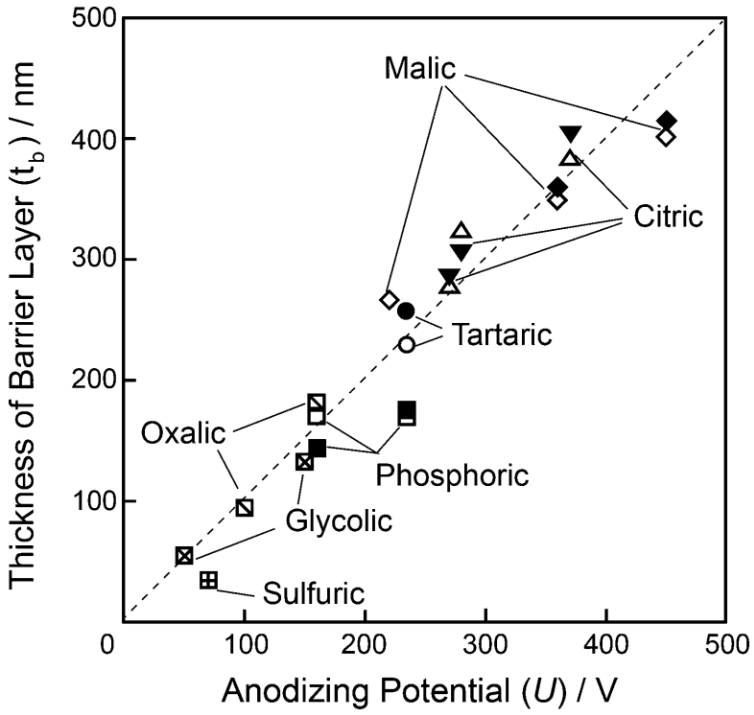

Figure 2.10. Relationship between anodizing potential and barrier layer thickness for porous AAO formed in different acid electrolytes (solid symbols, measured values; open symbols, calculated values from the half-thickness of the pore walls).[13]

Pore wall thickness is generally twice the thickness of the barrier layer. Pore density (ρ_{P}) and porosity (P) can be calculated by the following relationships:[13,16,19]

$$\rho_{\mathrm{P}} = \left(\frac{\pi}{\sqrt{3}D_{\mathrm{int}}^2}\right) \times 10^{14}\ cm^{-2}$$

$$P(\%) = \left(\frac{\pi}{2\sqrt{3}}\right)\left(\frac{D_{\mathrm{P}}}{D_{\mathrm{int}}}\right)^2 \times 100$$

2.1.3. Experimental AAO fabrication process

Al foil (99.999 %) is degreased in acetone for 10 min, rinsed with deionized water, and soaked in 1 mol NaOH for 3 min to remove the natural Al oxide. Then, the Al foil surface is smoothed by electropolishing (Al foil as anode and Pt mesh as cathode) with a mixture of perchloric acid : ethanol = 1 : 5 at 9 °C for 5 min with a constant potential of 18 V. By the electropolishing, the Al surface is oxidized and dissolved in the electropolishing solution and becomes like a mirror. After the electropolishing, it is anodized in 0.3 mol oxalic acid at 17 °C at constant 40 V for more than 10 hours. The AAO made by the first anodization is removed using a mixture of 6 wt% phosphoric acid (H_3PO_4) and 1.8 wt% chromic acid (H_2CrO_4) at 60 °C. Next, the Al foil is anodized again under the same condition used for the first anodization until the desired AAO thickness is reached. The remaining Al substrate of the AAO is floated in a solution of copper chloride ($CuCl_2$) or mercury chloride ($HgCl_2$) and etched to make a free-standing AAO template. There is a barrier layer blocking pores at the AAO/Al interface side. This side of AAO is floated and etched in 5 wt% H_3PO_4 to open the pores. Additionally, the pore diameter can be increased by immersing the AAO in 5 wt% H_3PO_4. Then, the sample should be sonicated in DI water for 5 minutes to remove the residue in pores. The sample is rinsed between each step. AAO made of Al film and integrated on Si is covered in Chapter 6.

2.2. Electrochemical deposition to grow nanowires

Electrochemical deposition has a long history and is a well-known conventional metal coating process in many industries. It is also able to make nanostructured materials (e.g., NWs) with porous templates (e.g., AAO and TEPC). Compared to other deposition techniques, such as chemical vapor deposition and physical vapor deposition, the template-assisted electrochemical deposition is simple, inexpensive, and fast, and can be performed without special equipment. In this section, electrodeposition is covered as a synthetic technique for nanowires.

2.2.1. Electrodeposition theory

A system for template-assisted electrodeposition is shown in Figure 2.11. It is a standard three-electrode electrochemical system consisting of AAO template as a working electrode (cathode), Pt mesh as a counter electrode (anode), and a reference electrode. A two-electrode system that doesn't have a reference electrode can be used as well. Reference electrodes set the relative potential of a solution in an electrodeposition system and are similar to the ground node in an electrical circuit. In order to monitor and control the potential of the working electrode accurately, the three-electrode systems are recommended.

There are two common modes in electrodeposition: a galvanostatic mode and a potentiostatic mode. In the galvanostatic mode, the current applied is kept constant during electrodeposition. In the potentiostatic mode, the voltage applied is kept constant.

Electrolyte bath needs to be stirred vigorously by a magnetic stir bar to keep electrolyte concentration uniform during deposition.

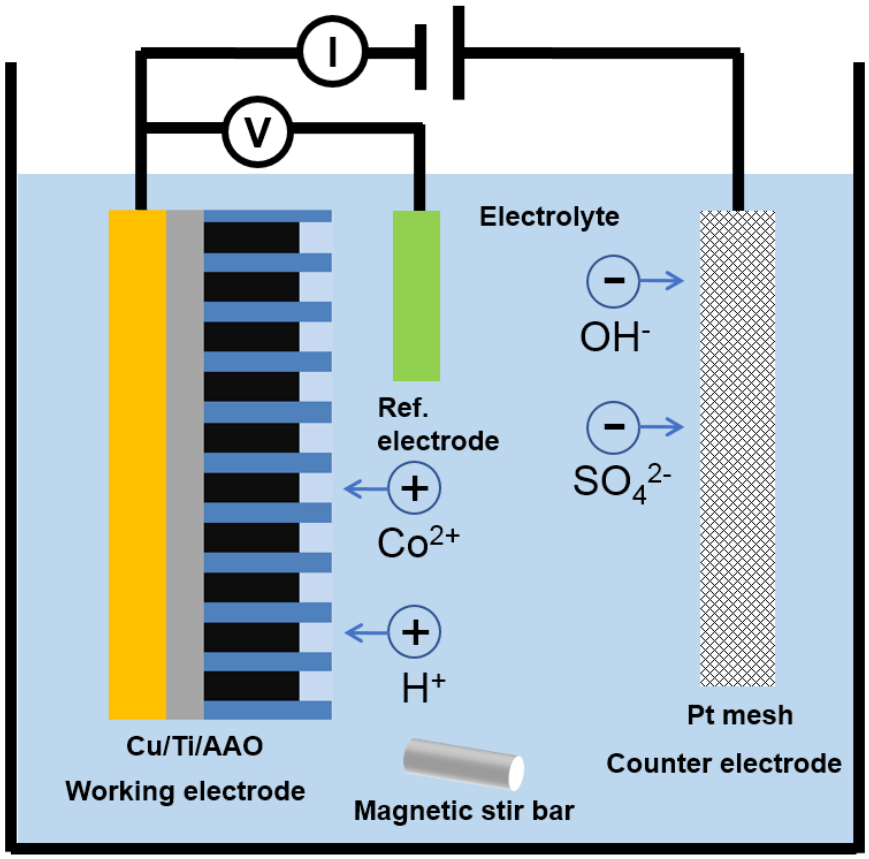

Figure 2.11. Schematic of a three-electrode electrodeposition system with AAO template.

AAO templates are not conductive since they are Al oxide. To use them in electrodeposition as a working electrode (cathode), titanium (Ti, 0−20 nm) and copper (Cu, 300−500 nm) films are deposited on one side of AAO as an adhesion layer between AAO and Cu and an electrical contact for electrodeposition, respectively.

Next, a voltage is applied between the working electrode and the counter electrode so that the positively charged metal ions such as cobalt (Co) ions (Figure 2.11) in the electrolyte can be electrostatically attracted towards the negatively charged working electrode (cathode). Then,

inside pores of AAO, the metal ions get electrons through Cu contact, and as a result of this reduction reaction, the metal is deposited and forms nanowires.

Figure 2.12 shows nanowire growth and current behavior with respect to time during potentiostatic electrodeposition (the plot of current and voltage versus time was from the electrodeposition of Cu NWs in AAO on Si and used for this explanation). The nanowire growth and current behavior can be explained in three stages. In stage 1, nanowires grow in AAO pores and the current is mostly constant since the amount of current is proportional to the electrode area in contact with electrolyte and the electrode area is limited to the area of pores only. The nanowire growth continues until nanowires reach the top surface of AAO. When they reach the top, there is

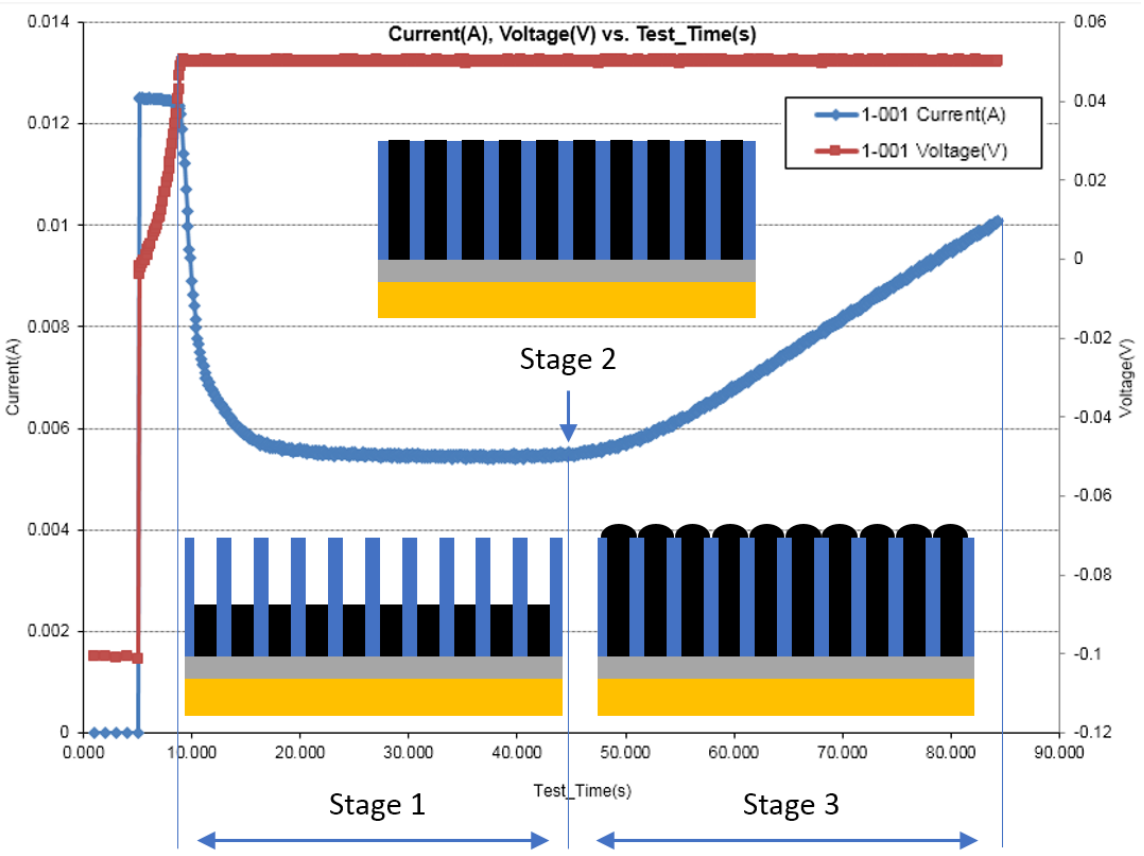

Figure 2.12. Current as a function of time for potentiostatic electrodeposition with AAO template.

no area limitation for them to grow, this is stage 2. After this point, during stage 3, nanowires grow three-dimensionally and they look like mushrooms. Then, the effective electrode area increases and the current also rapidly increases. Sometimes, even before nanowires reach the top, the current may increase when AAO templates with small pores (e.g., 10–20 nm) are used. It is because the wetting of electrolyte is not good inside pores then nanowire growth starts in some pores first and the number of pores in which growth proceeds may increase over time.[20] Once mushrooms cover the whole AAO top surface and grow like a film, then the current is saturated, which is not shown in Figure 2.12. So, by monitoring the current (deposited charges), nanowire length can be controlled.

2.2.2. Nanowire fabrication process

2.2.2.1. Approaches to making uniform nanowires

In reality, each of nanowires grown in AAO pores has a different length. If the performance or properties of applications using the nanowires need to be consistent, uniformity in nanowire length at least should be high. There are several approaches to increasing the nanowire length uniformity.

When Ti and Cu films are deposited on one side of AAO before electrodeposition, the Cu film should be thick enough to block the pores to avoid electrolyte leakeage. The Cu thickness depends on the pore size. For example, AAO with 40 nm pore diameter needs 200–300 nm Cu film. AAO templates with larger pores need thicker Cu films.

Similarly, before nanowire deposition, Cu seed layer (1–5 μm thick) can be electro-deposited first to block the pores, to fill dendrite structures that often form at the bottom of the AAO pores, and to provide nucleation sites for simultaneous nanowire growth.[17]

During electrodeposition using porous AAO templates, excess cations (metal ions) are continously diffused in the pores from the bulk electrolyte forming the hemispherical diffusion layers at the pore edge area, which means that the cations going in the pores tend to be concentrated at the pore edge area.[21,22] This reuslts in nonuniform nanowire length. But, the slow ion transport rate can prevent this phenomenon.[21] To get the slow ion transport rate, low temperature for electrolyte can be used. Shin et al. showed the extremely high nanowire length uniformity using the electrodeposition temperature of −2.4 °C. Also, low voltage as an initial electrodeposition potential can be used to get the slow ion transport rate. Especially, at the beginnig of electrodeposition, it is preferred that most pores start nucleation at the same time and have a foundation to grow nanowire further. After growing nanowires uniformly at small potential at the beginning, it is okay to increase the potential to increase the deposition rate. So, using low temperature and low initial potential in electrodeposition is to adopt the reaction-limited regime rather than the diffusion-limited regime.

Pulsed-electrodeposition is a process in which a deposition pulse (e.g., 0.5–1 sec) and a rest pulse (e.g., 0.5–1 sec) proceed alternately, and it can improve the length uniformity by removing non-uniform overlapping of the hemispherical diffuion layers at the pore edge area.

Another way to improve the length uniformity is to use a surfactant such as sodium dodecyl sulfate (SDS, also called sodium lauryl sulfate, SLS, 0.1–4 mmol). Electrolyte cannot go inside small sized pores easily. Also, even though the elctroylte goes in the pores, hydrogen gas bubbles can accompany electrodeposition and they may be trapped in the small pores, inhibiting the further deposition.[17] So growing nanowires using small pore AAO templates (e.g., 10–20 nm pore diameters) is hard compared to larger pores (e.g., 40–200 nm pore diameters). SDS (or SLS) improves the wetting of the electrolyte, reduces the bubble diameters, and increases bubble

detachment from the electrode surface (i.e., AAO surface) by changing surface tension and gas solubility.[23]

Lastly, sonicating the AAO templates in deionized water (or with ethanol) for shor time (30 sec–2 min) before electrodeposition can improve the wetting of electrolyte and help nanowire grow homogeneously in the deposition process.[20]

2.2.2.2. Single element nanowires

By template-asssited electrodeposition, many knids of single element nanowires can be made, such as Fe, Co, Ni, and Cu, which are used in this dissertation. Fe nanowires are made from a solution of 0.55 mol $FeSO_4$ (Fe^{2+} source), 0.73 mol H_3BO_3, and 5.68 mmol $C_6H_8O_6$ (pH = 3) at a pulsed-potential of V = −1.1 V versus Ag/AgCl.[24] Co nanowires are fabricated from a 0.85 mol $CoSO_4$ (Co^{2+} source) and 0.48 mol H_3BO_3 (pH = 2 for FCC, pH = 4 for HCP with c-axis oriented perpendicular to the wire, and pH > 6 for HCP with c-axis oriented parallel to the wire) at a pulsed-potential of V = −0.95 V versus Ag/AgCl.[24,25] Ni nanowires are deposited from a solution of 0.85 mol $NiSO_4$ (Ni^{2+} primary source), 0.17 mol $NiCl_2$ (Ni^{2+} secondary source, also increases solution conductivity thereby reducing voltage requirement), and 0.65 mol H_3BO_3 (pH = 2.5) at a pulsed-potential of V = −0.9 V versus Ag/AgCl.[24,26] Cu nanowires are made from a solution of 0.2 mol $CuSO_4$ (Cu^{2+} source) and 0.2 mol H_3BO_3 (pH = 3) at a pulsed-potential of V = −0.5 V versus Ag/AgCl.[24] The pH of the solutions was adjusted using diluted H_2SO_4 and NaOH.[24]

Boric acid (H_3BO_3) is used as a pH buffer in most electrolytes for metal electro-deposition.[27] In the electrodeposition process, H^+ ions are reduced at the working electrode (cathode). The amount of H^+ ions in the electrolyte decreases and the pH of the electrolyte increases (i.e., there are more OH^- relatively). Boric acid exists as a mixture of borate ions and

non-ionized boric aicd in the electrolyte and some boric acid is ionized to replace the lost H^+ ions when the H^+ ions are reduced.[26] So, the pH change of the electrolyte is limited.

In addition, ammonium chloride (NH_4Cl, 0.3 mol) can be added in all electrolyes. Since H^+ ions are depleted by hydrogen reduction in the electrolyte near the working electrode (cathode) surface, the pH near the working electrode is always higher than that in the bulk electrolyte.[28] But, NH_4Cl can stabilize the pH of the electrolyte by giving H^+ ions to react with OH^- in the electrolyte. Also, SDS (0.1–4 mmol) can be added if AAO templates with small pore diameters (10–20 nm) are used in order to enhance the wetting of the electrolyte and to remove hydrogen gas bubbles inside pores.[17] Saccharin sodium ($C_7H_5NO_3S$) can be added to make grains smooth and regular.[17]

For Fe NW deposition, ascorbic acid ($C_6H_8O_6$) is added as an antioxidant to prevent Fe^{2+} from becoming Fe^{3+} by oxidation because of dissolved O^{2-} from the air.[17] Malonic acid ($C_3H_4O_4$, 1 mmol) can be added in Fe electrolyte as a complexing agent to form stable complexes with Fe^{3+} ions.[17] By using $C_6H_8O_6$ and $C_3H_4O_4$, Fe NW length uniformity can be improved.

2.2.2.3. Multilayered nanowires

Multilayered nanowires consisting of two different element layers alternately can be made by electrodeposition using two different electrolyte baths separately or one bath with a mixture of two electrolytes.

If the two separate baths are used, the AAO template is simply put in and out of two separate baths alternately for a certain period of time to get the desired segment lengths. Any elements or combinations can be deposited. Before changing baths during the process, rinsing step should be required. A drawback is that there is a risk of contamination, such as corrosion at the

interface between two segments.[17] Also, it would be difficult to deposit many bilayers (e.g., more than 100 bilayers) with two separate baths.[17]

On the other hand, the electrodeposition with one bath made of two electrolytes eliminates the hassle of changing baths and the defects such as corrosion. But, two metals should not have similar reduction potentials with each other. Otherwise, it is likely to have alloys made of two metals due to the co-deposition. For example, electrodepositing bilayers of Fe/Co or Co/Ni is harder than that of Fe/Cu or Co/Cu using a mixture electrolyte. Other drawback is that segment lengths might be irregular if potentiostatic electrodeposition is used. But, this can be resolved by galvanostatic electrodeposition that can control the segment lengths more precisely.[17] It is noted that for one electrolyte bath to deposit mulilayered nanowires, the ratio of a metal with a high negative reduction potential (e.g., Fe with −1.1 V) and a metal with a low negative reduction potential (e.g., Au with −0.6 V) should be higher than 1:1. At low negative potential (e.g., −0.6 V), only the metal with a low negative reduction potential (e.g., Au) is deposited. At high negative potential (e.g., −1.1 V), both metals (e.g., Fe and Au) are co-deposited. To reduce the amount of the metal with a low negative reducton potential (e.g., Au) at high negative potential (e.g., −1.1 V), the amount of the metal with a low negative reduction potential (e.g., Au) should be small compared to that of the metal with a high negative reduction potential (e.g., Fe) in the electrolyte. For example, Fe/Au multilayered nanowires in Chapter 5 were made of a single bath with a molar ratio of Fe and Au of 40:1.

2.2.3. Experimental nanowire fabrication process

One side of AAO template is coated with Ti (0−20 nm) as an adhesion layer and Cu (300−500 nm) as an electrical contact by sputtering or evaportaion. Since AAO templates are brittle, a rigid support such as a glass slide is required in electrodeposition. Cu side of AAO template should be put on Cu tape attached to the glass slide to get electrical contact as shown in Figure 2.13(a, c). Wood pieces and rubber band can be used to remove a gap between AAO and Cu tape causing a contact issue as shown in Figure 2.13(b). Next, the sample is insultated with an insulation tape, leaving a deposition area. The sample can be sonicated in the deionized water with a small amount of ethanol to enhance the wetting of electrolyte in the electrodeposition. After electrodeposition as showin in Figure 2.11, the sample is unwrapped with an adhesive remover to acquire the AAO template with nanowires. If the Cu film on the electrodeposited AAO needs to be removed, then 1 M $Fe(NO_3)_3$ can be used to remove Cu film. Ti film can be etched by a mixture

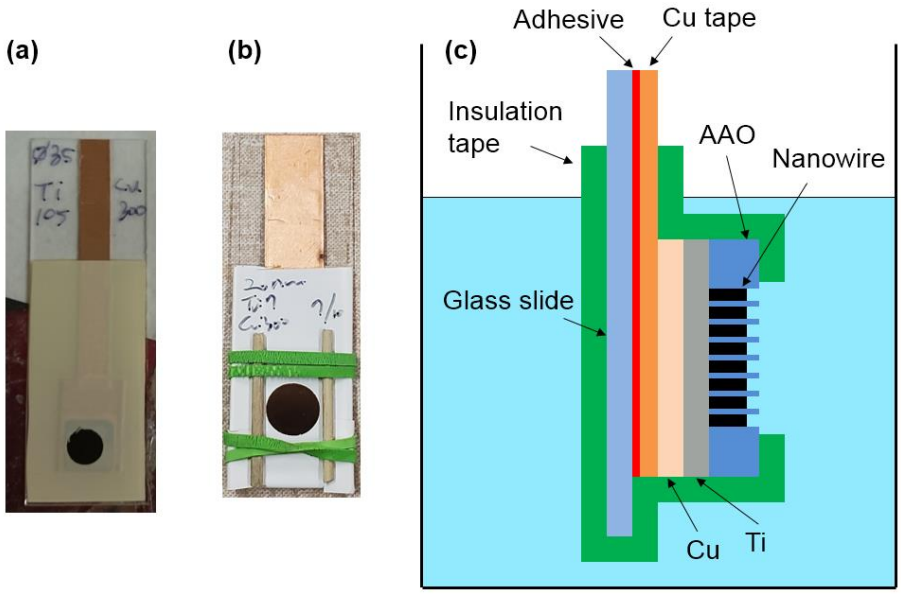

Figure 2.13. (a, b) Photo images of (a) sample and (b) sample with improved contact by wood pieces and rubber band for electrodeposition. (c) Schematic of cross-section of sample for electro-deposition.

of H_2O_2 : NH_4OH = 2 : 1. Since Ti is really thin, it is easily oxidized to TiO_2 and mostly, it doesn't affect other measurements such as high-frequency characterization measurement. If the nanowires electrodeposited need to be freed, the AAO with nanowires and 1 M NaOH are put together in a conical tube to dissolve the AAO, and the tube is sonicated. There are many AAO residues so nanowires should be rinsed with deionized water at least three times. During the rinsing, a magnetic stand is used to attract magnetic nanowires at a sidewall of the conical tube before pouring out the used deionized water. Then, ethanol is added in the conical tube to preserve the nanowires.

2.2.4. How to estimate/control nanowire length during electrodeposition

In electrodeposition, films are deposited on conductive areas only and a deposition rate is positively correlated to the amount of current used during the deposition. So, by monitoring deposited charges in the electrodeposition system, nanowire lengths can be estimated and controlled. The quantity of charge (or electricity, Q in coulombs [C]) contained in a current (I in amperes [A]) running for a specified time (t in [s]) can be calculated by $Q = I \times t$.

Assume that AAO template with 55 nm pore diameter is used in Ni electrodeposition, a deposition area is a circle with a diameter of 0.8 cm on the AAO, and porosity and pore density of AAO are 13 % and 6×10^9 cm^{-2}, respectively. If deposited charge is 8.99 C, this can be converted to the number of electrons using the amount of charge in an electron, 1.60×10^{-19} C. Then, 5.62×10^{19} electrons are used during the deposition. Ni^{2+} ions need two electrons to be reduced to Ni atom (Fe, Co, and Cu need two electrons and Au needs one electron to be reduced). It is possible to calculate the quantity of Ni atoms reduced by using 5.62×10^{19} electrons, which is simply half of the amount of electrons. Then, 2.81×10^{19} Ni atoms are reduced and this can be

converted to the mass of Ni using the atomic mass of Ni (58.6934 amu) and the Avogadro's number (6.02×10^{23}), which is $(2.81 \times 10^{19}) \times 58.6934 \div (6.02 \times 10^{23}) = 2.74 \times 10^{-3}$ g. Next, the Ni mass can be converted to the Ni volume using the Ni density (8.91 g/cm^3). So, 3.08×10^{-4} cm^3 of Ni is deposited inside the AAO template. If the porosity is used for the length estimation, the actual area of all pores is $\{\pi(0.4 \text{ cm})^2 \times 0.13\}$. Then, the estimated length is $(3.08 \times 10^{-4} \text{ cm}^3) \div \{\pi(0.4 \text{ cm})^2 \times 0.13\} = 4.71 \times 10^{-3}$ cm = 47.1 μm. If the pore density is used, the total area of all deposited pores is calculated using the number of pores in the deposition area and the area of single pore, which is $\{\pi(0.4 \text{ cm})^2 \times (6 \times 10^9 \text{ cm}^{-2})\} \times \{\pi(55 \text{ nm} \times 10^{-7} \text{ cm/nm} \div 2)^2\} = 0.0717$ cm^2. Then, the estimated length is $(3.08 \times 10^{-4} \text{ cm}^3) \div 0.0717 \text{ cm}^2 = 4.30 \times 10^{-3}$ cm = 43.0 μm. The lengths estimated using porosity and pore density are slightly different. In addition, cathode efficiency, the ratio of the actual amount (or length) of the deposited material to the theoretical amount (or length) that should be deposited, also needs to be considered since it is less than 100 % due to the hydrogen evolution.

So, after growing nanowires using specific condition and electrolyte, the actual nanowire length should be measured by SEM and the efficiency is calculated using the theoretical length based on the porosity or pore density. This efficiency can be used to estimate the nanowire length during other electrodeposition processes where the same deposition condition and electrolyte are used.

In order to estimate or control the nanowire length, the deposited charges should be monitored while electrodeposition is in progress, and the electrodeposition is stopped when the desired length is reached considering the cathode efficiency as described above.

2.3. Nanowire characterization

2.3.1. Vibrating sample magnetometry

Vibrating sample magnetometry (VSM) is a technique for measuring the magnetic moment of a sample when it is vibrated up and down perpendicularly to a uniform magnetic field. A schematic of the instrument is shown in Figure 2.14.[29] The sample is attached to the tip of a rod (sample holder) and the rod is installed between two electromagnets for the sample to be parallel or perpendicular to the direction of the magnetic field applied. The magnetic field magnetizes the sample by aligning the magnetic domains while changing the field (e.g., from an initial value to another value and turning back for magnetic hysteresis curves). Then, a magnetic dipole moment of the sample creates a magnetic field around the sample (magnetic stray field). As the sample is vibrated up and down and the magnetic field from the electromagnets is changed, the magnetic

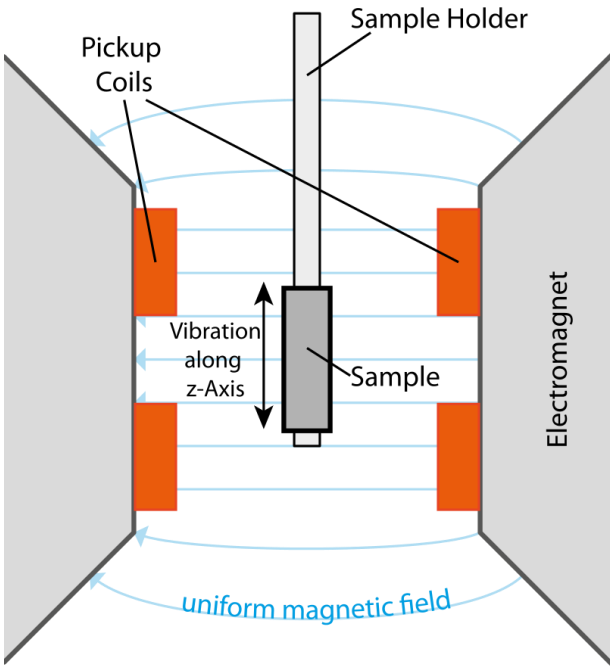

Figure 2.14. Schematic of VSM.[29]

stray field from the sample changes and this stray field change induces a voltage in pick-up coils. The voltage is proportional to the magnetic moment of the sample. By VSM, magnetic properties of materials can be measured, such as the saturation magnetization (M_s, the saturation value of magnetization of a material), the remanent magnetization (M_r, the magnetization left in a material when an external magnetic field is removed or 0), and the coercivity (H_c, the amount of magnetic field required to demagnetize a material). Also, the electromagnets of the VSM is used to provide a sweeping DC field in ferromagnetic resonance measurements of nanowires. It is discussed in Chapter 4.

2.3.1.1. How to estimate nanowire length by VSM measurement.

The saturation magnetization from magnetic hysteresis curve measurement by VSM can be used to estimate the nanowire length.

Assume that AAO template with 55 nm pore diameter is used in Ni electrodeposition, a deposition area is a circle with a diameter of 0.8 cm on the AAO, and the porosity and pore density of AAO are 13 % and 6×10^9 cm^{-2}, respectively. If the saturation magnetiztion (M_s) of Ni nanowires is 61.64 memu, the volume of Ni NWs is calculated by (61.64 memu) ÷ (485 emu/cm^3) = 1.27×10^{-4} cm^3 since the bulk M_s of Ni is 485 emu/cm^3 (the bulk M_s of Fe and Co are 1,707 and 1,440 emu/cm^3, respectively).[30] If the porosity is used for the length estimation, the actual area of all pores is $\{\pi(0.4 \text{ cm})^2 \times 0.13\}$. Then, the estimated length is $(1.27 \times 10^{-4} \text{ cm}^3) \div \{\pi(0.4 \text{ cm})^2 \times 0.13\} = 1.94 \times 10^{-3}$ cm = 19.4 μm. If the pore density is used, the total area of all deposited pores is calculated using the number of pores in the deposition area and the area of single pore, which is $\{\pi(0.4 \text{ cm})^2 \times (6 \times 10^9 \text{ cm}^{-2})\} \times \{\pi(55 \text{ nm} \times 10^{-7} \text{ cm/nm} \div 2)^2\} = 0.0717$ cm^2. Then, the estimated length is $(1.27 \times 10^{-4} \text{ cm}^3) \div 0.0717 \text{ cm}^2 = 1.77 \times 10^{-3}$ cm = 17.7 μm.

The lengths estimated using porosity and pore density are slightly different. The actual length of nanowires can be checked by SEM since these values are just estimated values. But, this is still good as a nondestructive estimation method.

2.3.2. Scanning electron microscopy

Scanning electron microscopy (SEM) is a technique that generates images of a sample by scanning with a focused electron beam. The sample surface needs to be conductive for SEM so sample coating is required to enable or improve the imaging if the sample is not conductive. The electron beam is focused on the sample surface by a set of condenser lenses. When the electron beam is bombarded on the sample surface, there are mainly two types of electrons detected: secondary electrons and backscattered electrons.

Secondary electrons occur on the surface of the sample or in an area close to the surface as a result of inelastic interactions between the primary electron beam and the sample. They are useful to get the topography of the sample surface.

Backscattered electrons occur in large areas within the interaction volume as a result of elastic collisions between electrons and atoms, causing a change in the trajactory of the electrons. Large atoms (atoms with high Z number) scatter electrons strongly compared to light atoms. This is because large atoms have a greater chance of colliding with electrons due to their sizes. So, as shown in Figure 2.15, the SEM with backscattered electrons can show the nanowire array embedded in AAO up to 1–2 μm depth from AAO cross-section surface with excellent contrast for segments. Au segments (large atoms) appear brighter than Fe segments (small atoms) in the SEM image of Fe/Au multilayered nanowires.

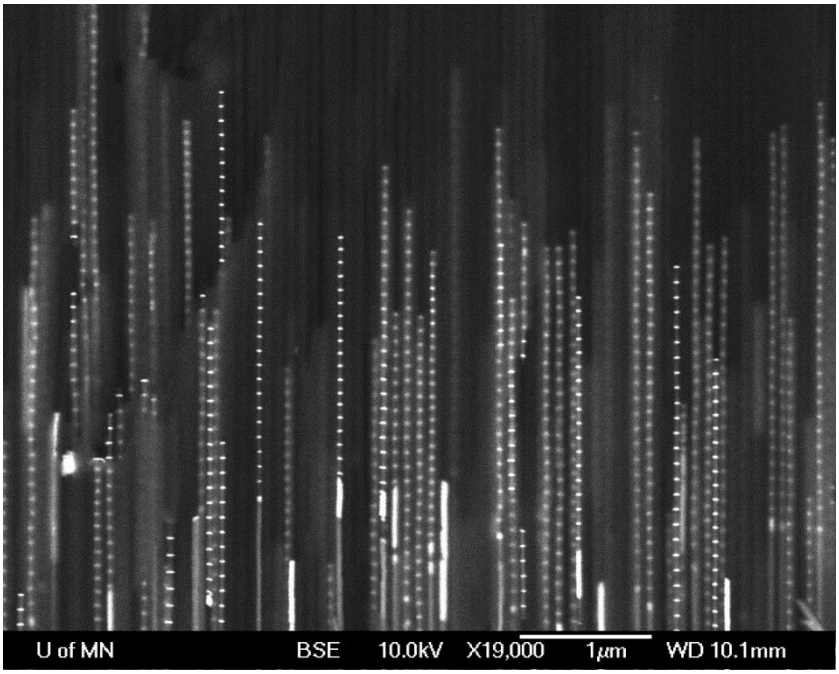

Figure 2.15. SEM backscattered electron image of AAO cross section showing Fe (gray, 100 nm)/Au (white, 20 nm) multilayered NWs in an array.

SEM can be used for the compositional analysis by detecting x-rays emitted from the sample during the electron beam bombardment, which is called energy dispersive x-ray spectroscopy (EDS or EDX). When the sample is bombarded by the elecron beam, electrons are released from the atoms at the sample surface, leaving electron vacancies. These vacancies are filled with electrons in a higher state. Then X-rays are emitted to balance the energy difference between the two electrons' states. The composition of the sample can be identified by the energy of the emitted X-rays as shown in Figure 2.16.

2.3.3. Transmission electron microscopy

Transmission electron microscopy (TEM) is a technique that generates images of a sample based on the transmitted electrons through the sample by an electron beam. Due to the transmitted

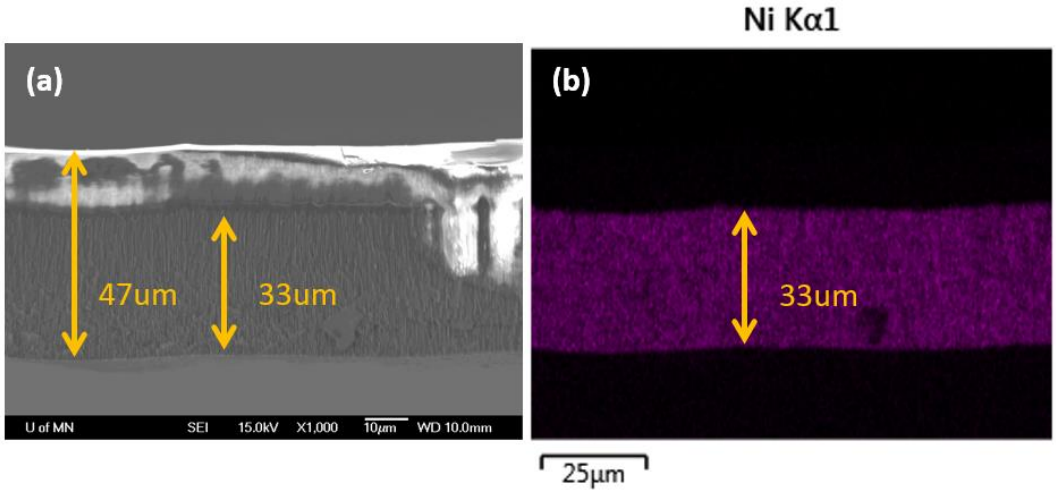

Figure 2.16. Cross-sectional (a) SEM image and (b) SEM EDS image of Ni NWs grown in AAO.

electrons, TEM provides the details about internal structures (e.g., crystal structure, dislocation, grain boundary, etc.) at the highest possible resolution, which SEM cannot give. However, samples for TEM should be thin enough for electrons to pass through and this requires additional work for sample preparation. A TEM image of Fe/Au multilayered NW is shown in Figure 2.17.

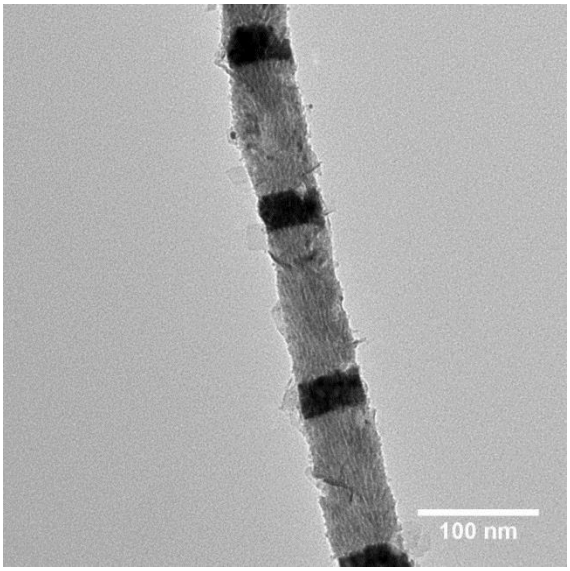

Figure 2.17. TEM image of Fe (gray, 120 nm)/Au (black, 30 nm) multilayered NW (image courtesy of Dr. Zohreh Nemati).

Chapter 3

Literature review of template-assisted electrodeposited magnetic nanowires and their properties for applications

3.1. Introduction

As discussed in 2.2.3, magnetic nanowires (NWs) can be fabricated by template-assisted electrochemical deposition, which is a relatively simple and cost-effective process compared with lithographical processes. Typical NW templates are porous anodic aluminum oxide (AAO, made by anodization of aluminum foils or films, Figure 3.1(a)) or track-etched polycarbonate (TEPC, made by ion bombardment and pore widening through polycarbonate membranes). AAO is preferred to make dense arrays of NWs because TEPC membranes usually have larger interpore distances (= smaller pore density or porosity). Pore diameters in AAO can be controlled at the nanometer scale (10–200 nm) with interpore distances about double the diameter in each case, and the pore lengths can be as long as the thickness of the membrane that is typically micrometer scale. Figure 3.1(b) shows a cross section of 34-μm-long Ni NWs in a 50-μm-thick AAO template. This means that devices with high aspect ratios (see NWs after AAO etching in Figure 3.1(c) and high-density arrays in Figure 3.1(d)) can be realized. On the other hand, the large interpore distances in TEPC enable fundamental research on magnetic properties of nearly single NWs because magnetostatic interactions between NWs will be smaller than those in AAO.

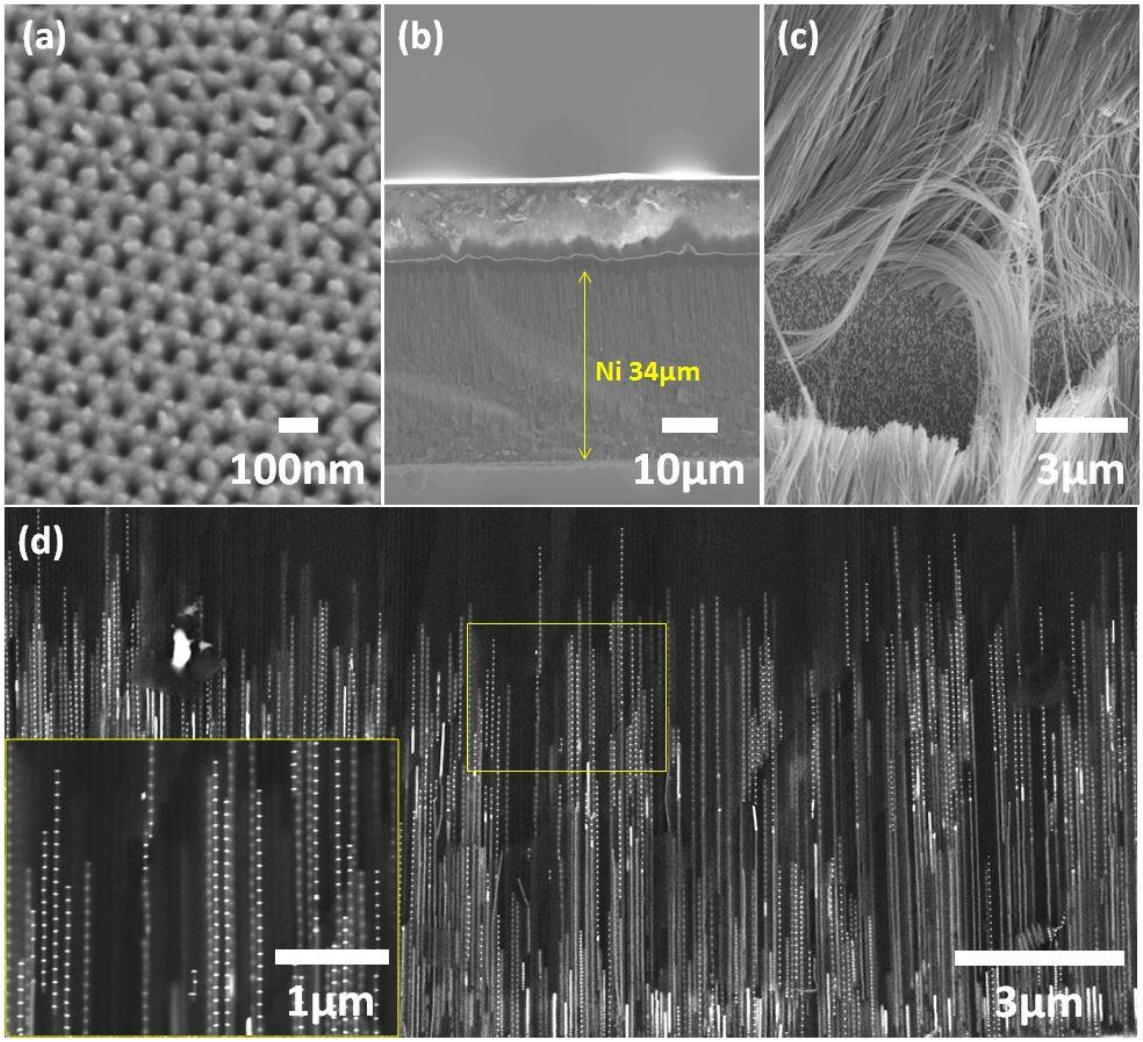

Figure 3.1. SEM images of (a) top view of AAO with 40-nm-diameter pores, (b) cross-sectional view of AAO with 34-µm-long Ni NWs grown inside, (c) freestanding Fe NWs after AAO removal, and (d) SEM backscattered image of cross-sectional view of Fe/Au multilayered NWs grown on Cu seed layer.*

The templates provide insulation and passivation for NW devices, such as hard disk drive (HDD) recording media, bit-patterned media, magnetic random-access memory (MRAM), and array read sensors. In other applications, the templates can be etched to release NWs into solutions, a feature that is desirable in many biomedical applications, such as nanoparticles for hyperthermia

cancer therapy, nanowarming cryopreserved tissues and organs, cell separation from assays, and magnetic resonance imaging (MRI) contrast imaging. As stated earlier, a range of the applications using magnetic NWs is broad, so the required magnetic properties are also varied. This chapter will review magnetic NWs with a focus on the important and application driven magnetic properties, which have been achieved at the University of Minnesota.

3.2. Fe-Ga alloy nanowires used in tactile sensors

When magnetostrictive materials are magnetized with a magnetic field, their shape or dimensions change. In reverse, when the materials are deformed, their magnetization orientation changes. This phenomenon is a good property for microelectromechanical and nanoelectro-mechanical sensors and devices. Specifically, tactile sensors have been made from magnetic NWs that are synthesized such that they are oriented vertically to thin film giant magnetoresistive (GMR) layers, similar to Figure 3.1(d). When the NWs are used as a sort of artificial skin to touch something, the deformation causes a magnetic response that the GMR sensor detects. In fact, many biological species sense touch using cilia in a similar fashion.

Three NW features are required for tactile sensors: 90-degree rotation of magnetic moments in response to applied stress, ductile mechanical properties, and low shape anisotropy. When these criteria are met, slight touches will yield large changes in magnetization (without breaking NWs) because the stress-induced rotation of magnetic moments will dominate the magnetic response.

Terfenol-D ($Tb_xDy_{1-x}Fe_2$) is known for high magnetostriction (2,000 ppm), but it is brittle and therefore difficult to machine.[31,32] Fe-Ga alloys ($Fe_{1-x}Ga_x$, $10 < x < 40$), also known as Galfenol, has reasonable magnetostriction (400 ppm)[22,31] with excellent ductility and strength.[22]

Many aspects of Fe-Ga have been extensively studied: fabrication,[22,31,33–38] magnetostriction,[33–35,39] mechanical properties,[40] and magnetic properties.[22,41–46]

In high-aspect ratio NWs, magnetic domains remain aligned along the NW axis due to shape anisotropy, so Fe-Ga alloy NWs do not show magnetostriction under applied magnetic fields or bending loads.[22,43] To rotate the domains away from the NW axis, a field larger than the shape anisotropy is required that is equal to $2\pi M_s$ (~10,000 Oe for Fe-Ga), where M_s is the saturation magnetization. Another approach is to reduce the aspect ratio of NWs using segmentation by nonmagnetic materials, for example, Au as in Figure 3.1(d) or Cu within NWs.[22,43–46] Magnetization reversal was investigated using Fe-Ga/Cu multilayered NWs composed of alternating 300-nm-long Fe-Ga and 70-nm-long Cu segments with 150 nm diameter.[43] First, an individual Fe-Ga NW with an aspect ratio of 2 was simulated with no applied field to predict the magnetic configuration at remanence (Figure 3.2(a)). Two vortex modes were seen separated by a single domain wall in the middle of the NW. Figure 3.2(b) shows that the stray fields from the ends and the middle of the NW are visible but very small. It is important to note that truly "zero" magnetic fields are unlikely, so this state is rare.

Next, an individual Fe-Ga/Cu multilayered NW was characterized by magnetic force microscopy (MFM) with the field applied. In Figure 3.3, a 550-Oe magnetic field was applied to the NW axis at different angles, showing that all of the domains were rotated and aligned in the field direction. This means that the shape anisotropy was reduced and controlled by the low aspect ratio of the Fe-Ga layers (= 2). This result is promising in that magnetization is certainly able to rotate, and therefore magnetostriction may dominate over shape anisotropy (which is < 550 Oe rather than 10,000 Oe) due to segmentation of the NW. In fact, these NWs were subsequently successfully used as pressure sensors.[45]

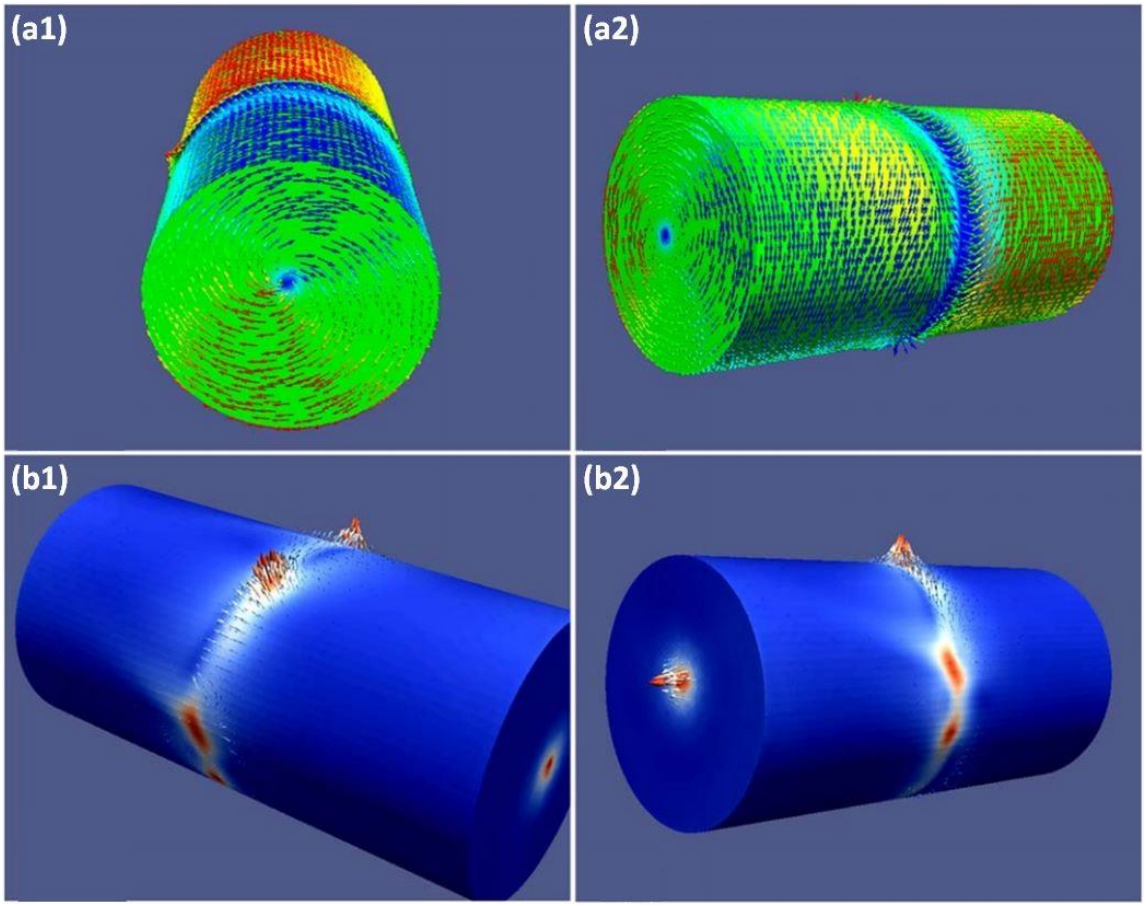

Figure 3.2. (a) Micromagnetic FEM prediction of a Fe-Ga NW with an aspect ratio of 2 and no applied field. (b) Stray fields produced from a vortex domain form at the end of the wire and the domain wall in the middle of the NW.[43]*

So, how do multilayered Fe-Ga/Cu NWs with different aspect ratios for both Fe-Ga and Cu layers behave with the field applied at different angles, and how much does shape anisotropy decrease? To answer these questions, it is useful to consider four common modes in magnetization reversal for NWs: coherent rotation (CR—all the magnetic moments coherently rotate), transverse wall (T—the moments invert progressively via propagation of a transverse domain wall, localized CR), curling (C—all the moments curl simultaneously), and vortex wall (V—the moments invert progressively via propagation of a vortex domain wall, localized C).[22,46] NWs will reverse by the

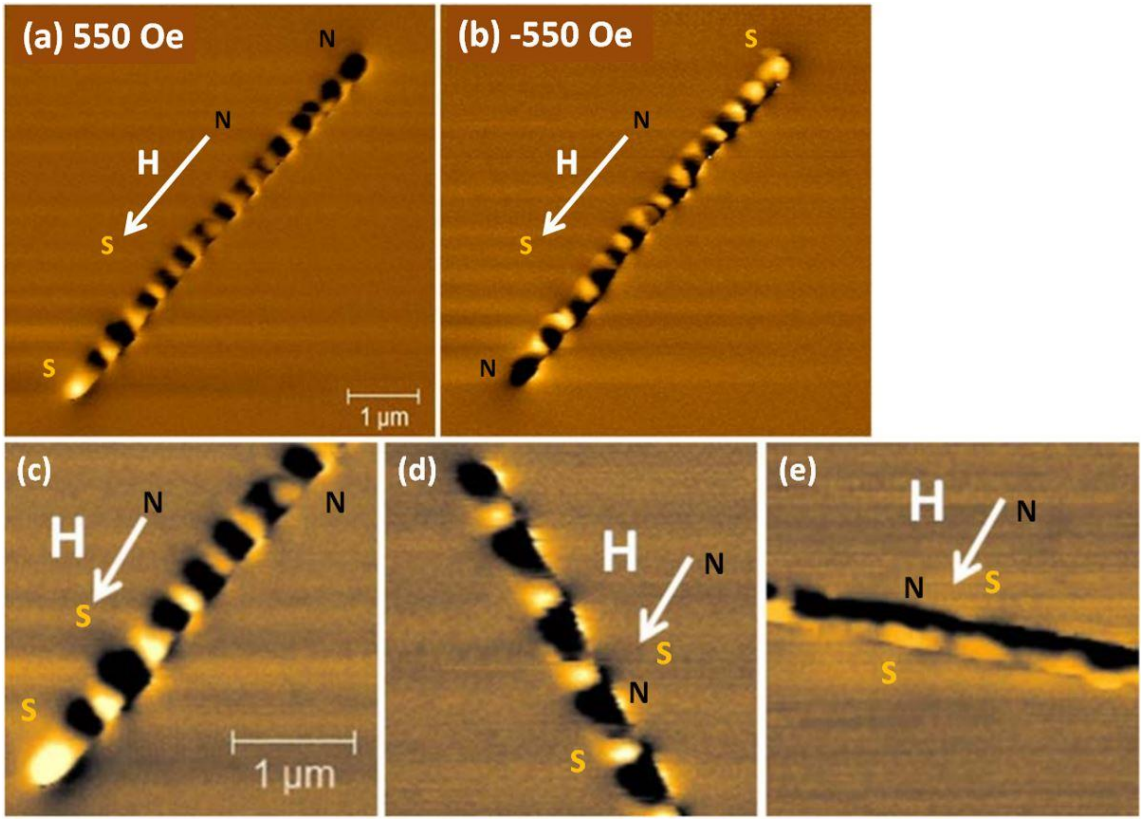

Figure 3.3. MFM images of multilayered Fe-Ga/Cu NWs with the magnetic field (550 Oe) at different angles. (a) 0 degree; (b) 0 degree, opposite direction; (c) 5 degrees; (d) 55 degrees; and (e) 105 degrees.[43]*

mechanism that requires the lowest coercivity (H_c, the amount of field required to demagnetize the NWs).[22]

Tracking coercivity helps one understand how magnetization reversal in the system occurs, and thus how to control the direction of magnetic domains, and eventually how to make the most of Galfenol in sensors. There are several theoretical predictions on magnetization reversal. First, H_c values in CR and T modes decrease, and H_c values in C and V increase with the field angle (0–90 degrees). Second, NWs can be categorized as "small" or "large" by comparing their diameters to $a\ critical\ diameter = q\frac{A^{1/2}}{M_s}$, where this $critical\ diameter$ is the size of a vortex

core; q is the smallest solution of the Bessel functions and related to the aspect ratio of the prolated spheroid, 1.8412 (a cylinder with an infinite aspect ratio) $\leq q \leq$ 2.0816 (a sphere with an aspect ratio of 1); A is the exchange stiffness constant (erg/cm), for example, $A = 10^{-6}$ erg/cm for typical ferromagnetic materials; and M_s is the saturation magnetization (emu/cm^3).[47,48]

Figure 3.4 shows the coercivity versus angle for 35- and 100-nm-diameter Fe-Ga NWs with and without Cu segments.[22,46] The thin, long Fe-Ga NWs (sample A) show vortex reversal at most field angles with an abrupt drop in coercivity near 90 degrees. This indicates that small-diameter, long NWs likely reverse their magnetizations by coherent rotation when the reverse field is applied perpendicular to the NW axes. Sample B shows increasing coercivity at 0–60 degrees and decreasing coercivity at 60–90 degrees with minimum at 90 degrees, meaning that segmented NWs experienced two competing modes (contributions of CR and V were comparable with each other): V mode at 0–60 degrees and CR mode at 60–90 degrees, resulting in a peak at 60 degrees.[22,46] This also means that the shape anisotropy of sample B was decreased relatively

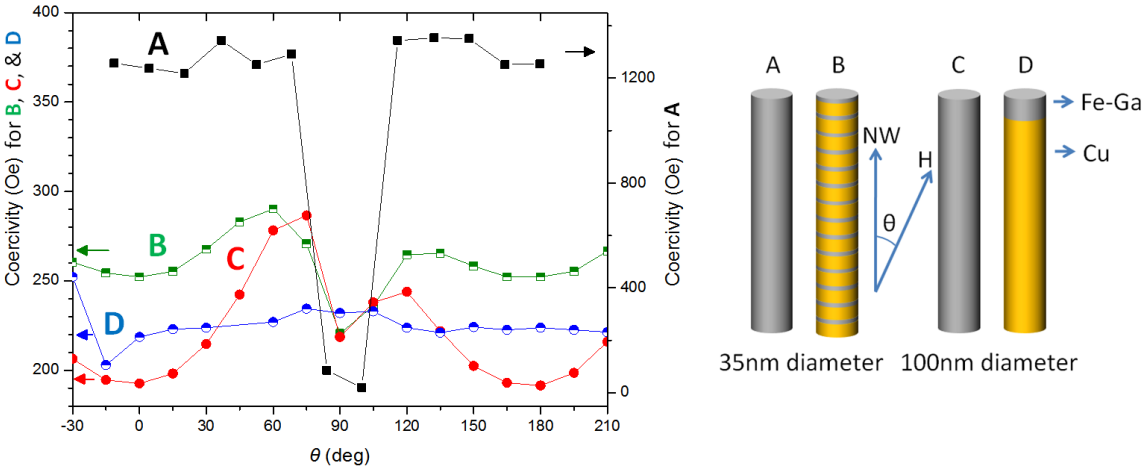

Figure 3.4. Coercivity as a function of field angle for Fe-Ga NWs: A ($AR_{Fe\text{-}Ga}$ > 55) and B ($AR_{Fe\text{-}Ga}$ 0.1/AR_{Cu} 0.3) with 35 nm diameter and C ($AR_{Fe\text{-}Ga}$ > 25) and D ($AR_{Fe\text{-}Ga}$ 0.5/AR_{Cu} 5) with 100 nm diameter, AR = aspect ratio = length/diameter.[22,46]*

compared with that of sample A at high field angles as expected due to the segmentation. Compared with sample A, the range of H_c values of sample B is narrow. But the structure of sample B is still not magnetically isotropic with the field angle.[46] This also suggests that higher aspect ratios of Cu layers would yield more magnetically isotropic samples.[46]

Next, the NW diameter was increased (sample C), and the coercivity had a distinct peak at about 70 degrees, which again indicates a competition of V and CR modes. Finally, sample D was made with Fe-Ga segments similar in length to diameter and with large separation (long Cu). This sample shows constant H_c regardless of the field angle, which indicates that the magnetization is able to rotate toward the applied field for all field angles.[22] In other words, Cu layers are thick enough to hinder dipole interactions between Fe-Ga layers. With reduced dipole interactions between Fe-Ga layers and reduced shape anisotropy within the Fe-Ga segments, this design can be used as the elements of magnetostrictive sensors or actuators, such as pressure sensor elements in Park et al.[45] Co NW arrays as well were studied and demonstrated for flow and vibration sensing.[49] There are also other studies on magnetic properties of NWs, such as magnetic configurations in individual Fe-Ga/Cu multilayered NW[42] and multiple NWs in arrays,[41,42] magnetic reversal mechanisms of Co/Cu multilayered NWs in arrays,[50] and electron holography of Co NWs for magnetization and crystalline orientations.[51]

3.3. Co/Cu multilayered nanowires for CPP-GMR structures

Giant magnetoresistance (GMR) is a phenomenon that occurs in structures composed of two ferromagnetic metals that are separated by a nonmagnetic metal. If the ferromagnetic metals are parallel- (or antiparallel-)magnetized, the resistance of the structure becomes low (or high) due to the weak (or strong) scattering caused by spin-dependent mean free paths. In measuring the

resistance, the current can be applied perpendicular to the plane (CPP) or in the plane (CIP) of the "sandwich" structure. As the importance of high areal densities of HDD and MRAM increases, CPP-GMR structures have potential for higher areal densities[52] and larger GMR effects[50] than CIP-GMR structures.

These applications are worth discussing before continuing the discussion on the NWs themselves. HDDs need GMR read sensors that are on the same scale as the magnetic bits that store data. Conventional GMR sensors are made via vacuum deposition of thin film layers that must be etched into the required size. The etching process causes damage to the sidewalls of the device, and as the device size scales ever smaller, the sidewalls make up an ever larger percent of the total sample. The next steps in fabrication of conventional hard drive read sensors is a coating of aluminum oxide (or other insulator) and side deposition of a magnetic hard bias material. Since the insulator and hard bias are only needed on the sides of the sensor, chemo-mechanical polishing is used to remove the top layers before subsequent shielding is deposited. In contrast, GMR structures can be made inside AAO, so they are already the required size and are surrounded by an insulator. Therefore, larger (easier) features can be etched in the AAO around the sensor so the etching does not touch the sensor itself. Then, a mask for hard bias layers completes the process. For GMR read sensors, the switching current density should be very high to prevent switching except by the media itself. For MRAM and STT-RAM, the switching current densities should be low such that the magnetic data can be entered at low energy consumption. In this case, GMR structures inside AAO form a very-high-density (up to 2 terabit/in.^{2}) array.

Growing multilayered NWs using relatively simple template-assisted electrodeposition can directly yield various nanometer-sized CPP-GMR structures with high density and AAO insulation. AAO usually has pore diameters in the range of 2.5–500 nm and a pore density range of 10^7–10^{12}.[53] GMR structures grown in AAO have shown better MR performance compared with

CPP-GMR structures made by conventional vacuum deposition and etching techniques that might damage the sidewalls and interfaces between ferromagnetic and nonmagnetic layers.[54–56]

A popular GMR structure involves Co/Cu multilayers. Interestingly, Co can be grown with various crystallographic orientations by varying pH during electrochemical deposition.[52] Specifically, Co/Cu multilayered NWs grown using pH 3.4 and 5.2 electrolytes have c-axis in plane (c-axis perpendicular to the NW axis) and c-axis out of plane (c-axis parallel to the NW axis), respectively.[52] Generally, the concentration of hydrogen reduced during the electro-deposition increases as the pH of the electrolyte decreases. The Co crystalline structures are considerably affected by the concentration of hydrogen absorbed and desorbed during deposition, leading to different types of Co crystalline structure.[57] More information on the relationship between pH of the electrolyte and Co crystallographic orientations is shown in Darques et al.[25,57] More information on the crystalline structure by X-ray diffraction of Co/Cu NWs is given in Tan et al.[52]

One example of device engineering using pH involves controlling the sample's two easy axes. Figure 3.5(a) shows the hysteresis loops of Co with an in-plane Co c-axis (pH 3.4) and an in-plane shape anisotropy (i.e., low aspect ratio of 0.083 from 60 nm diameter and 5 nm thickness).[52] Figure 3.5(b), however, shows the hysteresis loops of Co where the c-axis was grown perpendicular (pH 5.2) to the same shape anisotropy. The in-plane anisotropy is obvious in Figure 3.5(a), but Figure 3.5(b) shows almost identical loops because the NWs have two competing easy axes, so the same reversal behavior is observed irrespective of the saturation direction.[52]

Then, how do different crystallographic orientations in Co/Cu NWs affect the magneto-resistance (MR)? MR was measured using an AC transport system, applying a 10 μA bias current through the top to bottom layers of NWs.[52] MR is calculated by $MR = \left[\frac{R(H)-R(H_{sat})}{R(H_{sat})}\right] \times 100\%$,

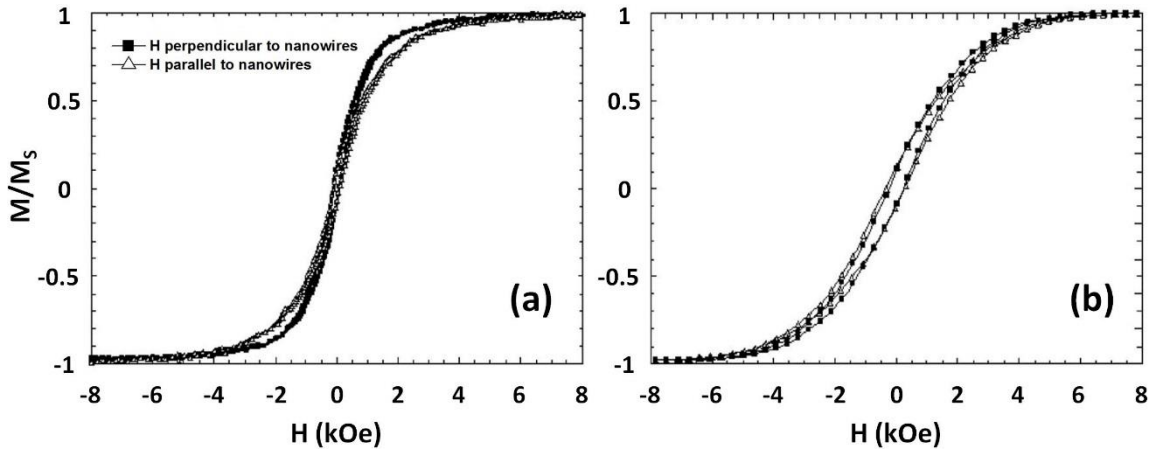

Figure 3.5. Magnetic hysteresis loops of Co/Cu multilayered NWs at room temperature. (a) Co 5 nm/Cu 10 nm NWs grown at pH 3.4, (b) Co 5 nm/Cu 5 nm NWs grown at pH 5.2.[52]*

where H_{sat} is the saturated field.[52] As shown in Figure 3.6(a, b), Co/Cu NWs with c-axis in plane (pH 3.4) have 0.08% MR difference when the field is applied parallel to NWs versus perpendicular. However, Co/Cu NWs with c-axis out of plane (pH 5.2) have 1.33% MR angular variation due to the two easy axes.[52] When Co/Cu NWs have in-plane c-axis, the remnant magnetizations are likely to stay along in plane because both Co shape anisotropy and c-axis are in plane (Figure 3.6(c)).[52] However, when Co/Cu NWs have out-of-plane c-axis, the remnant magnetizations remain in plane after in-plane saturation (following shape anisotropy) but perpendicular to the plane after perpendicular saturation (following the c-axis) (Figure 3.6(d)). In this out-of-plane orientation, it is more favorable for the magnetizations to form domains due to dipole fields between the Co layers. By this research, we found that hysteresis loops and MR measurements provide different but complementary information on multilayered Co/Cu NWs and also that isotropic MR properties were suitable for further CPP-GMR researches.[45,54–56,58,59]

Specifically, switching current densities can be lowered in Co/Cu multilayered NWs for low-energy MRAM,[58,59] and switching current densities can be increased in Co/Cu/Co trilayered

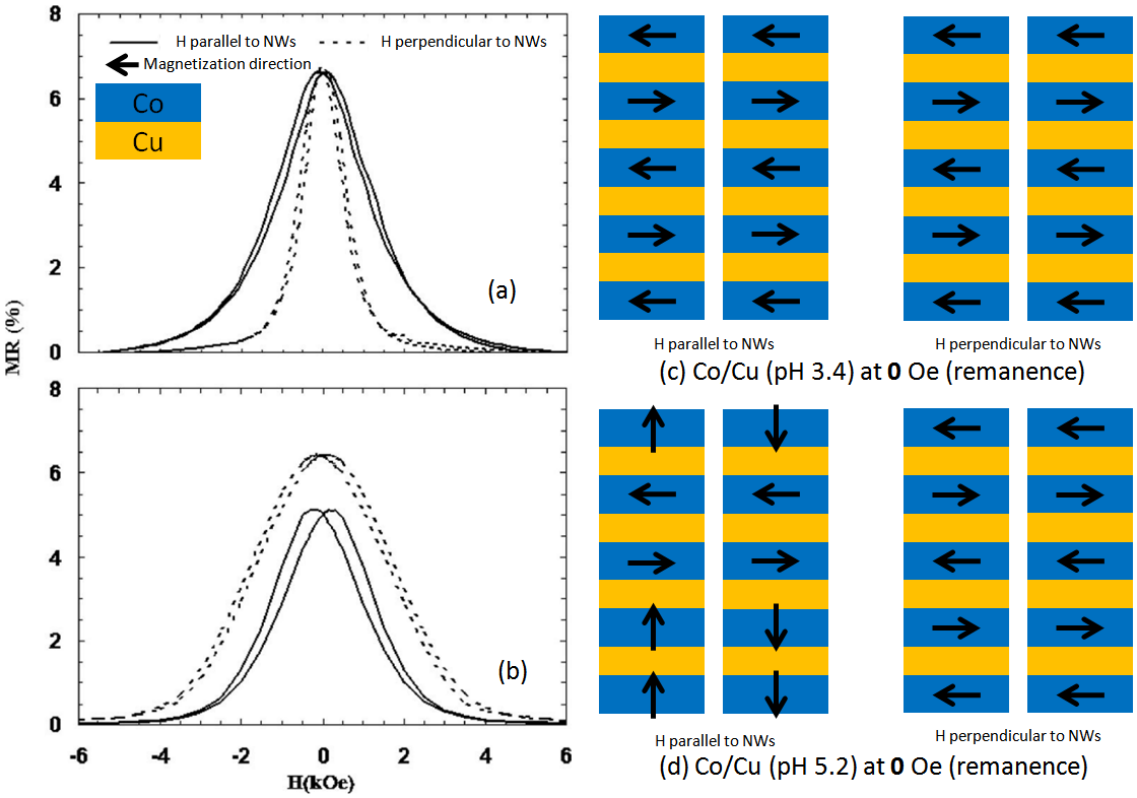

Figure 3.6. Magnetoresistance of Co/Cu multilayered NWs at room temperature. (a) Co 5 nm/Cu 10 nm NWs grown at pH 3.4, (b) Co 5 nm/Cu 5 nm NWs grown at pH 5.2, and possible magnetization configuration at remanence of two adjacent Co/Cu NWs grown at pH 3.4 (c) and at pH 5.2 (d).[52]*

structures for read head sensors with improved head stability.[54–56] It is noted that smaller numbers of layers in structures yield higher switching current densities and less read sensor noise.[54] In addition, while researching nanometer-sized CPP-GMR for high areal densities, low-resistivity NWs were also explored,[54,56] which could be crucial for interconnects in the near future.

3.4. Nanowires used for biomedical applications

Biomedical applications include cell labeling and identification, MRI contrast agents, and nanowarming agents. For cell labeling, the goal is to have a multitude of labels that can be coated to tag specific biomarkers. These labels should then have a physical mechanism to identify their presence in an assay or other location so that the medical personnel know the cell of interest is present. Possible magnetisms of identification in assay form will be discussed in the succeeding text. In tissue, the label could be identified by MRI if the imaging contrast is high enough. Another biomedical application is nanoheating, which relies on inductive hysteretic losses as either NWs or nanoparticles (NPs) are exposed to an external alternating magnetic field. For a decade or so, there has been interest in using this phenomenon to kill cancer by hypothermia therapy. The idea is to coat the nanostructure such that it adheres best to a tumor and/or tumor cells. The heating would then be local to the tumor for maximum cell death, while surrounding healthy tissue is left cool. A new use of hysteretic losses is nanowarming of cryopreserved tissues and organs. In this application, nanostructures suspended inside a cryoprotectorant (i.e., a biocompatible antifreeze) would be frozen inside and outside of the tissue or organ such that rapid, uniform rewarming is possible. To avoid detrimental crystallization during warming, the heating rate should be well above 50 °C/min.

So far, NWs are not approved by the US Food and Drug Administration, but a few NPs of iron oxide have been approved.[60,61] Magnetic NWs may become approved with further research because they do have several advantages over NPs of comparable volume. First, NWs have higher surface-to-volume ratio that enables loading of more coatings for drug delivery.[2,3] Second, multiple functionalities are possible with multilayered NWs with "barcoded" surface chemistries.[4] Third, NWs can be mechanically rotated for torque-induced dynamic cell therapy using a relatively weak external field due to the larger magnetic moment and higher aspect ratio.[2,3,5,6] In

the near future, more magnetic nanomaterials and nanotechnologies could be used in diagnosis and treatment of illnesses like cancer. Then, techniques for cell labeling and identification also should be necessary; otherwise, both unhealthy and healthy cells would be destroyed during treatment. Sharma et al.,[3,6,62] Shore et al.,[63] and Zhou et al.[64] show how to label cells with NWs and how to separate these cells from unlabeled ones. NWs can also be selectively functionalized using antibodies to label different cell types so that each type of NW will match a specific cell type.[6] For example, Ni and Co NWs can be coated with different antibodies so that Ni NWs will label cancer cells only and Co NWs will label immune cells only.

Then, if magnetic NWs are used for this cell labeling and identification, what kinds of magnetic properties can be utilized for cell identification? Magnetization hysteresis (MH) loops could be used to count labels if one kind of NW is used to label cells.[3] For example, when Ni NWs (3 μm long with 100 nm diameter) were coated with Arg-Gly-Asp (RGD), osteosarcoma (bone cancer) cells were shown to self-disperse the NWs throughout the cell population by integrin-mediated responses with low cytotoxicity.[3] To show the potential of hysteresis loop quantification, 300-μL samples with varied concentrations of dispersed Ni NWs in deionized (DI) water were measured, and a reliable linear relationship between magnetic moment and Ni NW volume was clearly demonstrated, as shown in Figure 3.7.

However, it would be hard to distinguish two or more kinds of NWs in a single assay since MH loops simply show the net moment of the entire sample and the loops vary with orientation. Another proposed "read out" technique was H_c versus applied field angle, as in Figure 3.4. Although this technique can distinguish which one of many types of NWs might be present in an assay, it does not delineate mixtures of NWs very well.

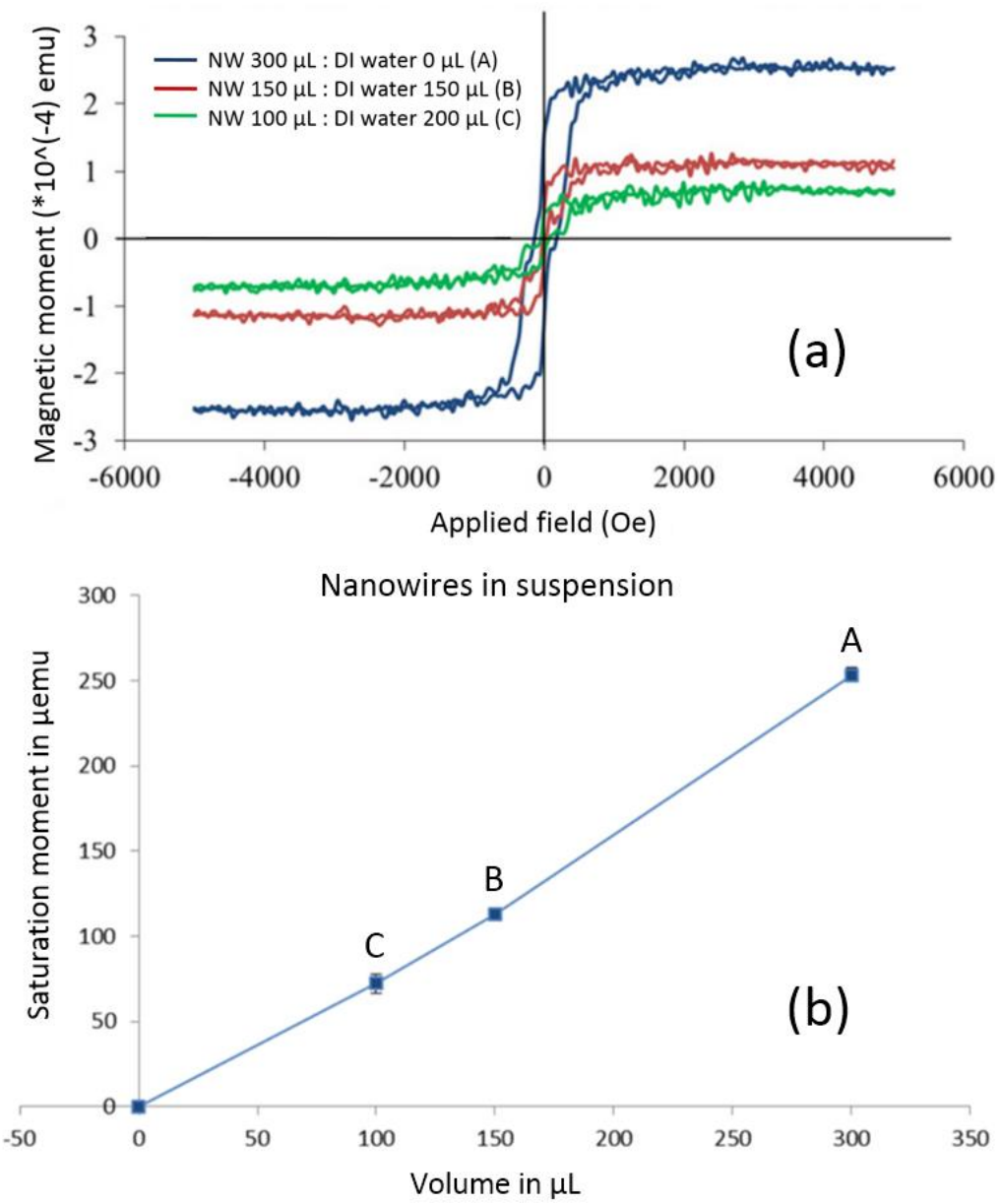

Figure 3.7. (a) MH loops obtained for 100-µL samples from Ni NWs 300 µL with DI water 0 µL, Ni NW 150 µL with DI water 150 µL, and Ni NW 100 µL with DI water 200 µL. (b) Moment versus Ni NW volume relationship in cell culture medium.[3]*

First-order reversal curve (FORC) measurements, however, were efficiently used to distinguish two different types of NWs.[62] In FORC, if a sample is saturated at a high positive field,

then the magnetic moment of a sample is measured as the magnetic field (H) is swept from a progressively lower reversal field (H_r) back to saturation. The measurements from each reversal field are compiled into a family of curves from which the FORC distribution $\rho(H, H_r) = -\frac{1}{2}\frac{\delta^2 M_{FORC}(H,H_r)}{\delta H \delta H_r}$ is calculated plotted in a plane of $H_u = \frac{H+H_r}{2}$ (as y-axis) and $H_c = \frac{H-H_r}{2}$ (as x-axis), where H_u is interaction field and H_c is coercivity.[62,65] As one example, FORC measurements were used to estimate the ratios of two kinds of Ni NWs from mixtures.[62] Here, high coercivity labels (at low field angles) were engineered by ensuring coherent rotation as the reversal mechanism because, at 5 μm long and 18 nm diameter, their diameters were too small to have a vortex core.[62] Low coercivity labels were engineered by ensuring the diameters were large enough to support a vortex wall reversal mechanism (6 μm long and 100 nm diameter).[62] Four mixtures were studied with NW ratios of 100 nm:18 nm equal to 1:0, 1:23, 1:115, and 0:1, and these four samples were measured by FORC as in Figure 3.8.[62]

The end samples 100 nm:18 nm = 1:0 and 100 nm:18 nm = 0:1 were found to have coercivities of 370 and 730 Oe, respectively, and these FORC curves were used in a regression analysis to estimate the ratios of the other two mixtures.[62] The estimated ratios were compared with the known ratios, and the regression analysis was linear with the expected ratios for samples b and c in Figure 3.8: $\rho_b = 1.2\,\rho_{a_{100\,nm}} + 0.75\,\rho_{d_{18\,nm}}$ and $\rho_c = 0.28\,\rho_{a_{100\,nm}} + 0.81\,\rho_{d_{18\,nm}}$, respectively, as shown in Figure 3.8(e).[62] To get the accurate ratios between the numbers of 100 and 18 nm diameter NWs, their volume ratio should be considered and used for further analysis, which is $\frac{Vol_{100\,nm}}{Vol_{18\,nm}} = \frac{\pi\times(50\,nm)^2\times 6\,\mu m}{\pi\times(9\,nm)^2\times 5\,\mu m} = 37$ (meaning that the volume of one of 6-μm-long and 100-nm-diameter NW is equal to that of thirty seven of 5-μm-long and 18-nm-diameter NWs) since the magnetic moment is proportional to the volume.[62]

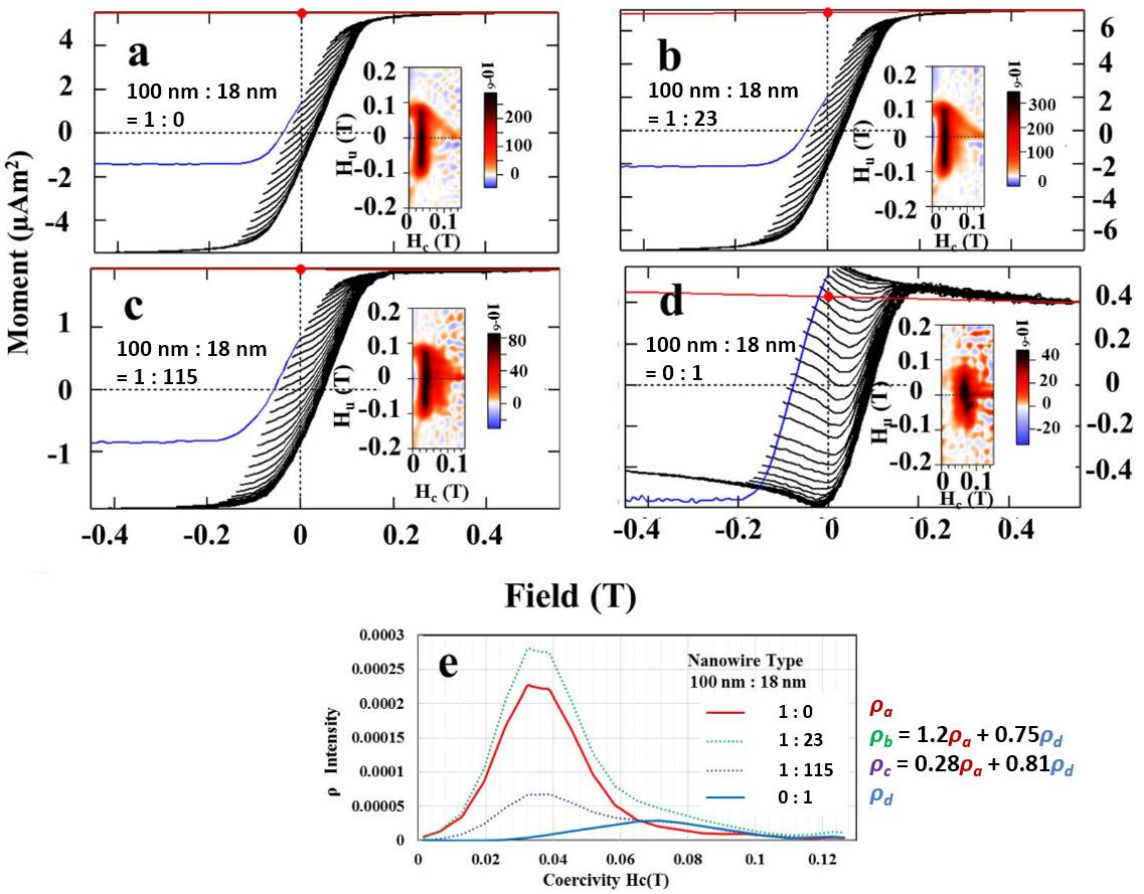

Figure 3.8. FORC measurements by VSM for NW ratios of 100 nm:18 nm equal to (a) 1:0, (b) 1:23, (c) 1:115, and (d) 0:1 with insets of FORC analysis (ρ vs. H_c vs. H_u). (e) Integrated intensity of horizontal slices across each FORC with each intensity formulas based on the regression analysis on the right.[62]*

For sample b, 100 nm:18 nm = 1:23 sample, if the ratio of the intensities of two types of NWs is $\rho_{a_{100\,nm}}/\rho_{d_{18\,nm}} = 1.2/0.75$ (since $\rho_b = 1.2\,\rho_{a_{100\,nm}} + 0.75\,\rho_{d_{18\,nm}}$), then numerical ratio of the two types of NWs is $\frac{N_{100\,nm}}{N_{18\,nm}} = \frac{\rho_{a_{100\,nm}}}{\rho_{d_{18\,nm}}} \div \frac{Vol_{100\,nm}}{Vol_{18\,nm}} = \frac{1.2}{0.75} \div 37 = \frac{8}{185} \sim \frac{1}{23}$.[62] For sample c, 100 nm:18 nm = 1:115 sample, if the ratio of the intensities is $\rho_{a_{100\,nm}}/\rho_{d_{18\,nm}} = 0.28/0.81$ (since $\rho_c = 0.28\,\rho_{a_{100\,nm}} + 0.81\,\rho_{d_{18\,nm}}$), then concentration ratio is $\frac{N_{100\,nm}}{N_{18\,nm}} =$

$\frac{\rho_{a_{100\,nm}}}{\rho_{d_{18\,nm}}} \div \frac{Vol_{100\,nm}}{Vol_{18\,nm}} = \frac{0.28}{0.81} \div 37 = \frac{28}{2997} \sim \frac{1}{107}$.[62] This value is within 7% error of the known value, which is very good for such a large difference in NW concentrations between these two types of NWs with such different volumes. Therefore, FORC analysis can be a good way to distinguish mixtures of more than two NWs.

Ferromagnetic resonance (FMR) measurements are another way to distinguish between different types of NW labels.[64] FMR occurs when an AC magnetic field is applied to a magnetic material at a frequency (f) that matches the material's natural electron precession frequency. This precession frequency can be altered using a DC magnetic field, according to the well-known Kittel equation: $\left(\frac{\omega}{\gamma}\right)^2 = \left[Hcos(\theta - \theta_H) + H_{eff}cos2\theta\right]\left[Hcos(\theta - \theta_H) + H_{eff}cos^2\theta\right]$,[66] where ω is the angular frequency ($\omega = 2\pi f$), γ is the gyromagnetic ratio ($\gamma = \frac{g\mu_B}{\hbar}$, where g is the g-factor of the material, μ_B is the Bohr magneton, $\hbar$ is the reduced Plank constant), H is the applied DC field, θ is the angle between magnetization direction and NW axis, and θ_H is the angle between the applied DC field and NW axis as in Figure 3.9.

H_{eff} is the effective field that the NWs experience, and it is a combination of the shape anisotropy field of the NW itself and the magnetostatic interaction field resulting from nearby

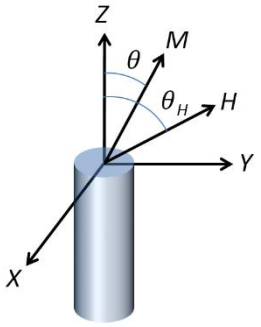

Figure 3.9. Relative orientations of magnetization (M) and external DC magnetic field (H) for single NW.*

NWs. These two fields dominate over others, such as magnetocrystalline anisotropy field and magnetoelastic anisotropy field.[25] Therefore, H_{eff} is expressed as $H_{eff} = 2\pi M_s(1 - 3P)$, where M_s is the saturation magnetization and P is the porosity of the template in which NWs are grown.[25] In addition to dimensional factors, ferromagnetic materials such as Fe, Co, and Ni have different g-factors and saturation magnetizations, so NWs can easily be designed to show many unique FMR behaviors. For FMR measurements, radio frequency (RF) signal is applied to a coplanar waveguide on which the NW samples are placed. If the frequency of the RF signal matches the resonance frequency of the NWs, an intensity reduction occurs in the S_{21} magnitude, which is a ratio of the output voltage and input voltage of RF signals. To verify the cell labeling using FMR and emulate the mixture of different types of NWs, three types of NWs (18-μm-long Ni, 15.5-μm-long Co, and 10.5-μm-long Fe NWs with 40 nm diameter) were measured individually and in stacks (Ni-Co-Fe and Ni-Fe-Co from bottom to top).[64]

Figure 3.10(a) shows FMR measurements for individual NW types as dashed lines and two measurements of stacked types as solid lines. The Ni-Co-Fe stacks had three absorption peaks for S_{21}, representing each individual type of NW. However, when the Co NWs were further from the coplanar waveguide, as in the Ni-Fe-Co stack, only the absorption peaks of Fe and Ni were obvious. Zhou et al.[64] also provides an algorithm detecting multiple NW types and showing the contribution of each to the overall S_{21} magnitude shape as in Figure 3.10(b, c). This FMR measurement technique shows its ability to detect three different types of NWs. Theoretically, this technique can detect many types of NWs as long as NWs are made of different elements or alloys since they have all different FMR signals. For cell labeling and identification using two or more types of NWs, FORC and FMR techniques have strong potential as described earlier and even stronger if they are used together. Furthermore, these techniques can be combined with fluorescence techniques because these three techniques are orthogonal (noninterfering).

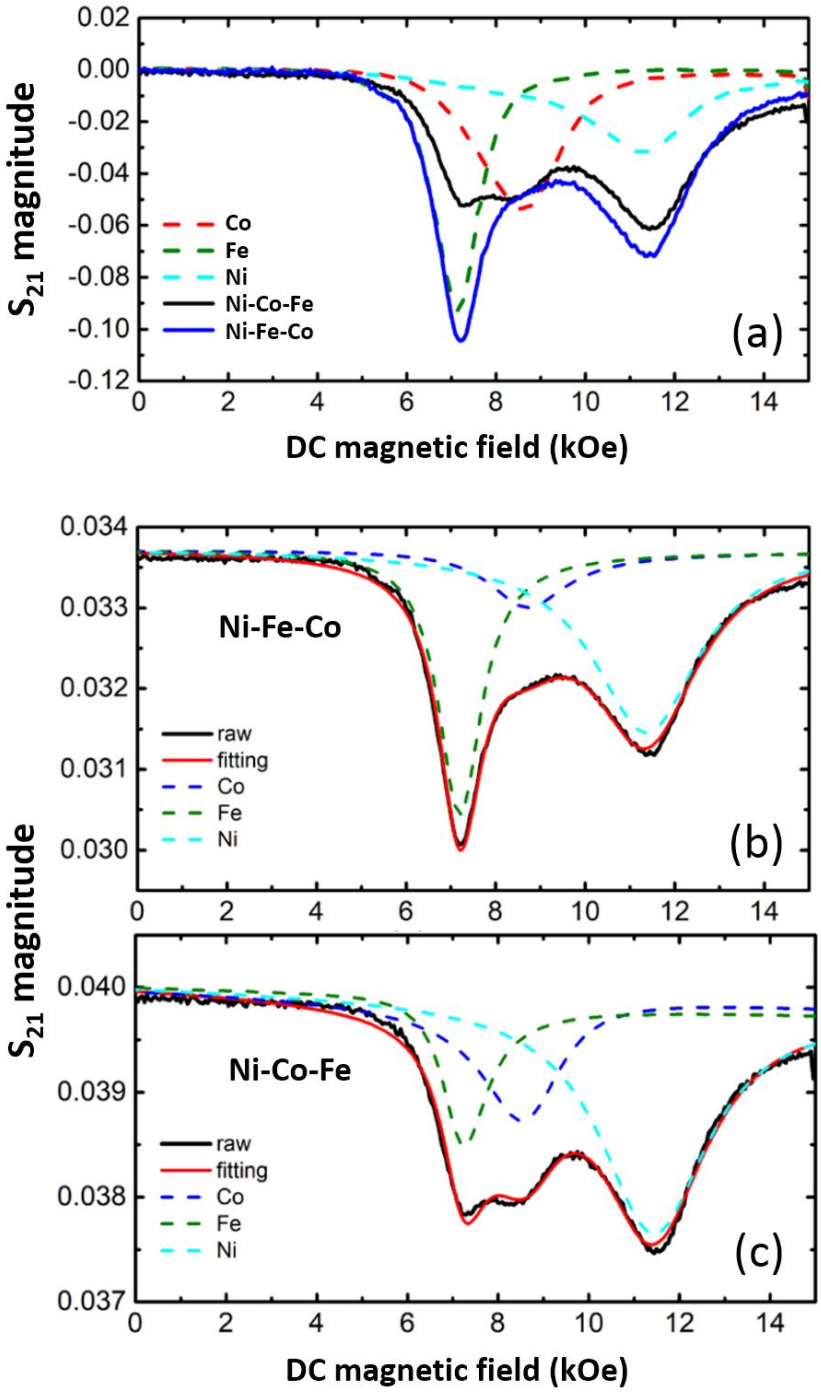

Figure 3.10. (a) FMR measured for three types of NWs (Fe, Co, and Ni NWs) as dashed lines and stacks of Ni-Co-Fe and Ni-Fe-Co as solid lines. (b and c) FMR raw data and fitting curves as solid lines and contribution of each type of NWs as dashed lines from (b) Ni-Fe-Co stack and (c) Ni-Co-Fe stack.[64]*

NWs can also be used as MRI contrast agents. For example, Fe/Au multilayered NWs exhibited a contrast performance comparable with commercial Fe oxide nanoparticles and showed multiple functionalization capabilities, because of the multilayered structure, which could enable specific tissue imaging and therapy.[67] Furthermore, after systematically controlling the electrodeposition of Co-Fe alloy NWs,[48] Au-tipped Co-Fe alloy NWs were studied as nanowarming agents for cryopreservation.[68] Their very high saturation magnetization led to nanowarming rates of 1000 °C/min, 20 times faster than critical warming rate (50 °C/min) for common cryoprotective agents. This fast rate means that the preserved sample (e.g., tissues or organs) could be heated without crystallization, and the nanoscale dimensions of the NWs would enable them to be evenly dispersed (e.g., in blood vessels) for uniform heating. The NWs were shown to have low cytotoxicity.[6,68] Although Au is a literally a "gold standard" for biocompatibility, electroplated Au often involves cyanide electrolyte chemistry. For bio-related applications, a thiosulfate-sulfite electrolyte, which is a noncyanide solution, was recently proven successful for NW deposition.[69] Galfenol has also been studied for remote microactuators for cell biology studies and intracellular applications.[70]

3.5. Long-range ordered porous AAO fabricated by double imprinting with line-patterned stamps

NWs are frequently grown inside porous AAO by electrodeposition, but the pores of AAO typically have only short-range order as naturally formed during conventional two-step anodization of aluminum (Al), usually in the range of 20 times the interpore distance.[71] It would be great to make long-range ordered AAO so that NWs or devices can be grown densely at a known location and pinpointed easily for applications, such as HDD recording media, bit-

patterned media, and MRAM. Conveniently, long-range ordered AAO is possible with imprinting methods[35,54,55,72] in which stamps with hexagonally ordered arrays of nanopillars (as in Figure 3.11(a)) are pressed into Al foils or Al films and the resulting dents guide the pore growth during subsequent anodization. Figure 3.11(b) shows pores formed in an AAO (oxide) grown using imprinted Al and the pores naturally occurring in unimprinted areas during anodization.[72] The stamps were conventionally made by e-beam lithography, which is an expensive and very slow process to make billions of nanopillars over large areas (square millimeter scale).

Therefore, line-patterned Si stamps have been developed (simpler patterns and even commercially available for cheap prices).[56] Although Si stamps with line patterns are brittle for imprinting, Ni can be electrodeposited onto Si masters such that the deposited Ni films (with duplicate line patterns) can be used as stamps for imprinting. The original Si stamps can be reused to make many Ni stamps. These Ni stamps then are imprinted, rotated 60 degrees, and imprinted again on the Al precursors to make double-imprinted areas from which the nanopores will grow during anodization as in Figure 3.12.

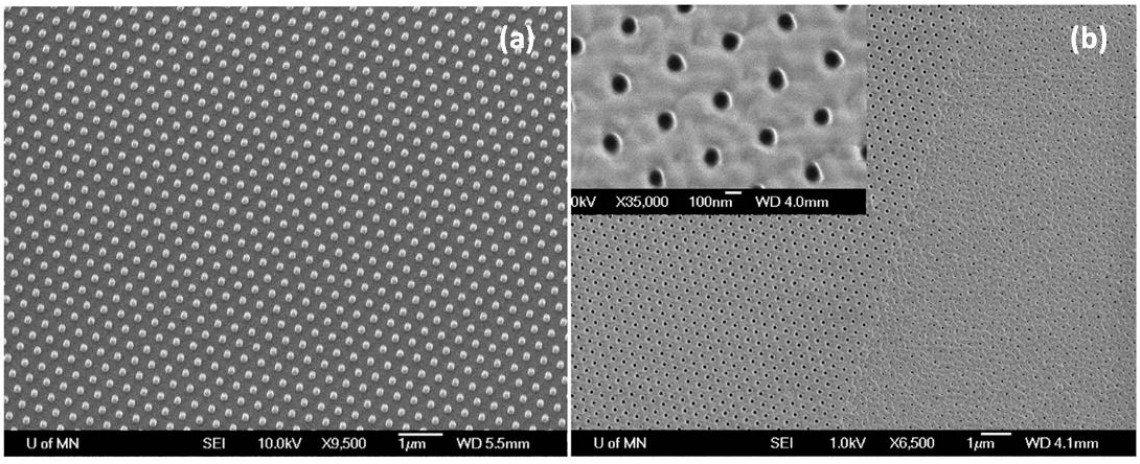

Figure 3.11. SEM image of (a) stamp with nanopillars and (b) nanopores from imprinted (left) and unimprinted (right) areas.[72]*

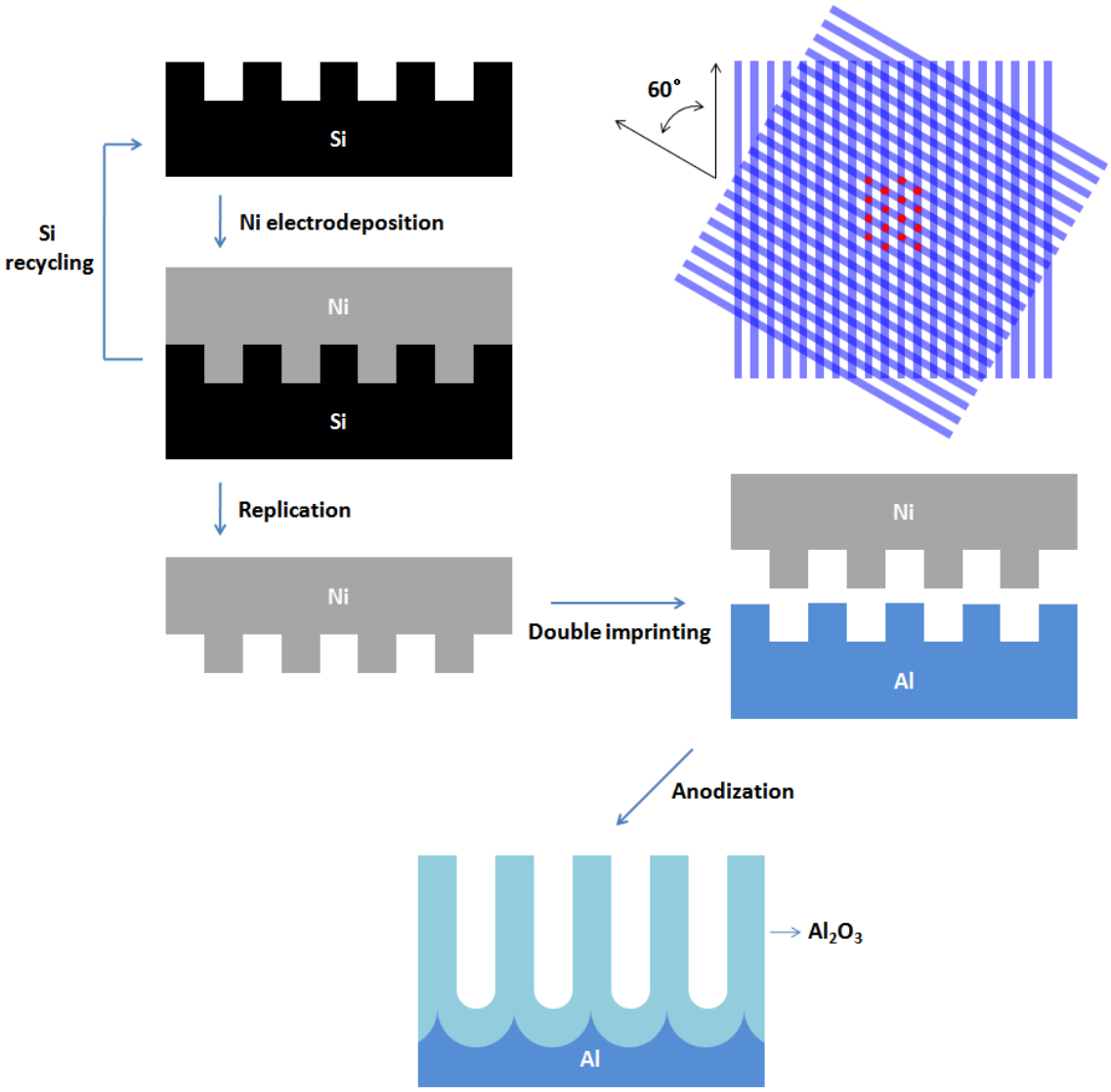

Figure 3.12. Schematic diagram of fabrication of long-range ordered AAO by double imprinting with line-patterned Ni stamps replicated from Si master stamps. Red dots are shown for pore locations that will result if double-imprinted Al is oxidized via anodization to form AAO templates.*

Figure 3.13(a) shows the line pattern on a Ni stamp, and the inset shows the whole Ni sample, which is 1 × 1 cm. The pattern looks blue since the line pattern period demonstrated here is 278 nm, and blue light is diffracted off the Ni stamp at specific viewing angles. When the Al

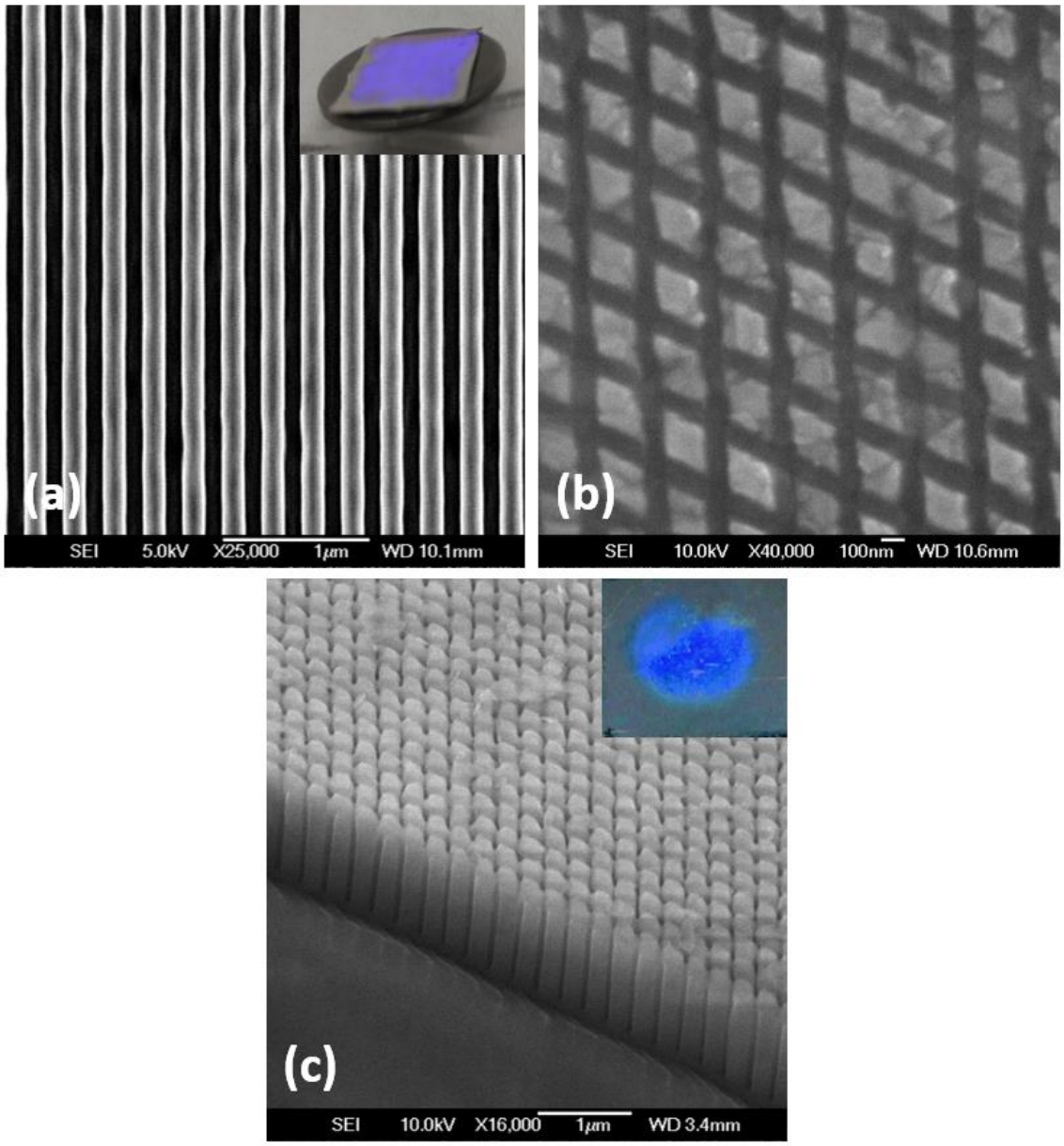

Figure 3.13. SEM images of (a) top view of line pattern on Ni stamp with inset showing the Ni stamp, (b) top view of double-imprinted Al precursor, (c) AAO by anodization after double imprinting with inset showing the ordered nanoporous region by double imprinting with inset showing the ordered nanoporous region by double imprinting (seen as a blue area) and short-range ordered region naturally formed in nonimprinted region (seen as a gray area).[56]*

precursor is double imprinted with this Ni stamp, the imprint pattern is shown in Figure 3.13(b).

After the anodization of the imprinted Al, the resulting oxide contains pores with long-range order as in Figure 3.13(c). The inset of Figure 3.13(c) shows AAO with the patterned region that has ordered pores over 1 cm diameter (blue area) surrounded by natural short-range ordered pores in the region that was not imprinted (gray area).

The techniques to make large-scale long-range ordered AAO are interesting to template-assisted fabrications for nanostructured materials. Double imprinting could be the simplest and most cost-effective method. The AAO made by this method shows the potential for the future high-density recording systems requiring long-range ordered devices separated from each other by insulating material to eliminate cross talk, such as 3-D magnetic memory.

3.6. Conclusions

Magnetic nanowires (NWs) grown by template-assisted electrochemical deposition have gathered great attention for nanometer-sized features made by relatively simple and low-cost processes and unique magnetic properties due to their high aspect ratios and high densities. Thus, there are many applications using magnetic NWs and many magnetic properties that need to be engineered depending on these applications. To get the magnetostriction effect from Fe-Ga alloy NWs, the shape anisotropy should be negligible by using nonmagnetic materials such as Cu to segment the NWs. Fe-Ga/Cu and Co/Cu multilayered NWs and Co NWs were all studied as individual NWs and as arrays to determine each of their magnetic switching mechanisms. For Co/Cu multilayered NW-based CPP-GMR structures for future MRAM and read head sensors, high or low magnetoresistance is achieved using either a trilayer or Co/Cu NWs with in-plane shape anisotropy due to low aspect ratio and in-plane c-axis of Co, respectively. In cell labeling and identification, FORC analysis has been used to estimate the proportion of two different types

of NWs in mixtures and FMR measurements to detect three types of NWs. Combining these two techniques and fluorescence techniques could yield a powerful tool for cell analysis. Fe/Au multilayered NWs and Au-tipped Co-Fe alloy NWs show promise as MRI contrast and nanowarming agents, respectively. Finally, NWs or devices made by template-assisted electrodeposition can be enhanced in terms of material quality and magnetic property if long-range ordered AAO is used. A simple and cost-effective double imprinting technique using line-patterned Ni stamps is demonstrated and could be applied to future memory devices, such as 3-D magnetic memory that requires well-ordered and densely close-packed monodisperse nano-devices with insulation between them.

Chapter 4

Magnetic nanowire biolabels using ferromagnetic resonance identification

The nanowire fabrication and characterization as well as data analysis in this chapter were done by the author who thanks Yali Zhang of Prof. Franklin's research group for the FMR measurements.

4.1. Introduction

The ubiquitous application of radio-frequency identification (RF-ID) has recently reached nano-dimensions.[73–75] Nano-identification markers would be a useful addition to nanomaterials already in use in a variety of fields, including drug delivery,[76,77] hyperthermia therapy,[77,78] cell manipulation,[79,80] cell separation,[81] cryopreservation,[68,82–84] ferrogels,[85] and circulators in high-frequency circuits.[86] Magnetic nanowires (MNWs) in particular have shown promise for labeling cells for a specific therapy,[2–4,6,32,62,87] and these MNWs can have unique magnetic signatures to identify and/or distinguish the cells in an assay.[6,62,64] For read-out, first-order reversal curve (FORC) analysis has been shown to distinguish mixtures of two types of nickel MNWs with a high accuracy.[62] Other techniques that are excellent for characterization, such as hysteresis curves and angle-dependent coercivity,[3,22] do not detect individual signatures well, and FORC

measurements are slow unless the projection method or backfield remanence is used.[88] Faster measurements are being explored, including ferromagnetic resonance (FMR) which has potential to identify many high frequency signatures simultaneously.[64]

FMR measurements of magnetic nano- and microwires have been used to study magnetization dynamics for both fundamental and applied research.[19,25,57,66,89–106] However, FMR has merely been used as a measurement technique to date. Recently, Zhou et al. introduced FMR readout of MNWs as biolabels using the broadband FMR technique (also called the vector network analyzer (VNA)-FMR technique) based on coplanar waveguides (CPWs) with a focus on a fitting algorithm for detecting multiple MNW types using a mathematical model.[64] For FMR measurements, generally microwave circuit structures such as waveguide cavities, microstrips, and CPWs are used to provide an ac magnetic field induced from the microwave signal.[64,66,93,103,106] CPWs enable FMR measurements with a broad frequency range and easily accommodate rapid and multiple measurements of unknown samples compared to waveguide cavities, and CPWs produce a stronger ac magnetic field at the sample location which is more suitable for nanowire characterization than microstrips.[106] Here, FMR is utilized as the identification signature, and an FMR identification (FMR-ID) system is optimized using the broadband FMR technique together with carefully engineered magnetic properties of the MNWs themselves. Beyond cell labeling, these MNWs could prove useful wherever small identification markers are desired.

4.2. Ferromagnetic resonance ant its potential in biolabeling

To explain FMR briefly, a swing is taken as an example, as shown in the Figure 4.1. For resonance, there is gravity given and a person is on a swing. When the swing is slightly off-center, then it swings at a certain frequency, for example, f_1. If someone pushes the person on the swing

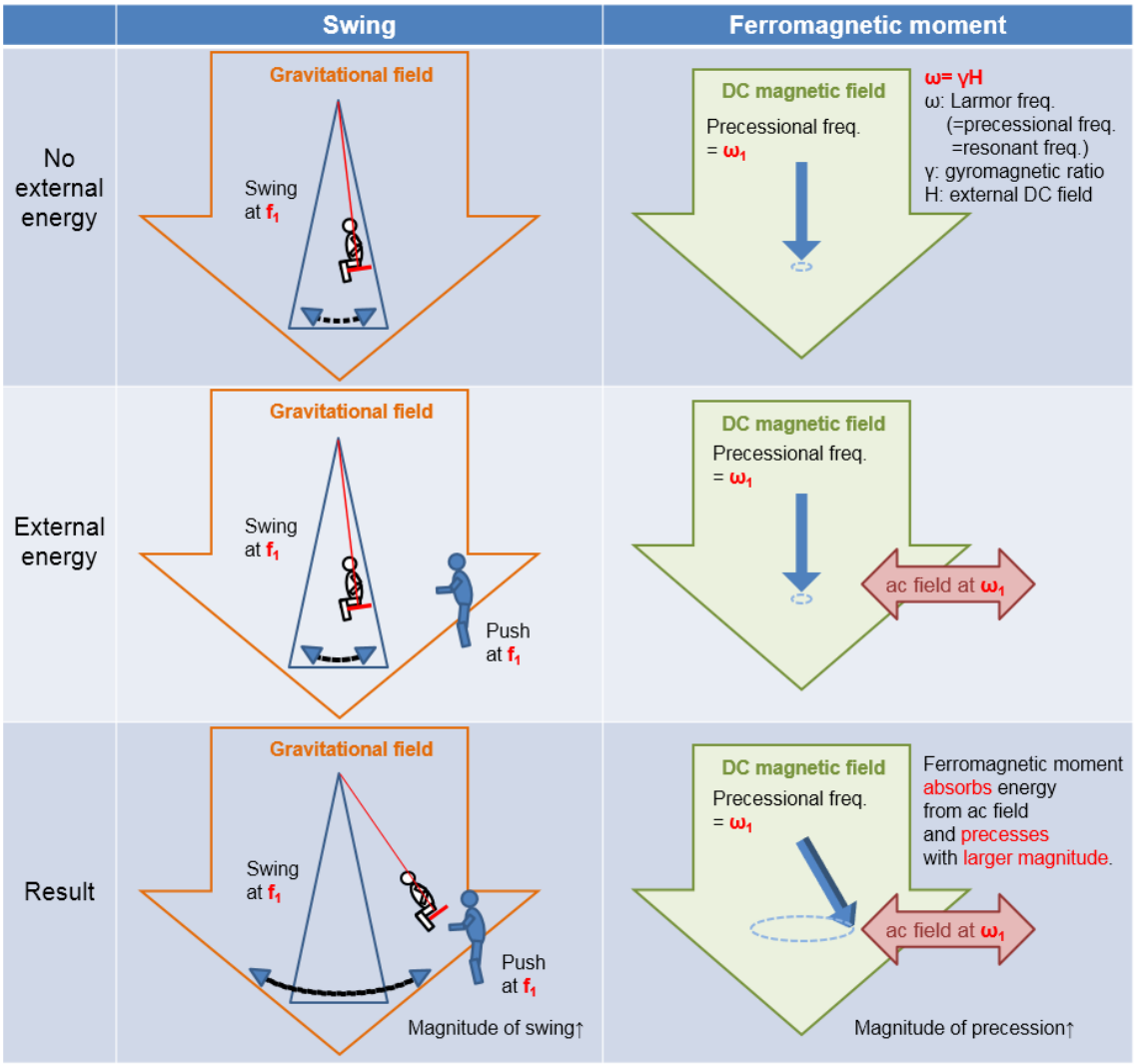

Figure 4.1. Comparison of resonance and ferromagnetic resonance.

at the same frequency of f_1, the magnitude of swing gets larger. Energy can transfer easily when the frequency of push closely matches the natural frequency of the swing.

For ferromagnetic resonance, it is similar to the resonance. There is a DC magnetic field applied (including zero field) and there is a magnetic moment of ferromagnetic material such as Fe, Ni, or Co. It is fully saturated and aligned in the DC field. At room temperature, due to the thermal energy and DC field, the magnetic moment precesses at ω_1 with small magnitude. When

ac field perpendicular to the DC field is applied to the moment, which is also at ω_1 frequency, then the magnitude of precession gets larger. Energy can transfer easily when the frequency of ac field closely matches the precessional frequency of the moment. Simply, FMR occurs when a frequency of ac magnetic field matches the precession frequency of the ferromagnetic material.

The magnetization precession frequency (= resonant or Larmor frequency) of a ferromagnetic material can be controlled by an applied DC magnetic field in accordance with the Kittel equation, which is discussed in results and discussion section.

For a spherical atom of ferromagnetic materials, the Larmor equation ($\omega = \gamma H$) as shown in Figure 4.1 is eligible. For most cases with ferromagnetic materials, the Kittel equation is valid, which considers magnetic interactions of electrons such as demagnetizing effect and exchange interaction.

Every ferromagnetic material has its own FMR behavior as a fingerprint for cell identification. Theoretically, using different proportion of ferromagnetic materials for alloys or layered structures for multilayered NWs can yield a variety of MNWs with unique signatures,[17] which is not possible by the limited number of spectrally resolvable fluorophores used currently for cell sorting and identification[6].

This nanowire labeling system using FMR can be a candidate for cell labeling in next generation or at least, it could improve the current fluorescence technique. Nine fluorophores with different colors are picked as a representative of each color for this explanation as shown in Table 4.1. If three kinds of NWs (e.g. Fe, Co, and Ni) are coated with those nine kinds of fluorophores, and these fluorophore-coated NWs are used, twenty seven kinds of cells can be labeled at the same time since the fluorescence and MNW-based FMR techniques are orthogonal and not affecting each other. Furthermore, with FORC technique, it would be more powerful biolabeling tool.

Table 4.1. Fluorophores with different colors.

Color	Dye	excitation[nm]	emission[nm]
Ultraviolet	BUV 395	348	395
Violet	BV 421	407	421
Blue	BV 480	436	478
Green	FITC	494	520
Yellow	Cy3.5	576	589
Orange	TR	595	613
Red	APC	650	660
Far red	Cy7	753	775
Near-IR	AF 790	782	805

4.3. Experimental methods

4.3.1. Nanowire fabrication

Fe, Co, and Ni nanowires were used in this work. Nanowires were made in porous anodic aluminum oxide(AAO) and track-etched polycarbonate (TEPC) by pulsed-electrodeposition using a three-electrode system at room temperature. The AAO templates (40 nm pore diameter, 12% porosity, and 50 μm thickness) and the TEPC membranes (200 nm pore diameter, 9% porosity, and 10 μm thickness) were obtained from InRedox and GE Healthcare, respectively. Prior to electrodeposition, 7 nm of titanium and 500 nm of copper were sputtered on one side of the AAO (for Fe and Co) or TEPC (for Ni) for adhesion and electric contact for electrodeposition, respectively. A thin platinum mesh was used as the counter electrode. Fe MNWs were fabricated from a solution of 0.55 mol $FeSO_4$, 0.73 mol H_3BO_3, and 5.68 mmol $C_6H_8O_6$ (pH = 3) at a pulsed-

potential of V = −1.1 V versus Ag/AgCl. Co MNWs (face-centered cubic Co for the minimum effect of the magnetocrystalline anisotropy, which is discussed in results and discussion section) were made from a solution of 0.85 mol $CoSO_4$ and 0.48 mol H_3BO_3 (pH = 2) at a pulsed-potential of V = −0.95 V versus Ag/AgCl. Ni MNWs were deposited from a solution of 0.85 mol $NiSO_4$, 0.17 mol $NiCl_2$, and 0.65 mol H_3BO_3 (pH = 2.5) at a pulsed-potential of V = −0.9 V versus Ag/AgCl. The pH of the solutions was adjusted using diluted H_2SO_4 and NaOH. The wire lengths were controlled by counting the deposited charge, which indicates the volume of material deposited in pores.

4.3.2. FMR measurements

For FMR measurements, a VNA (Anritsu 37369D) was used to apply and detect microwave signals with nonmagnetic connectors and cables to avoid interference from other magnetic materials.[64,86] The microwave signal induces an ac magnetic field. As shown in Figure 4.2(a), a 50 Ω coplanar waveguide (CPW) board was designed on 10 mil Duroid 5880LZ (ε_r = 2) with a signal line width of 16.5 mil, signal line length of 6.8 cm, gap width of 5 mil, and 2.4 mm nonmagnetic end launch connectors.[64] This CPW board was used to provide an ac magnetic field that was perpendicular to the MNW axes, Figure 4.2(b, c), while an electromagnet provided a DC magnetic field either parallel or perpendicular to the MNW axes. FMR measurements were performed using a sweeping DC field from +15 kOe to −15 kOe at constant ac frequencies from 10 to 40 GHz with 2 GHz intervals. At specific field−frequency pairs, MNWs absorbed the microwave energy due to FMR. This absorption was observed by the VNA as a reduction of the transmitted microwave signal (S_{21}, the ratio of output voltage in port 2 and input voltage in port 1). The transmitted microwave signals were normalized and analyzed.

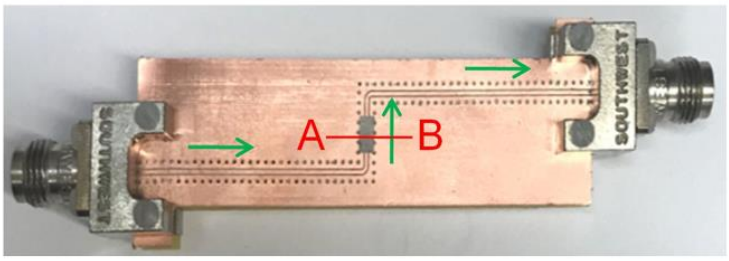

(a)

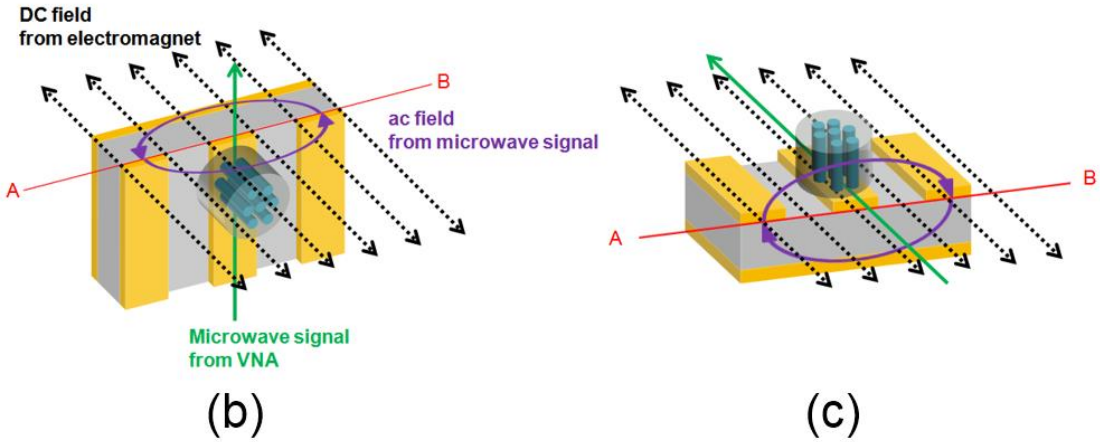

(b) (c)

Figure 4.2. (a) Photo of a CPW board with the Co MNW sample (gray rectangle). Green arrows show the direction of the microwave current and the line A-B shows the orientation of the magnetic field. (b, c) Schematic, not to scale, showing the orientations of the sample and both ac (purple ellipses) and DC (black lines) magnetic fields. The CPW board was rotated such that the DC field was (b) parallel or (c) perpendicular to the MNW axes.**

4.4. Results and discussion

4.4.1. Nanowire characterization

Iron (Fe), cobalt (Co), and nickel (Ni) MNWs were fabricated using AAO templates (for Fe and Co, 40 nm pore diameter, 12% porosity, and 50 μm thickness) and a TEPC membrane (for Ni, 200 nm pore diameter, 9% porosity, and 10 μm thickness) by pulsed electrodeposition. The length of MNWs was measured by scanning electron microscopy (SEM, JEOL 6500F). The beam was set to 25 kV with medium probe current available. For example, an SEM cross section of AAO shows that Co MNWs were grown uniformly, Figure 4.3. MNW lengths of 14, 28, and 2.3 μm were used for Fe, Co, and Ni MNWs, respectively. Figure 4.4 shows the magnetic hysteresis curves (+10 kOe to -10 kOe) of these samples, as obtained by vibrating sample magnetometry (VSM, Princeton and Lakeshore 7410) at room temperature. The saturation magnetization of Fe, Co, and Ni MNWs were 142.6 memu, 232.9 memu, and 5.2 memu, respectively. The coercivities were determined with the field applied parallel and perpendicular to the MNW long axes: 1.16 kOe and 0.1 kOe for Fe, 1.52 kOe and 0.21 kOe for Co, and 0.22 kOe and 0.14 kOe for Ni.

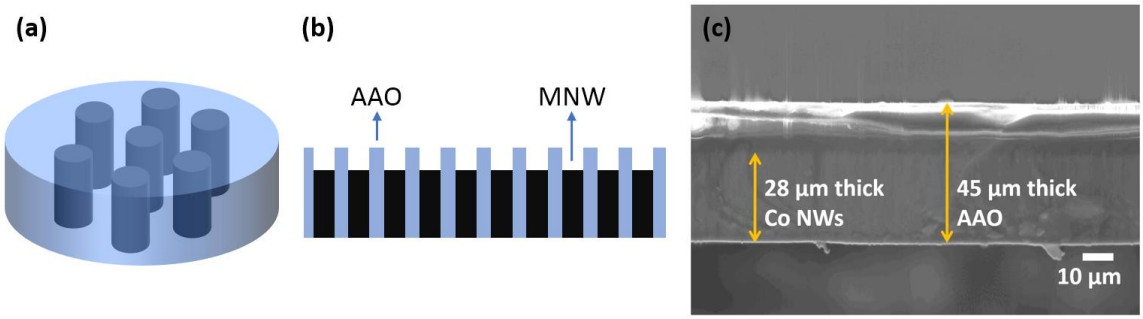

Figure 4.3. (a) Schematic and (b) cross section of AAO with MNWs. (c) SEM image of cross section of AAO with Co MNWs. Note that the bright spots are due to charging, which occurs after a darker (Debye) region above the MNWs.**

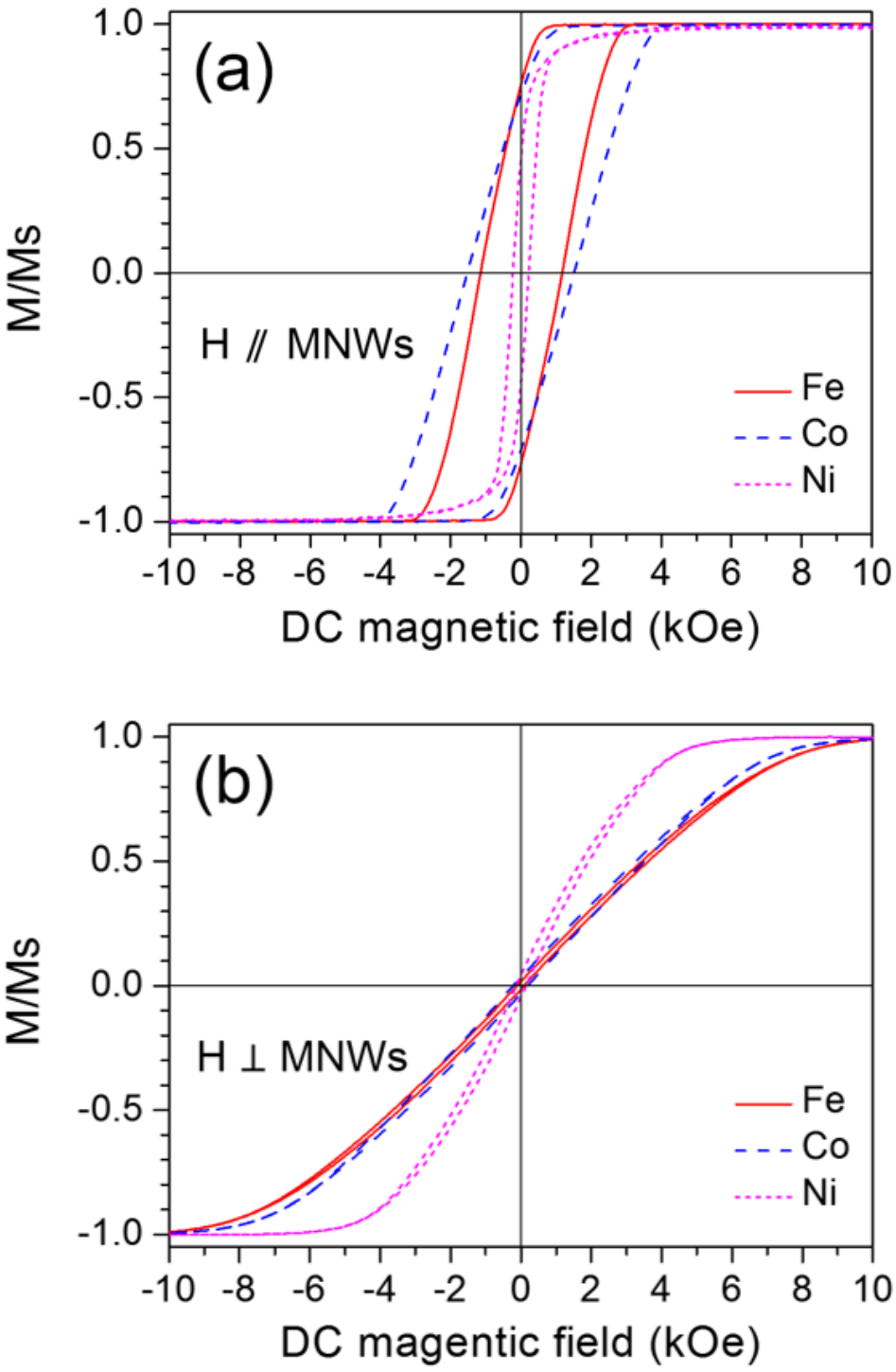

Figure 4.4. Hysteresis loops of Fe, Co, and Ni MNWs with the applied DC magnetic field (a) parallel and (b) perpendicular to the MNW axes.**

4.4.2. FMR behavior of Fe, Co, and Ni MNWs

The Kittel equation describes a precessional frequency of magnetic moments, depending on the orientation of the magnetic material and the strength of an applied DC magnetic field,[66,93,107]

$$\left(\frac{\omega}{\gamma}\right)^2 = \left[H\cos(\theta - \theta_H) + H_{eff}\cos 2\theta\right]\left[H\cos(\theta - \theta_H) + H_{eff}\cos^2\theta\right] \quad (1)$$

where ω is the angular frequency ($\omega = 2\pi f$), γ is the gyromagnetic ratio ($\gamma = \frac{g\mu_B}{\hbar}$, where g is the g-factor, μ_B is the Bohr magneton, and $\hbar$ is the reduced Planck constant), H is the applied DC field, H_{eff} is the effective field of MNWs, θ is the angle between magnetization direction and MNW axis, and θ_H is the angle between the applied DC field and MNW axis as shown in Figure 4.5(a).

Here, H_{eff} is briefly defined as the sum of shape anisotropy field, magnetocrystalline anisotropy field, magnetoelastic anisotropy field, and magnetostatic interaction field. However, due to the large aspect ratio of MNWs, the shape anisotropy is dominant and the magnetocrystalline and magnetoelastic anisotropies are negligible at room temperature.[93,94,104] Magnetostatic interactions among MNWs are dependent on the interwire distances relative to the MNW diameters,[94] which means it is proportional to a fill factor (= a porosity of templates) in our samples. Specifically, the effective field for an array of MNWs, considering shape anisotropy and magnetostatic interactions, is given by $H_{eff} = 2\pi M_s(1 - 3P)$, where M_s is the saturation magnetization and P is the porosity of the template in which MNWs are grown.[98] This can be confirmed by checking the extreme cases where $H_{eff} = 2\pi M_s$ for $P = 0$ (single nanowires) and $H_{eff} = -4\pi M_s$ for $P = 1$ (films).[93,94] The values of H_{eff} in this work are positive since our fill factors were 12% for Fe and Co MNW samples and 9% for Ni MNW sample.

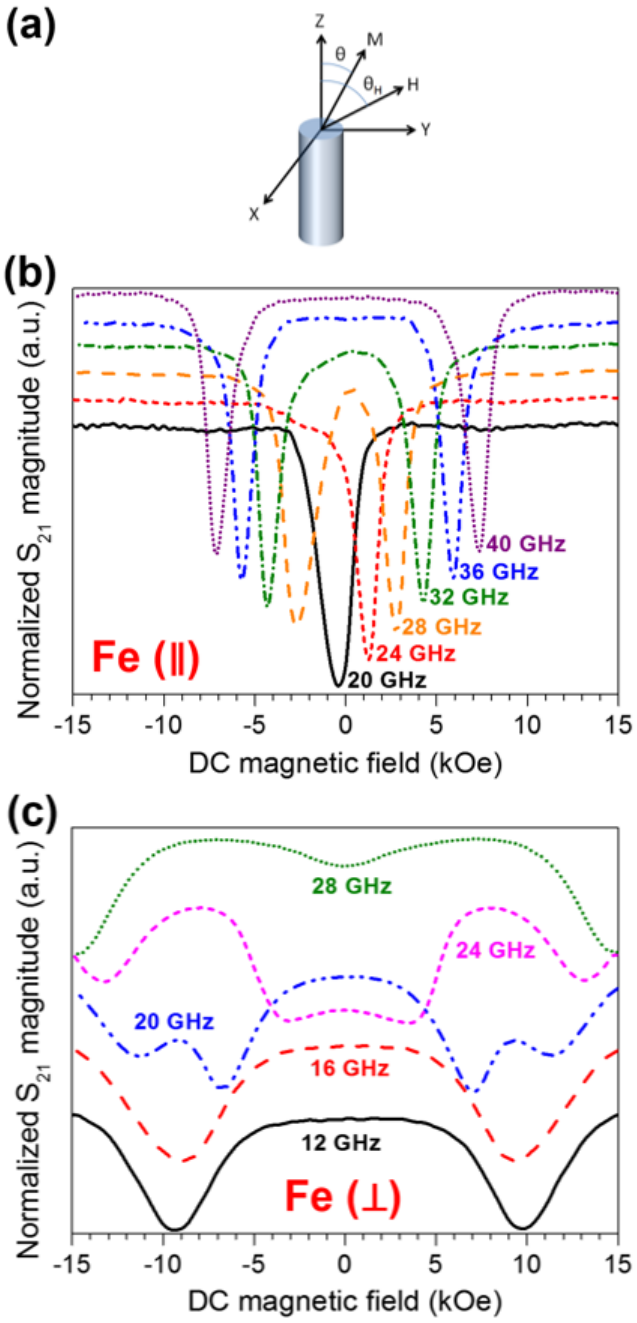

Figure 4.5. (a) Schematic defining the angles (θ) of magnetization (M) of a MNW and an applied field (H) relative to the MNW axis (Z). (b, c) Stacked normalized S_{21} (microwave signal at the output compared to the input) at labeled frequencies for Fe MNWs with the DC field (b) parallel and (c) perpendicular to the MNW axis. Representative curves are shown here for clarity, and others are given in individual FMR measurement results section.**

In the orientations shown in Figure 4.5(a), there are three cases for FMR measurements:[66]

case (1) $$\frac{\omega}{\gamma} = H + H_{eff} \quad (2)$$

(H parallel to MNW axis, $H > 0$, $\theta = 0°$, $\theta_H = 0°$)

case (2) $$\left(\frac{\omega}{\gamma}\right)^2 = H_{eff}^2 - H^2 \quad (3)$$

(H perpendicular to MNW axis, $0 < H < H_{eff}$, $0 < \theta < 90°$, $\theta_H = 90°$)

case (3) $$\left(\frac{\omega}{\gamma}\right)^2 = H(H - H_{eff}) \quad (4)$$

(H perpendicular to MNW axis, $0 < H_{eff} < H$, $\theta = 90°$, $\theta_H = 90°$)

Generally, the remanent magnetization direction of MNWs is along the MNW axis due to the shape anisotropy. If a DC field is applied perpendicular to MNWs, but it is weaker than H_{eff}, the magnetization angle remains between 0 and 90°. However, the magnetization angle changes to 90° when a perpendicular DC field is stronger than H_{eff}. Therefore, the boundary between cases 2 and 3 is the magnitude of H_{eff}. Figure 4.5(b, c) shows normalized S_{21} from FMR measurements (observation of the microwave energy absorption due to FMR as a reduction of the transmitted microwave signal, S_{21}, i.e., the ratio of output voltage in port 2 and input voltage in port 1) of Fe MNWs with parallel and perpendicular orientations, respectively.

In Figure 4.5(b), the FMR measurements of Fe MNWs with a parallel orientation shows that the resonant frequency increased as the DC field increased in accordance with case 1 (eq 2). At each frequency, the microwave signal is absorbed at two different DC fields that are almost symmetric about the origin except at 20 and 24 GHz. The signal at 20 GHz has only one absorption

null as expected by the Kittel equation. The signal at 24 GHz seems to have two absorptions: one obvious null at about 1.3 kOe and another shoulder at about −2.5 kOe. The absorption difference between these nulls can be attributed to the remanence in the ferromagnetic material since the field is being swept from positive to negative values. Once the resonant field is more negative than the coercivity (see Figure 4.4), all of the MNW samples are switched "down", so this absorption difference diminishes. This occurred for both Fe and Co MNWs.

Figure 4.6 shows the location of the FMR absorption field−frequency pairs for Fe, Co, and Ni MNWs and compares the results with the Kittel equations. The solid (case 1) and dashed (cases 2 and 3) lines are based on eqs 2−4, respectively. The solid and half-solid symbols are the experimental FMR trends from FMR measurements with parallel and perpendicular orientations, respectively. Bulk Fe, Co, and Ni have saturation moments of M_s = 1707, 1440, and 485 emu/cm^3 and g-factors = 2.08, 2.145, and 2.185, respectively.[30,108] The MNW samples made by electrodeposition have nanosized polycrystalline structures.[22,68] Also, as mentioned above, the magnetocrystalline anisotropy field is negligible for Fe and Ni because they have cubic crystal structures. However, the magnetocrystalline anisotropy of hexagonal Co is similar in magnitude to the shape anisotropy because it is uniaxial. To minimize this effect, face-centered cubic Co MNWs were made using a pH = 2 electrolyte,[25,57,96,98] which has been shown to disturb the crystallization with a high concentration of hydrogen absorbed and desorbed during deposition.[57]

The experimental FMR trends for all parallel orientations (Fe above 20 GHz, Co above 18 GHz, and Ni above 10 GHz) match well with case 1. This means that materials properties such as saturation magnetization and crystal structure (e.g., fcc Co) are accurately measured with FMR[25] and that the effective field, $H_{eff} = 2\pi M_s(1 - 3P)$ in eq 2, is valid. Therefore, these samples have the predicted magnetostatic interactions, which is also supported by the high (but not saturated) remanent magnetization from the hysteresis loops taken with the field parallel to the

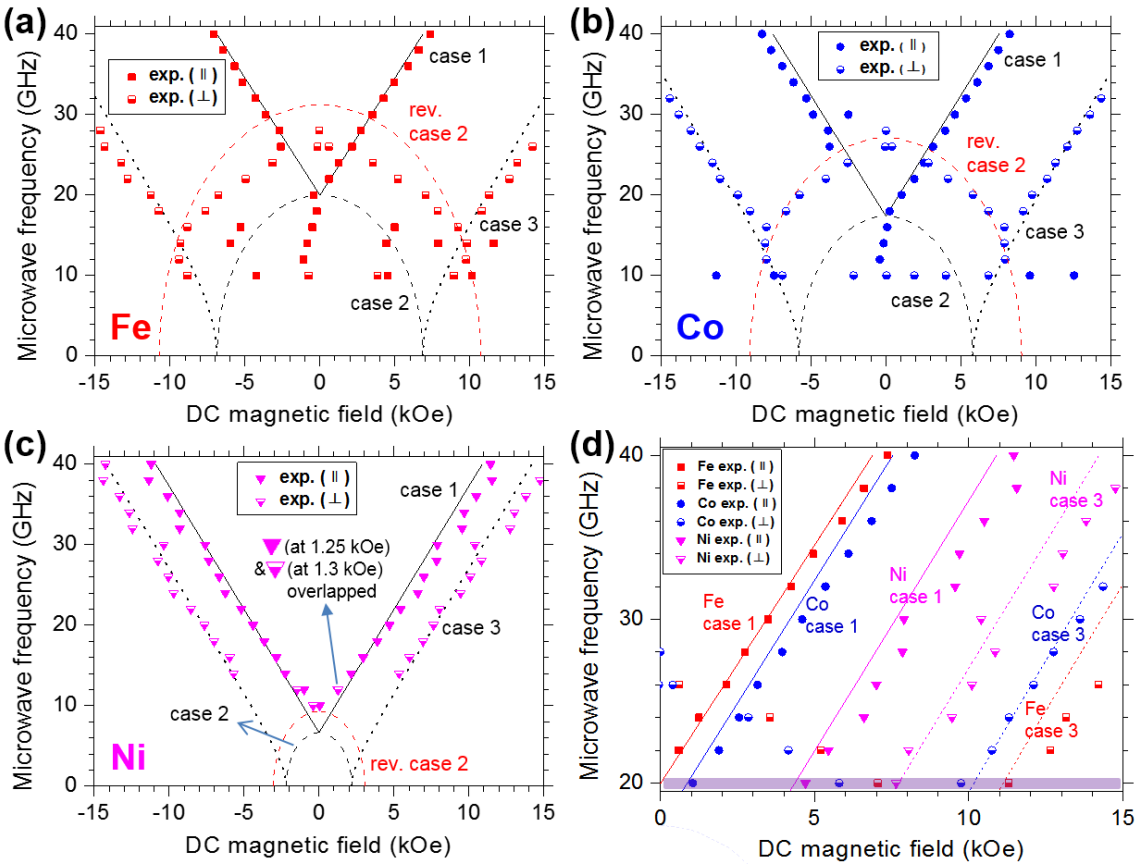

Figure 4.6. FMR trends of (a) Fe, (b) Co, and (c) Ni MNWs plotted with the Kittel equation for case 1 (black solid lines), case 2 (black dashed lines), revised case 2 (red dashed lines), and case 3 (black dotted lines). (d) FMR trends of Fe, Co, and Ni plotted together in the range of 0−15 kOe and 20−40 GHz. The purple box is for reference purpose for discussion in the text and in Figure 4.7.**

MNW axes in Figure 4.4(a). Above the parallel saturation field for each MNW sample (~3 kOe for Fe, ~4 kOe for Co, and ~2 kOe for Ni as shown in Figure 4.4(a)), the samples behave as single domains with uniform mode resonance as shown in Figure 4.6(a−c). At these fields, the magnetizations of the MNWs are fully aligned with the DC field. There is an unexpected Co FMR at −2.5 kOe (this field is close to the coercivity and below the saturation field) at 30 GHz because

the magnetic domains are not in a single-domain state. Below those frequencies (20 GHz for Fe, 18 GHz for Co, and 10 GHz for Ni), FMR is not defined by the Kittel equation.

On the other hand, the experimental FMR trends of Fe and Co with perpendicular orientation do not follow the case 2 of the Kittel equation. By definition, case 2 is below the saturation field (~9.8 kOe for Fe, ~8 kOe for Co, and ~4 kOe for Ni as shown in Figure 4.4(b)), so there is a multidomain state and the magnetostatic interactions between the MNWs are small.[93] This can be confirmed with very low remanence from the perpendicular hysteresis loops of MNWs as shown in Figure 4.4(b). This also means that the resonant frequency is sensitive to magnetostatic interactions for perpendicular orientations. So, for MNW FMR case 2, a revised $H_{eff} = 2\pi M_s$ can be used because the shape anisotropy field (also called the demagnetizing field) is dominant. When this revised H_{eff} is used in eq 3, it yields the red dashed lines in Figure 4.6(a−c). This new case 2 (red dashed lines), together with the previous case 2 (black dashed lines), provides limits for how the magnetostatic interactions affect the resonant frequency. In Figure 4.6(a, b), there appear to be more interactions between Fe MNWs than Co, for example. Case 2 for Ni is below our measurement frequencies.

The experimental FMR trend of Ni with a perpendicular orientation accords closely with case 3 Kittel equation, eq 4. The FMR trends of Fe and Co with perpendicular orientation also correspond to case 3 above perpendicular saturating applied fields at equal to or higher than 18 GHz in Figure 4.6(a, b). This shows that above the saturation field, the MNWs have the expected magnetostatic interactions based on the effective field, $H_{eff} = 2\pi M_s(1 - 3P)$ as described above.

At 10 GHz, undefined absorption nulls at −0.75 kOe for Fe and at −2.15, 0.05, and 1.9 kOe for Co are detected, in addition to FMR pairs following the original case 2 (3.85 kOe for Fe and 4 kOe for Co) and case 3 (−8.85 and 8.95 kOe for Fe and −6.9 and 6.85 kOe for Co) below

the saturation field. All these including unpredicted absorption nulls with parallel orientation below 20 GHz for Fe and 18 GHz for Co result from the unsaturated state (below the saturation field) but will be studied in the future for clarity.

Overall, the FMR trends are well fitted to the Kittel equation. Small differences between the FMR experimental and analytical results could be caused by a small angular variation of the MNW orientation inside the porous templates and/or a misalignment in the experimental setup.[93]

By comparing the FMR measurements and the Kittel equations (Figure 4.6(a−c)), it is possible to identify the specific type of MNW used for labeling. Also, it is possible to identify which MNWs and measurements are best used in an FMR-ID system.

4.4.3. Optimization of FMR measurements for the FMR-ID labeling system

For efficient labeling and identification, the fundamentals of MNW labeling and FMR-ID detection can be established using the measurement results in Figure 4a−c. Three features in particular stand out.

(1) Negative DC field sweeping is not necessary because the FMR trends are symmetric about the origin. FMR trends in positive DC fields from 0 to 15 kOe are sufficient for identification.

(2) It is best to use obvious and predictable FMR (absorption nulls that follow the Kittle equations) which occurs for all of the MNWs studied at frequency−field pairs above saturation, or $\geq$ 20 GHz.

(3) Geometric cases 1 and 3 are best for identification applications because all of the MNW materials have distinct FMR absorption nulls at each frequency.

To verify this hypotheses, three samples were measured together to test the feasibility of MNW-based identification systems. Figure 4.7 shows the normalized FMR measurements at

20−40 GHz for a combined Fe, Co, and Ni MNW sample with DC field parallel (black solid line) and perpendicular (gray solid line) to the MNW axis. The FMR absorption nulls are labeled corresponding to the FMR individual samples measured in Figure 4.6(d). Also, missing nulls based on the individual measurements are marked in a smaller font at their expected positions. When the applied field is parallel to the MNWs, the three expected absorption nulls are observed at every frequency. On the other hand, the absorption nulls are not as obvious with perpendicularly orientated DC fields. For example, at 20 GHz (corresponding to the purple box in Figure 4.6(d)), there are no absorption nulls for Fe (at ~7 kOe) and Ni (at ~7.7 kOe), Figure 4.7(a). Also, the null from Ni (at ~8 kOe) appears only as a shoulder at 22 GHz in Figure 4.7(b). Other absorption nulls with perpendicularly applied fields are so broad that they overlap and it is hard to distinguish them at ~3 kOe and ~14.5 kOe as in Figure 4.7(c, f), respectively. These broad nulls might be caused by small absorption differences and broad linewidths. (For reference, the null at ~14.6 kOe with perpendicular orientation at 34 GHz in Figure 4.7(h) is not real absorption but was from curve fitting when there was no data above 15 kOe.)

It should be noted that the null position difference between Fe and Co with the parallel applied DC field is only about 1 kOe but they are always distinguishable. However, measurements with perpendicular DC applied fields do not show all distinguishable nulls even when the null position difference is more than 1 kOe. It seems that the field linewidth of the FMR absorption with parallel DC fields is narrower than that with perpendicular DC fields. Another interesting feature is that FMR measurements with parallel DC fields only show three nulls, rather than five nulls with perpendicular DC fields from 20 to 26 GHz, as expected by Figures 4.6(d) and 4.7(a−d). The five perpendicular nulls consist of two nulls from case 2 FMR and three nulls from case 3 FMR. The case 2 FMR absorption can be located anywhere between the original and the modified

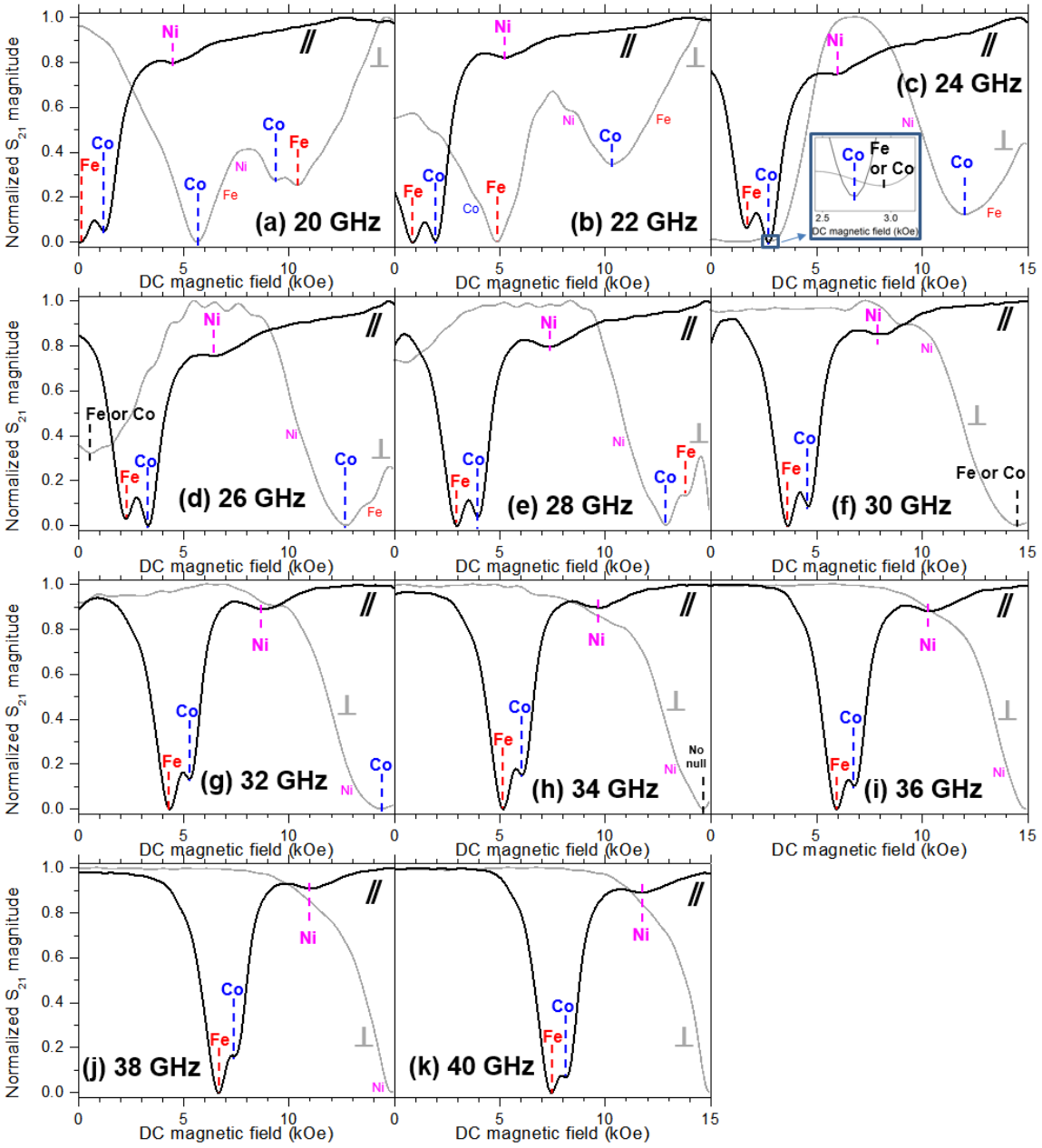

Figure 4.7. (a−k) Normalized S_{21} (microwave signal at the output compared to the input) at labeled frequencies from combined sample (Fe, Co, and Ni MNWs) measurement with the DC field parallel (black solid line) and perpendicular (gray solid line) to MNW axes.**

case 2 theoretical lines, as shown in Figure 4.6(a, b), depending on the presence of magnetostatic interactions between the MNWs. In other words, it will be hard to recognize, for example, which

FMR null belongs to Fe or Co. So, case 2 FMR is not very reliable for FMR-ID. Also, the three nulls (Fe, Co, and Ni) from the case 3 FMR in Figure 4.6(a−c) disappear as the microwave frequency increases, which would make reliable FMR-ID difficult. Higher DC fields would be necessary to get enough data with perpendicularly oriented DC fields. For the reasons above, case 1 FMR (absorption nulls and their trends) appear to be the best geometry for efficient FMR-ID detection.

A summary of these nulls from Figure 4.7 is plotted in Figure 4.8. At 22 GHz, the Fe FMR absorption was at 0.85 kOe, Co at 1.95 kOe, and Ni at 5.25 kOe. These same materials had FMR at 0.6 kOe, 1.9 kOe, and 5.45 kOe when measured individually at this frequency. Also, the Fe FMR null at 20 GHz was observed at ~0.1 kOe in this combined measurement but was absent when measured individually. Another change in the null position was found with perpendicular orientation at 28 GHz in Figure 4.7(e) as Fe FMR appeared at ~13.9 kOe but was not present in the individual measurement. The combined sample measurement showed other little shifts in the FMR absorption null locations as well. The little shifts could result from the magnetostatic interactions among samples caused by stacking. Despite these minor discrepancies, all three absorption nulls are obvious in all of the results with parallel DC applied fields from 20 to 40 GHz, as shown in Figure 4.7. In general, the FMR absorption nulls and trends from the combined and individual sample measurements are similar, as shown in Figure 4.8, and all three of the FMR-ID labels would have been correctly identified in an FMR-ID application.

Importantly, every ferromagnetic material has its own FMR behavior as a fingerprint. Theoretically, ferromagnetic alloys or multilayered structures could be incorporated into MNWs for a variety of unique signatures for FMR-ID,[17] which are comparable to spectrally resolvable fluorophores used currently for cell sorting and identification.[6] In fact, if the FMR and fluorescence techniques were used together, it could be a strong potential labeling technique.

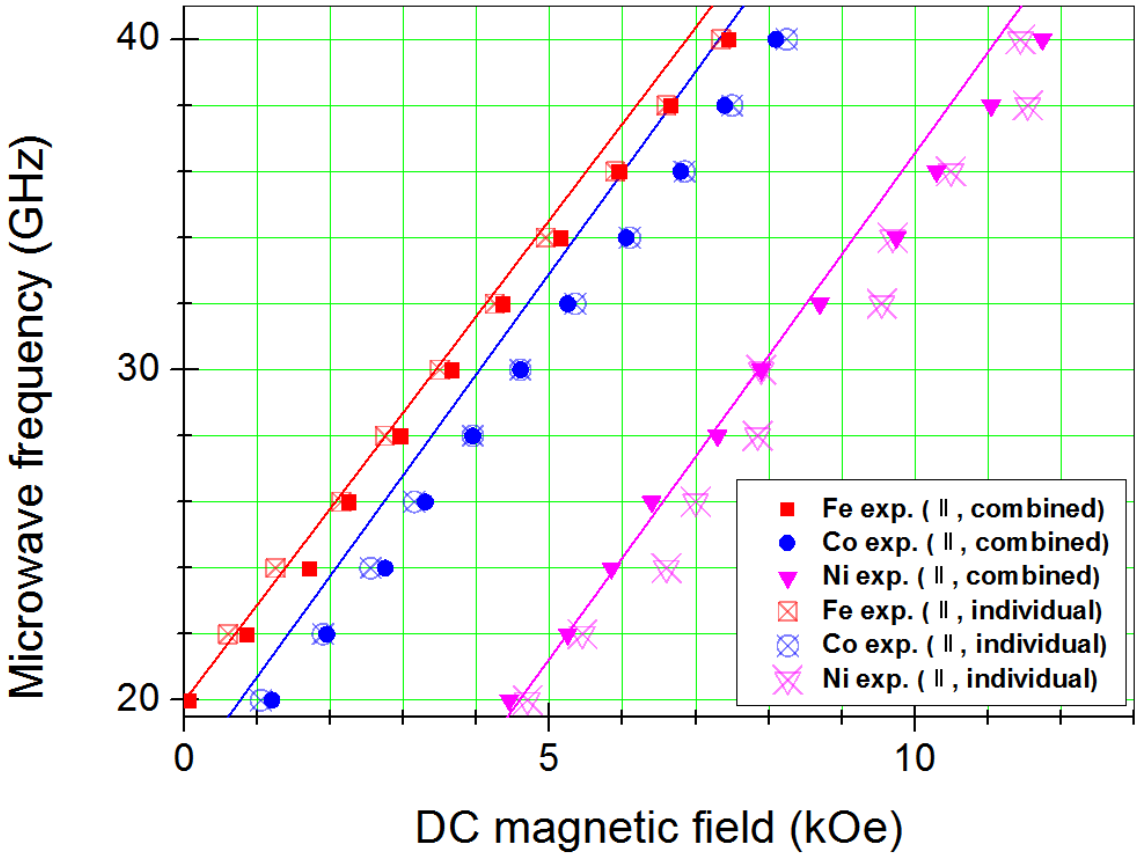

Figure 4.8. FMR trends from combined (solid symbol) and individual (empty crossed symbol) sample measurements with parallel orientation in the range of 0−13 kOe and 20−40 GHz with the case 1 Kittel equation (solid lines).**

4.4.4. Individual FMR measurement results

Results of individual FMR measurements of Fe, Co, and Ni with both parallel and perpendicular orientations are shown in Figures 4.9, 4.10, 4.11, 4.12, 4.13, and 4.14.

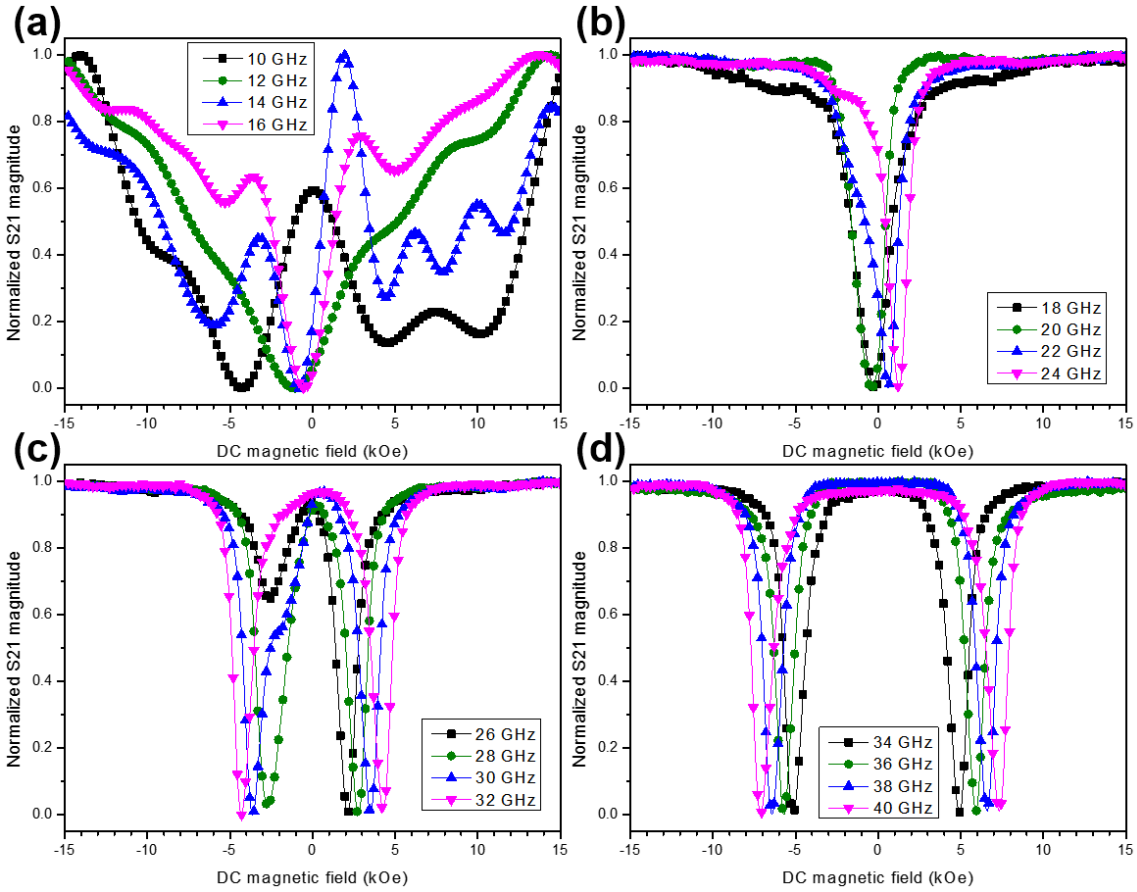

Figure 4.9. Normalized S_{21} (microwave signal at the output compared to the input) at (a) 10-16 GHz, (b) 18-24 GHz, (c) 26-32 GHz, and (d) 34-40 GHz for Fe MNWs with DC field parallel to MNW axis.**

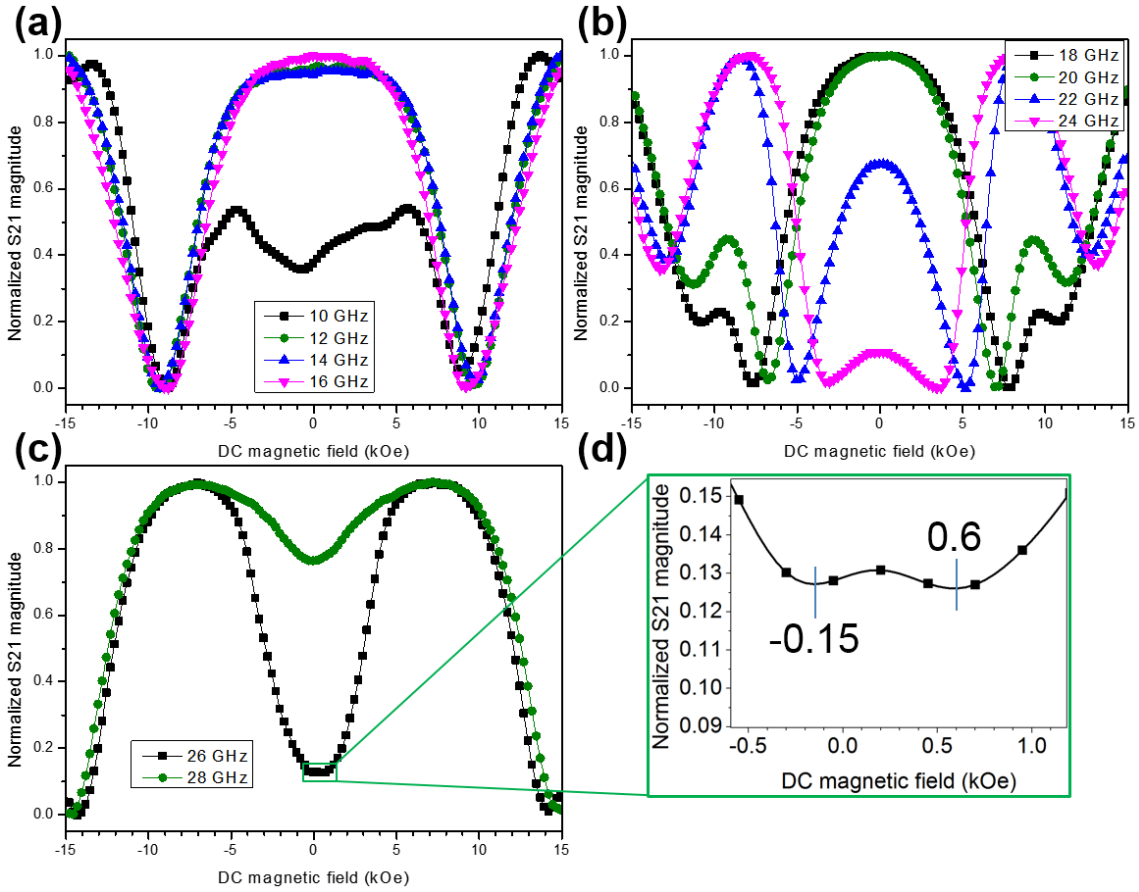

Figure 4.10. Normalized S_{21} (microwave signal at the output compared to the input) at (a) 10-16 GHz, (b) 18-24 GHz, and (c) 26-28 GHz and (d) two FMR absorption nulls of normalized S_{21} at 26 GHz for Fe MNWs with DC field perpendicular to MNW axis.**

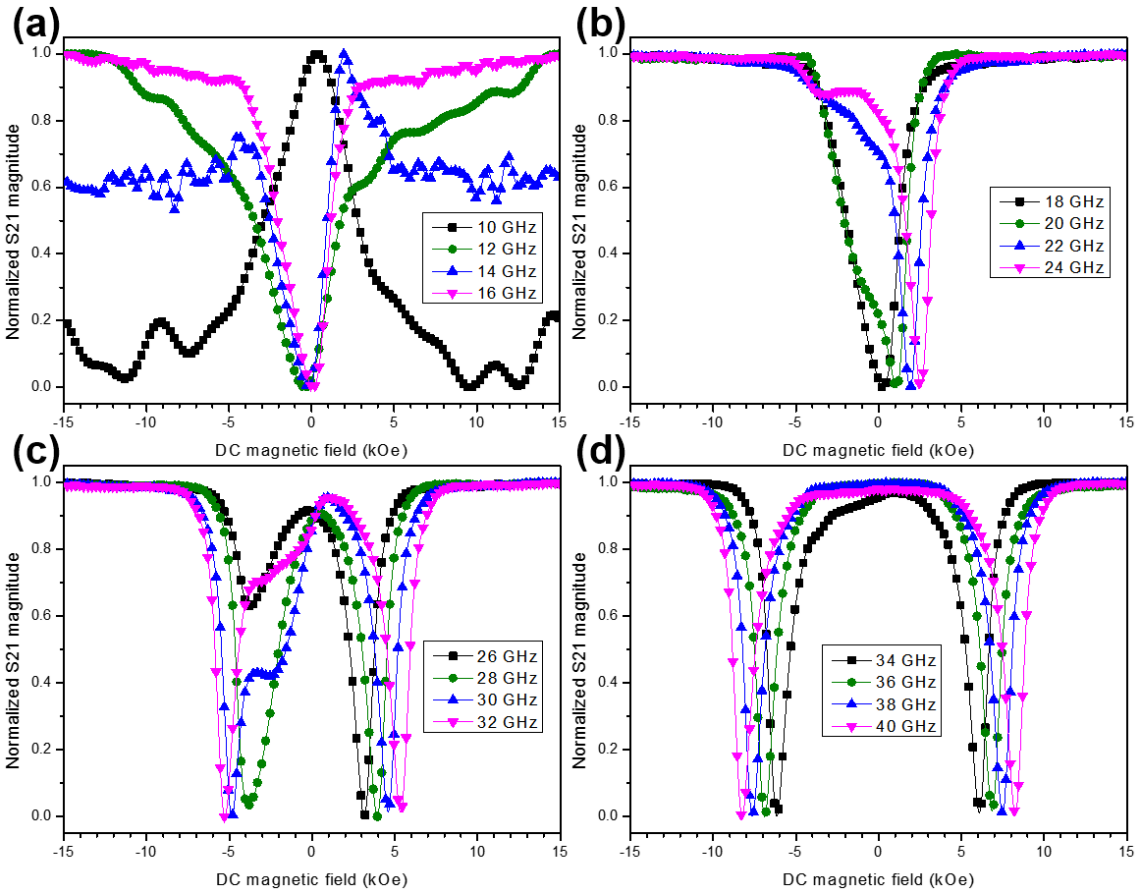

Figure 4.11. Normalized S_{21} (microwave signal at the output compared to the input) at (a) 10-16 GHz, (b) 18-24 GHz, (c) 26-32 GHz, and (d) 34-40 GHz for Co MNWs with DC field parallel to MNW axis.**

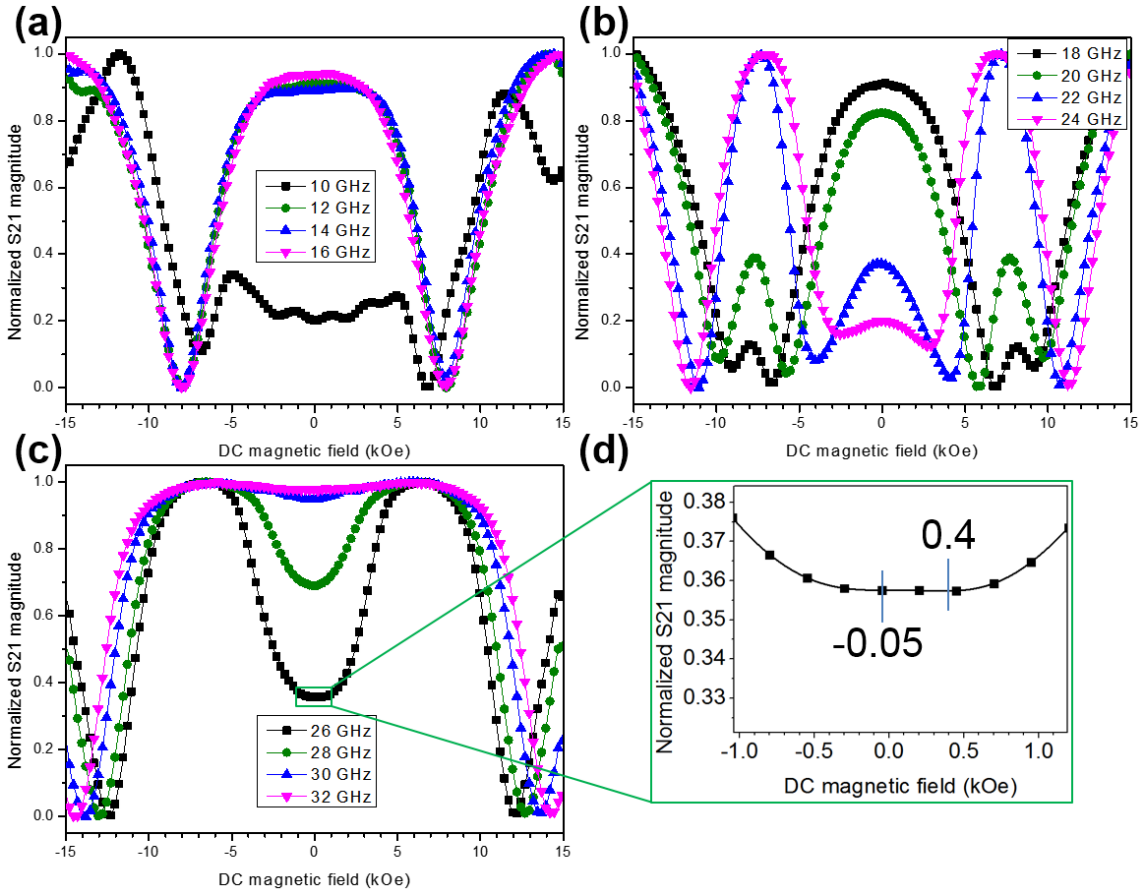

Figure 4.12. Normalized S_{21} (microwave signal at the output compared to the input) at (a) 10-16 GHz, (b) 18-24 GHz, and (c) 26-32 GHz and (d) two FMR absorption nulls of normalized S_{21} at 26 GHz for Co MNWs with DC field perpendicular to MNW axis.**

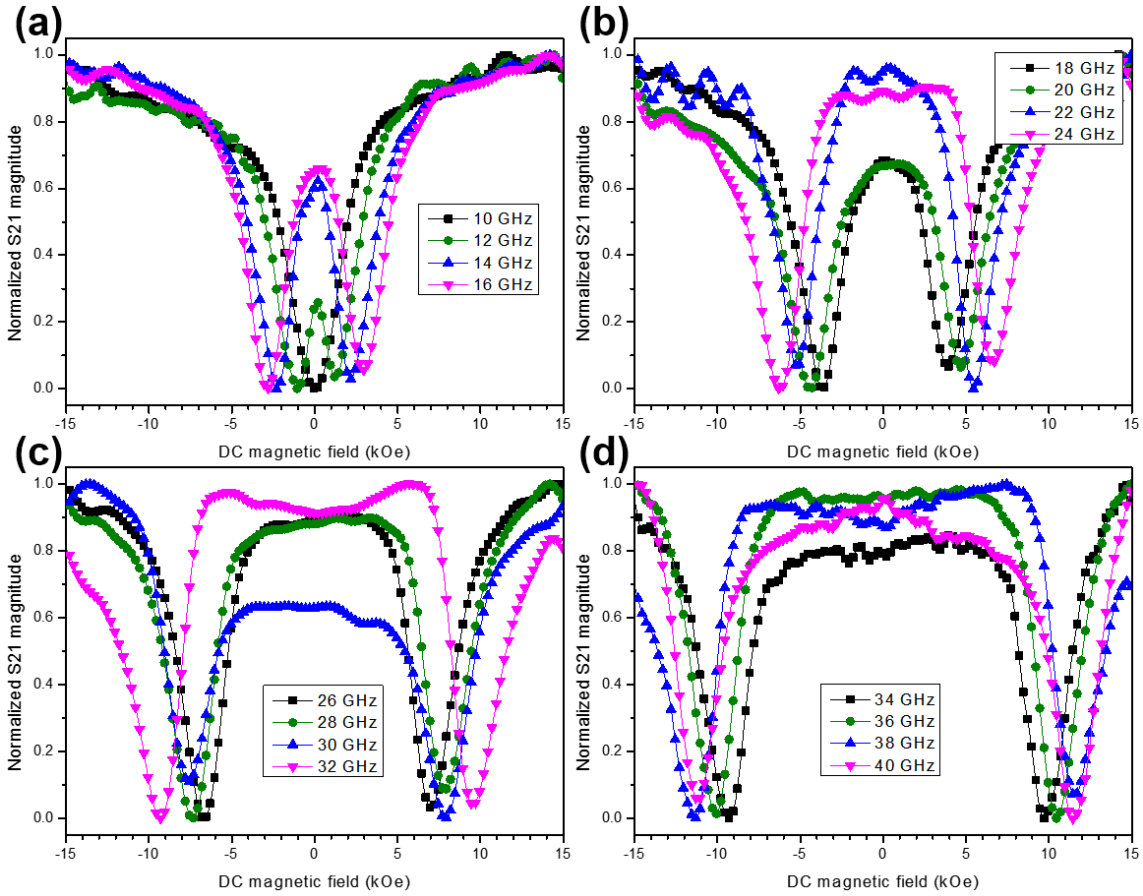

Figure 4.13. Normalized S_{21} (microwave signal at the output compared to the input) at (a) 10-16 GHz, (b) 18-24 GHz, (c) 26-32 GHz, and (d) 34-40 GHz for Ni MNWs with DC field parallel to MNW axis.**

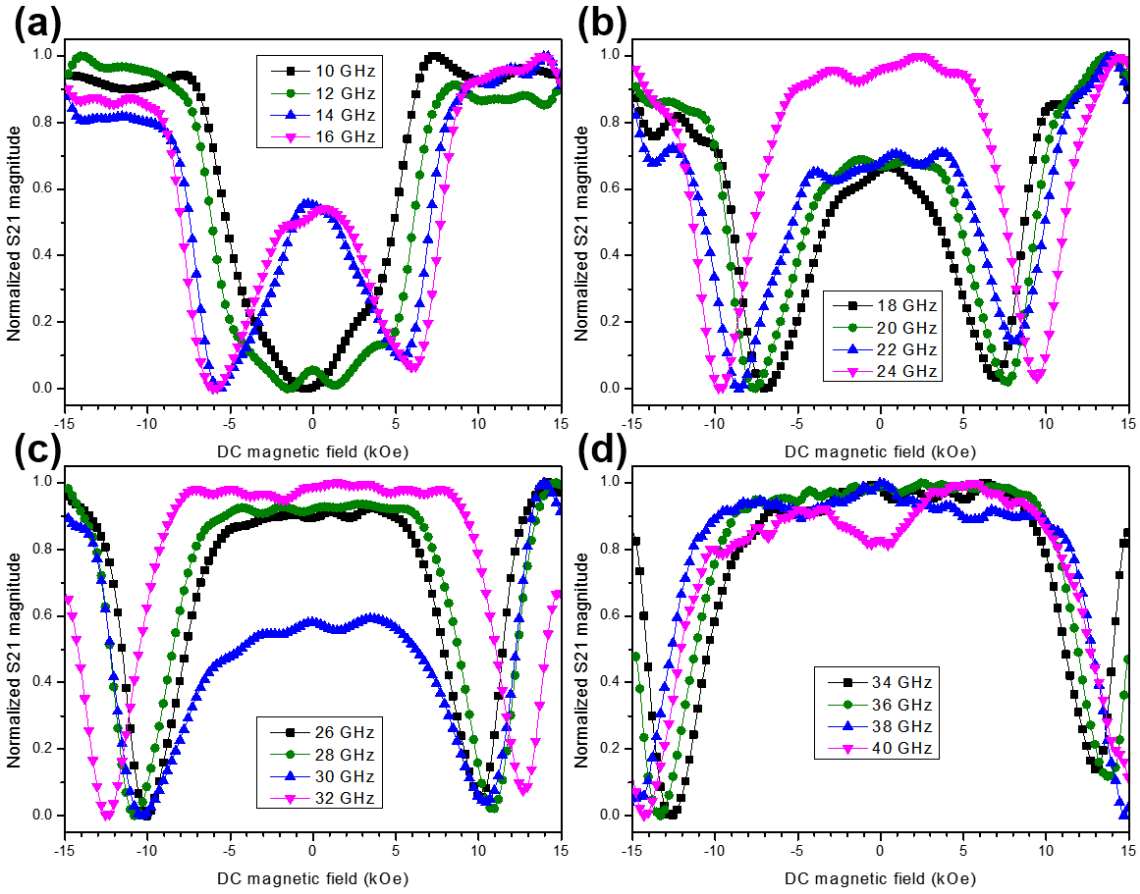

Figure 4.14. Normalized S_{21} (microwave signal at the output compared to the input) at (a) 10-16 GHz, (b) 18-24 GHz, (c) 26-32 GHz, and (d) 34-40 GHz for Ni MNWs with DC field perpendicular to MNW axis.**

4.4.5. Error analysis

4.4.5.1. Errors in S_{21}

Errors in S_{21} from ferromagnetic resonance (FMR) measurements were calculated as the standard deviation of the measured spectra from the fitted spectra, as shown in Table 4.2. The FMR spectra is normalized between 0 and 1, the calculated error is also in the same range. Error usually decreases as microwave frequency increases. For example, as shown in Figure 4.15, which shows normalized S_{21} with errors at 16, 18, 20, and 22 GHz for Fe MNWs with parallel orientation, there is a significant difference between two S_{21} at 16 and 22 GHz. It is because the absorption null at 16 GHz is not defined by the Kittel equation. FMR for Fe MNWs with parallel magnetizations is defined by a null at zero DC field for 20 GHz, followed by nulls along the Kittel equation above 20 GHz. So, the null at 16 GHz is not due to a well-behaved precessional resonance like FMR. One of the main points of this work is to identify the FMR range for Fe, Co, and Ni MNWs that will yield the most efficient FMR identification, and these errors confirm the choice of using frequencies at 20 GHz or above.

Table 4.2. Errors in S_{21} from FMR measurements.**

		Microwave frequency [GHz]							
		10	12	14	16	18	20	22	24
Error (±)	Fe ∥	0.0549	0.0775	0.1008	0.0642	0.0088	0.0056	0.0035	0.0034
	Fe ⊥	0.0393	0.0134	0.0075	0.0090	0.0058	0.0043	0.0043	0.0045
	Co ∥	0.0604	0.0605	0.0592	0.0184	0.0048	0.0032	0.0024	0.0023
	Co ⊥	0.0351	0.0126	0.0053	0.0047	0.0034	0.0030	0.0039	0.0041
	Ni ∥	0.0368	0.0308	0.0184	0.0231	0.0370	0.0354	0.0363	0.0467
	Ni ⊥	0.0299	0.0344	0.0355	0.0274	0.0437	0.0449	0.0562	0.0471

		Microwave frequency [GHz]							
		26	28	30	32	34	36	38	40
Error (±)	Fe ∥	0.0035	0.0025	0.0030	0.0033	0.0038	0.0040	0.0036	0.0032
	Fe ⊥	0.0055	0.0041	-	-	-	-	-	-
	Co ∥	0.0025	0.0021	0.0023	0.0022	0.0018	0.0020	0.0019	0.0021
	Co ⊥	0.0044	0.0039	0.0034	0.0027	-	-	-	-
	Ni ∥	0.0150	0.0250	0.0262	0.0234	0.0403	0.0224	0.0202	0.0232
	Ni ⊥	0.0170	0.0267	0.0275	0.0188	0.0468	0.0203	0.0164	0.0240

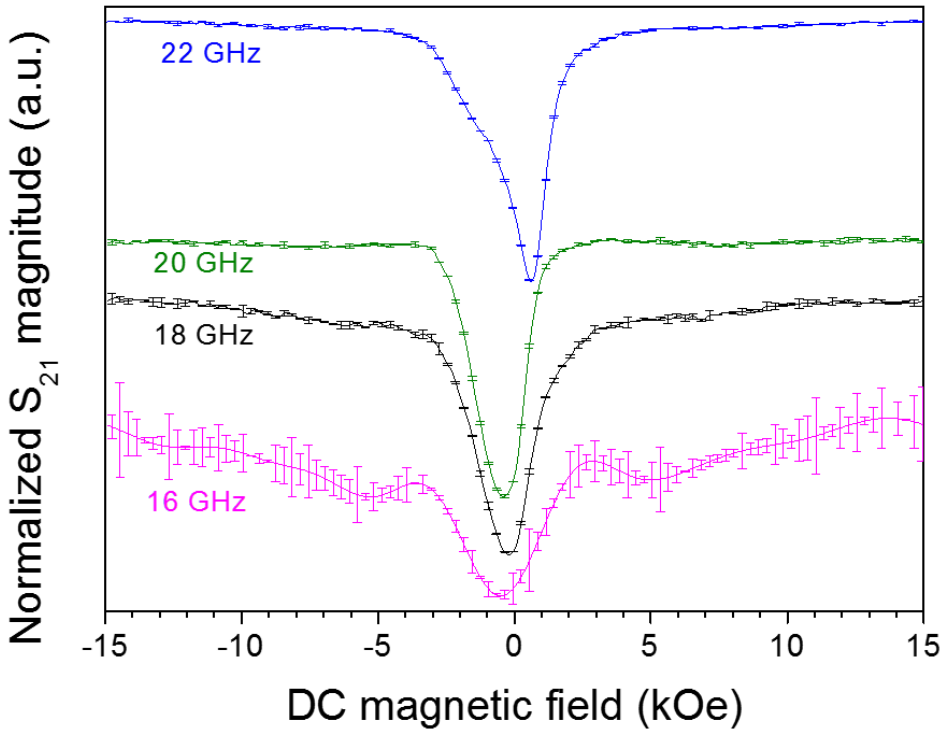

Figure 4.15. Stacked normalized S_{21} (microwave signal at the output compared to the input) with errors at 16, 18, 20, and 22 GHz for Fe MNWs with DC field parallel to MNW axis.**

4.4.5.2. Errors in g-factor

As shown in Figure 4.6, the experimental FMR trends of Fe, Co, and Ni MNWs with parallel magnetizations match the case 1 Kittel equation well with small errors due to small differences in slope. This slope difference comes from the difference in the g-factor of the gyromagnetic ratio. Table 4.3 shows the bulk g-factors from literature that was used in the Kittel equation and the experimental g-factors acquired by the line fitting of the FMR results at parallel orientation. The experimental g-factor depends on the local ordering or local magnetic fields, which are affected by the amount of defect, strain, and crystallinity inside the material. In this work, Fe, Co, and Ni MNWs grown in the confined nanopores of templates by electrodeposition

Table 4.3. g-factors used in the Kittel equation and acquired by the line fitting of the results of FMR experiments with parallel orientation.**

	g-factor	
	Kittel equation	Experiment
Fe	2.08	1.874
Co	2.145	1.986
Ni	2.185	1.848

were used for FMR measurements, and they have nanosized polycrystalline structures. It is reasonable that the experimental g-factors are slightly different from the bulk ones as found here.

4.5. Conclusions

To verify the potential of an FMR-ID labeling system, Fe, Co, and Ni MNW samples were fabricated by template-assisted pulsed electrodeposition and measured for FMR absorption individually and in combination. For FMR analysis, the Kittel equation was generally used, but in order to better understand the FMR behavior of MNW samples with a perpendicular orientation, the Kittel equation had to be revised. FMR analysis provided a good estimation of the magnetic properties in the MNW system, such as the saturation magnetization, the magnetostatic interaction field, and the shape anisotropy field. Generally, regardless of MNW sample's orientation, the MNW system was in a single-domain state above the saturation field or in a multidomain state below the saturation field. All the unexpected absorption nulls were either unsaturated or undefined. The parallel MNW-DC field orientation (case 1 FMR) with the optimized ranges of DC field (positive DC field from 0 to 15 kOe) and microwave frequency (at 20 GHz or above) was shown to yield the most efficient FMR-ID detection. Both individual and combined FMR

measurements show the potential of the MNW-based FMR-ID labeling system, which can also be applied to the current cell-labeling techniques.

Chapter 5

Fabrication of long-range ordered aluminum oxide and Fe/Au multilayered nanowires for 3-D magnetic memory

Some of the work in this chapter was done with the help of Dr. Sang-Yeob Sung, who performed the anodization of double imprinted Al foils and SEM characterization of them, and Dr. Zohreh Nemati, who performed the TEM characterization of Fe/Au nanowires. The fabrication of Ni stamps and Fe/Au nanowires, double imprinting on Al foils, backscattered electron SEM and VSM characterization, and data analysis were done by the author.

5.1. Introduction

The rapid development of data storage technology has enabled memory density in magnetic hard disk drives (HDDs) and solid-state devices to reach 1 Tbit/in^2 with the limit of 2-D arrays in sight. For example, the limit for heat-assisted magnetic recording-based HDDs is 10 Tbit/in^2.[109] A further increase in the memory density is possible with 3-D approaches,[109,110] such as Fe/Au multilayered magnetic nanowires (NWs) in which the bits are stored in Fe layers.

Compared to 3-D flash memory which experiences oxide crystal lattice damage by quantum tunneling and hot electron injection, leading to a finite lifespan, the NW-based 3-D memory (e.g., racetrack memory) does not experience a wear-out phenomenon because it uses

electron spins and magnetic moments for read and write, which give it a fundamental advantage of high reliability. To realize NW-based 3-D memory, two structural features are required, long-range ordered anodic aluminum oxide (AAO) templates and multilayered NWs. We explored these features simultaneously via custom and commercial templates.

First, porous AAO templates are frequently used as templates to grow NWs by electrochemical deposition. The pores of AAO, however, have only short-range order as naturally formed during conventional two-step anodization of aluminum (Al), usually in the range of 20 times the interpore distance.[71] It is desirable to make long-range ordered AAO so that NW devices can be grown densely at known locations and contacted easily for applications, such as HDD read sensors,[54] bit patterned media, and magnetic random-access memory (MRAM)/spin-transfer torque (STT)-MRAM.

Long-range ordered AAO is possible with imprinting methods in which stamps with hexagonally ordered arrays of nanostructures such as nanopyramids,[71] nanoconvexes,[111] and nanopillars[35,54,55,72] are pressed into Al foils or Al films, and the resulting imprints guide pore growth during subsequent anodization. These stamps were made by conventional photolithography that requires many steps and e-beam lithography that is expensive and slow for millimeter square scale area.[32] Stamps with simple line patterns, instead of hexagonally arranged dots, take far less time to fabricate since the time for patterning is proportional to the number of structures.[56] Also, inexpensive Si stamps with line patterns at nanometer scales are commercially available.

The second feature of interest is multilayered NWs. Here, we use a single electrolyte bath for Fe and Au which, compared to transferring between two different baths, lowers the risk of contamination, such as corrosion at the interface between Fe and Au layers. Also, high-density vertical memory will require many Fe layers, which would be difficult with two separate baths.

There has been research on multilayered NWs for different materials deposited with single bath,[22,46,50,52,112–118] mostly using AAO templates with pore diameters larger than 100 nm. The pore diameter of AAO decreases as the pore density (number of pores /cm^2) increases, for example, AAO with 40-, 100-, and 200-nm pore diameters have densities of about 10^{10}, 10^9, and 10^8 /cm^2, respectively. To increase the number of NWs, in other words to increase the memory density, AAO with small pore diameters should be used. Using small pore templates for growing NWs requires much attention compared to larger pores since any hydrogen gas bubbles, which can accompany electrodeposition, may be trapped in small pores, hindering the deposition.

In this work, we introduce the long-range ordered AAO made by double imprinting method with the line-patterned stamp and Fe/Au multilayered NWs using commercial AAO with 40-nm pore diameter and a single electrolyte bath, which could be useful for fabrication of 3-D magnetic memory in the near future. The line stamps, the long-range ordered AAO, and the Fe/Au NWs were characterized using scanning electron microscopy (SEM, JEOL 6500F) and transmission electron microscopy (TEM, FEI Tecnai T12). The magnetic properties of Fe/Au NWs were measured using vibrating sample magnetometry (VSM, LakeShore 7410).

5.2. Experimental methods

5.2.1. Long-range ordered AAO

In this article, Si masters were purchased from LightSmyth Technologies that were 12.5 mm × 12.5 mm in total size and had line patterns of 139-nm protruded linewidth and a period of 278 nm. These masters were cleaned with acetone, isopropyl alcohol, and deionized (DI) water. A 200-nm Ni film was evaporated onto these Si masters as a seed layer, and then more Ni was electrochemically deposited to produce a Ni stamp that contained complementary line patterns.

The electrodeposited Ni film (= Ni stamp) was delaminated from the Si master when it became thick (~ 145 ± 12 μm) due to film stress, and the original Si master can be reused to make many Ni stamps. Next, Al foils (99.999%) from Alfa Aesar were degreased in acetone for 10 min, rinsed with DI water, and soaked in 1 M NaOH for 3 min to remove the natural Al oxide. The Ni stamps were imprinted into Al foils using a hydraulic press with 1200–1500 kg/cm^2, rotated 60°, and imprinted again to make double imprinted areas from which the nanopores were grown during anodization at 160 V with 1 wt% H_3PO_4 at 0 °C, as shown in Figure 5.1. The oxide growth rate by anodization was 1.14 μm/h.

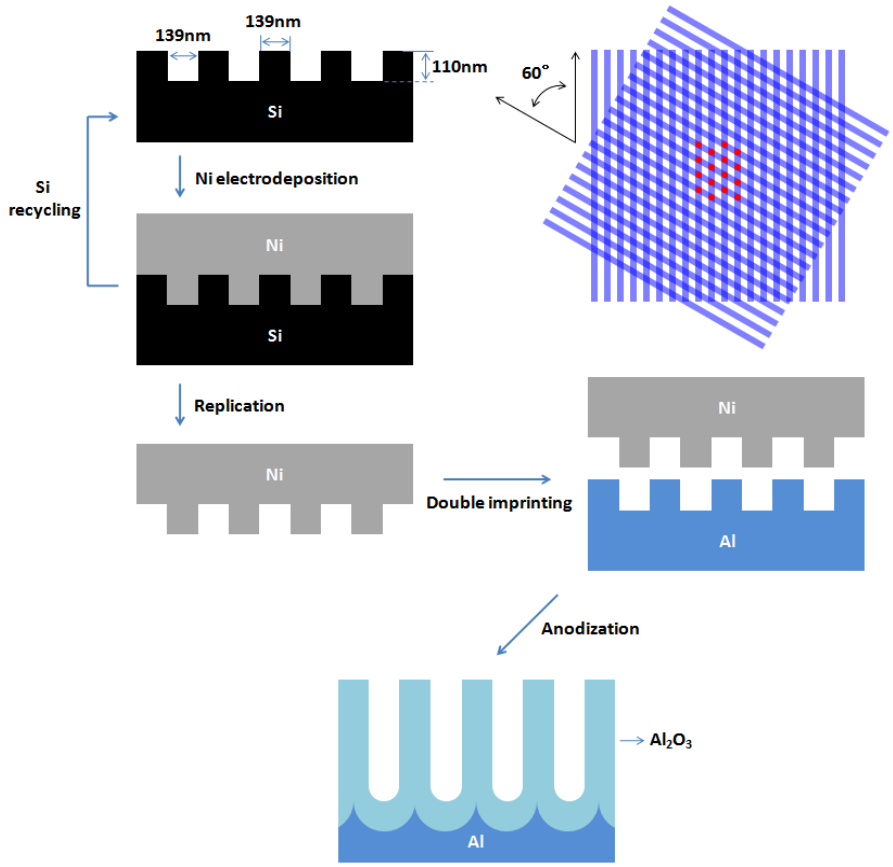

Figure 5.1. Schematic of double imprinting method.***

5.2.2. Fe/Au multilayered nanowires

Simultaneously with the synthesis of the above ordered AAO arrays, Fe/Au NWs were fabricated using commercial AAO with 40-nm pore diameter purchased from InRedox. The Fe/Au single electrolyte bath was a mixture of iron sulfate (source of Fe^{2+}), potassium dicyanoaurate (source of Au^{+}), boric acid (pH buffer), ammonium chloride (to increase the conductivity of the solution and to inhibit pH increase on a working electrode surface),[28,119] saccharin sodium (to make grains smooth and regular),[48] malonic acid (complexing agent for Fe^{3+} ions),[48] ascorbic acid (to prevent Fe^{2+} from becoming Fe^{3+} by oxidation),[48] and sodium dodecyl sulfate (to enhance the wetting and to remove hydrogen gas bubbles in pores of AAO).[48] The molar ratio of Fe and Au was 40:1. The pH of the solution was in the range of 2.5–3. Prior to electrodeposition, a 7-nm Ti film was sputtered on the one side of AAO as an adhesion layer between AAO and subsequently a 500-nm Cu film, which was an electrical contact for electrodeposition. In electrodeposition, AAO was used as a working electrode, and a platinum mesh was used as a counter electrode. The electrolyte bath was stirred vigorously at 300 rpm during electrodeposition. A 2-μm Cu seed layer was first electrodeposited in AAO using a bath consisting of copper sulfate and boric acid at −0.25 V versus a Ag/AgCl reference electrode at room temperature. After sonicating and rinsing the AAO in DI water, Fe/Au layers were electrodeposited in the AAO at room temperature with two different current pulses: the current densities below −10 mA/cm^2 and above −2 mA/cm^2 for Fe and Au, respectively.[112] The durations for both Fe and Au pulses were adjusted to control the length of both Fe and Au segments, for example, the pulse times for Fe (10 nm)/Au (6 nm) NWs were 0.7 and 3 s, respectively. A rest pulse of 1 s also was used after Fe and Au pulses in order to maintain a constant concentration of metal ions of electrolyte in AAO pores for uniform growth of NWs.[120] The whole deposition time is simply the number of bilayers multiplied by the sum of the pulse time and the rest pulse time,

e.g., deposition time for 400-bilayered Fe (10 nm)/Au (6 nm) = 400 × (Fe 0.7 s + Rest 1 s + Au 3 s + Rest 1 s) = 2280 s.

For SEM measurements, AAO with Fe/Au multilayered NWs was cleaved at the center, and a cross section of the template was coated with a 5-nm carbon film. For TEM measurements, AAO was dissolved in 1 M NaOH to free the NWs from the AAO, followed by DI water rinse.

5.3. Results and discussion

5.3.1. Long-range ordered AAO

In this section, cost-effective long-range order is achieved by two means. First, line patterns are used rather than dot patterns, and second, the e-beam pattern is used to produce not Si stamps but Si masters, from which many Ni stamps are made. Figure 5.2(a) shows the line pattern on a Ni stamp replicated by Ni electrodeposition on a Si master, and the inset shows the whole Ni stamp. The stamp looks blue since the line period demonstrated here is 278 nm, and blue light

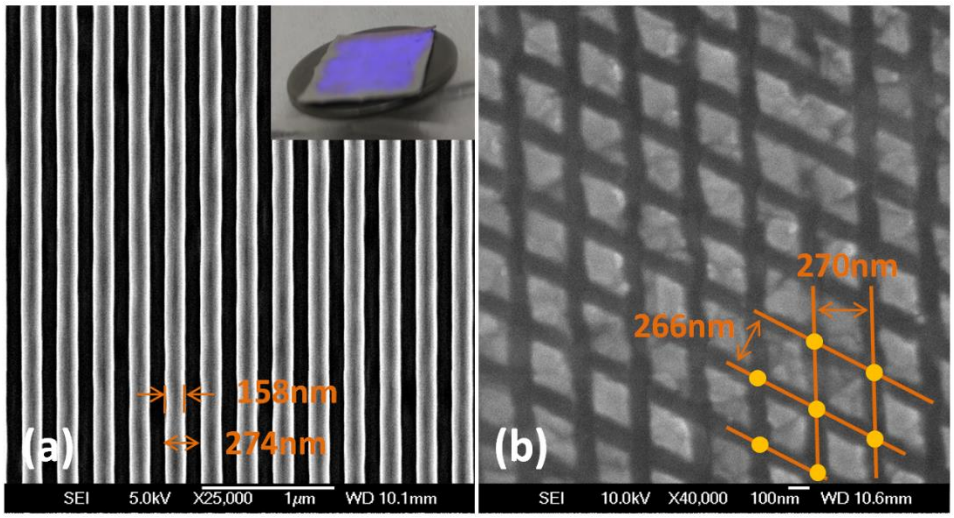

Figure 5.2. SEM images of (a) line pattern on Ni stamp with the inset showing the Ni stamp and (b) double imprinted Al precursor.***

with a wavelength of 278 nm is diffracted off the Ni stamp at 0° and 180°. The linewidth is about 160 nm, and the sidewalls of the lines are slightly sloped. This gives the Ni lines a periodic trapezoidal cross section which enables successful nanoimprinting.

When the Al precursor is double imprinted, the resulting pattern is shown in Figure 5.2(b). The double imprinted area is marked with orange dots, which are hexagonally arranged. These sunken features will guide the pore growth during anodization because they provide low energy sites for pores to start.[56] The distance between orange dots is similar to the line period of the Ni stamp and the Si master. Simply, the relationship between interpore distance (D_{int}) and line spacing is $D_{int} = \text{Line spacing} / (\sqrt{3}/2)$. For this imprinted Al precursor, the calculated interpore distance is about 300–320 nm based on the line spacing shown in Figure 5.2(b). The proper anodization voltage (V) required to match the interpore distance (D_{int}) is calculated by $D_{int} = \alpha \times V$, where α is a correlation parameter and ranges from 2 to 2.8.[16,56,71] Anodization of the imprinted Al precursor at 160 V for 1 h resulted in AAO with long-range ordered pores shown in Figure 5.3. The interpore distances were in the range of 295–315 nm, which is quite similar to the calculated values. The inset in Figure 5.3 shows AAO with a patterned region that has ordered pores (blue area with 1 cm diameter) surrounded by the not-imprinted region that has natural short-range ordered pores (gray area). The average pore diameter measured by ImageJ was 56 ± 7 nm. In addition, denser NW devices can be made if a similar process is used with smaller line period stamps and anodization voltages.

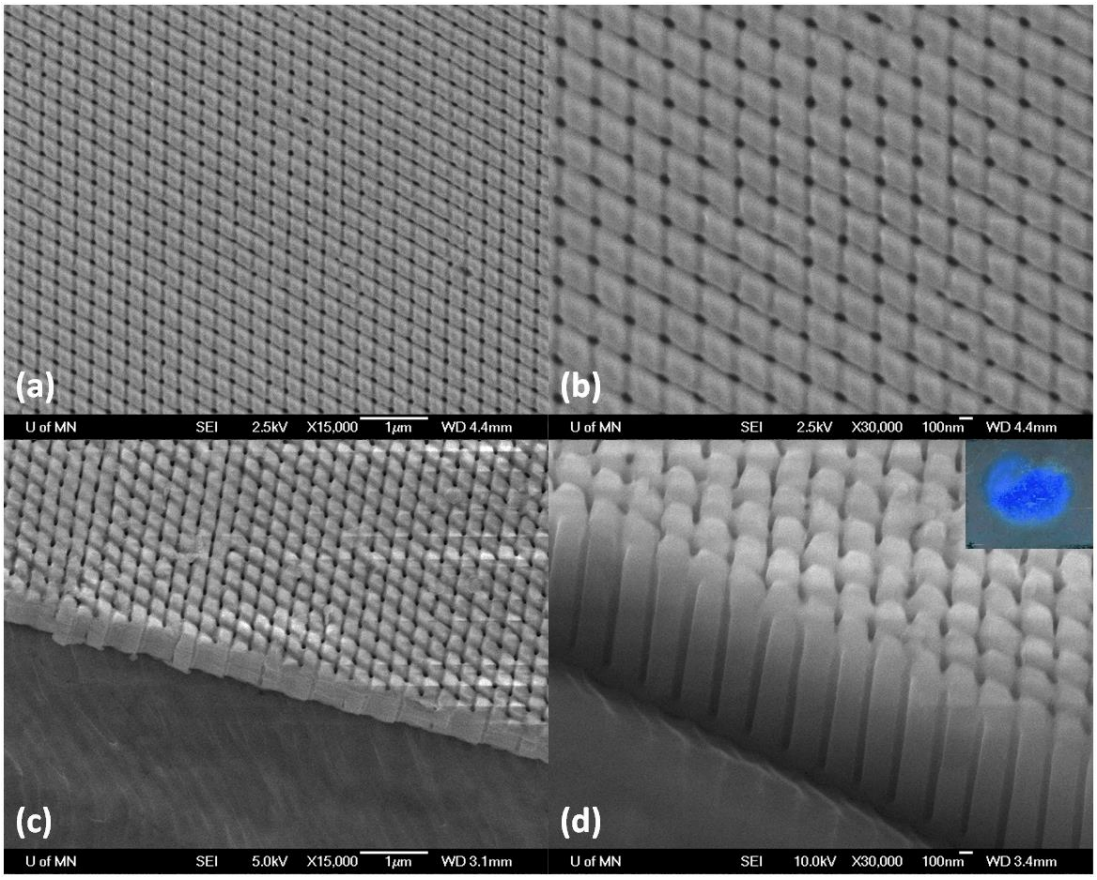

Figure 5.3. (a)–(d) AAO by anodization of double imprinted Al at different magnifications with the inset showing ordered and random regions. Inset: ordered pores diffract blue light (image courtesy of Dr. Sang-Yeob Sung).***

5.3.2. Fe/Au multilayered nanowires

As mentioned above, a 2-μm Cu seed layer was first deposited in AAO in order to block the pores to avoid electrolyte leakage, to fill dendrite structures that often form at the bottom of the AAO pores, and to provide nucleation sites for simultaneous NW growth.[22,121] Growing NWs without the Cu seed layer can cause nonuniform NW lengths, especially nonuniform segment lengths for multilayered NWs.

Constant current densities and time durations were used throughout the whole deposition process so that the deposited charges were fixed for Fe and Au segments. This galvanostatic method ensures that the lengths of both Fe and Au segments are constant along the entire length of the NWs, especially compared to potentiostatic methods,[63,67] unless the pore size of AAO has a distinctive variation or hydrogen bubbles block pores. In this way, 400 bilayers were made with high uniformity.

Segment lengths were confirmed with SEM. Typical SEM analysis usually involves either images of small areas (at most about ten NWs in one SEM image) or energy-dispersive X-ray spectroscopy to check compositions of single NWs or the surface of a filled AAO cross section. Here, we show that SEM images with backscattered electrons provide excellent contrast for segments, even well into the array (up to 2 μm depth from AAO cross section surface), as shown in Figure 5.4. TEM images of the NWs are also shown in Figure 5.5.

As shown in Figures 5.4 and 5.5, the segment lengths of all different types of Fe/Au NWs are uniform. The length of both Fe and Au segments of NWs can be simply controlled by changing the pulse duration, thereby adjusting the amount of deposited charges. Lee et al. investigated Fe and Au composition ratio depending on the current density in electrodeposition,[112] indicating that an alloy was not formed by using the current densities below −10 mA/cm^2 for Fe and above −2 mA/cm^2 for Au.

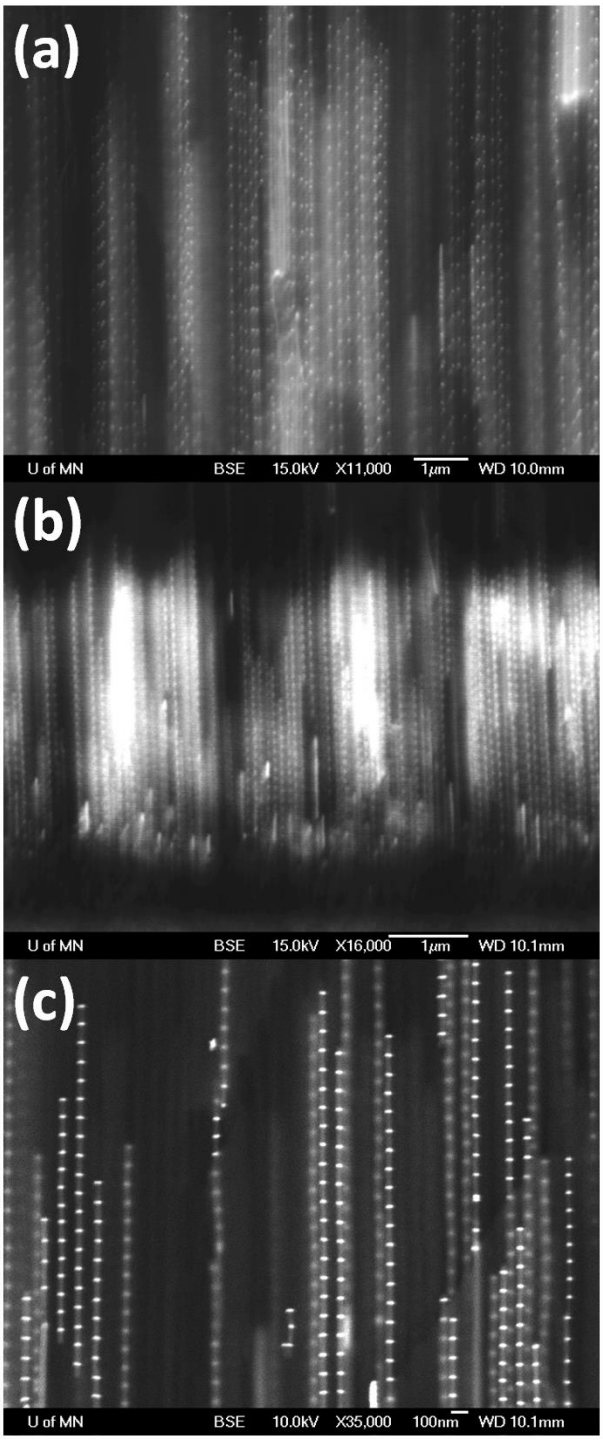

Figure 5.4. SEM backscattered electron images of AAO cross section showing Fe (gray)/Au (white) multilayered NWs in the array. (a) Fe (300 nm)/Au (50 nm) NWs. (b) Fe (50 nm)/Au (60 nm) NWs. (c) Fe (100 nm)/Au (20 nm) NWs.***

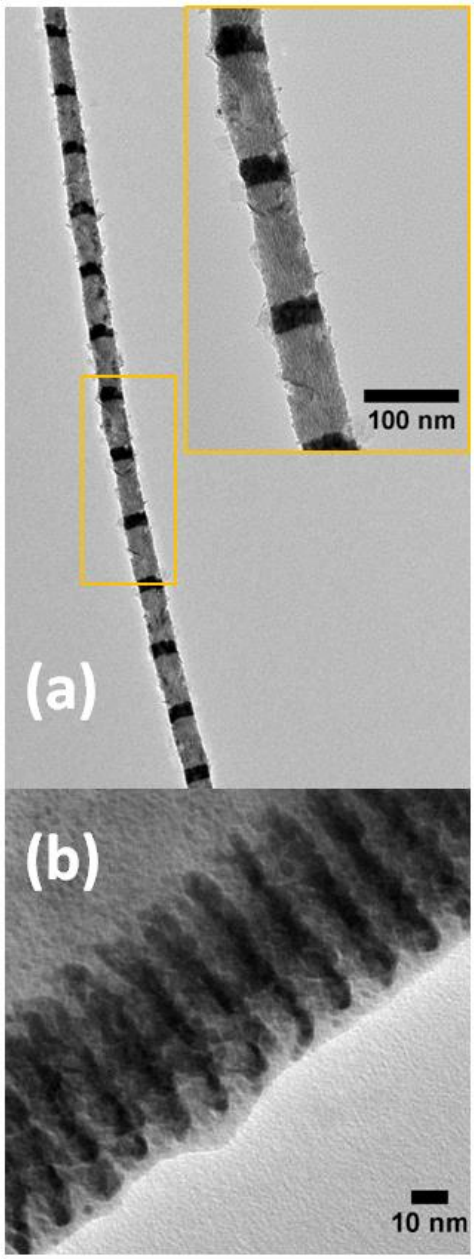

Figure 5.5. TEM images of Fe (gray)/Au (black) multilayered NWs. (a) Fe (120 nm)/Au (30 nm) NW. (b) Fe (10 nm)/Au (6 nm) NW (image courtesy of Dr. Zohreh Nemati).***

The magnetic hysteresis loops of an array of 40-nm diameter Fe (120 nm)/Au (30 nm) NWs in AAO were measured at room temperature by VSM as shown in Figure 5.6. The coercivities with the field applied parallel and perpendicular to NW long axis were measured as 137.2 and 76.3 Oe, respectively. The shape anisotropy field (H_d) of the Fe segments is clear based on the difference in switching field when the NWs were aligned parallel and perpendicular to the applied field. For isolated NWs, this shape anisotropy field should equal the switching field of NWs with perpendicular alignment (H_{sw} in Figure 5.6), and should also equal $2\pi M_s$, where M_s is saturation magnetization (e.g., M_s of Fe = 1707 emu/cm^3). However, when the NWs are in arrays in AAO, this value must be corrected by $(1-3P)$, where P is the porosity of the template (e.g., P of AAO with 40-nm pore diameter = 12 %), meaning that $H_d = H_{sw} = 2\pi M_s(1-3P)$, or 6.9 kOe.[25,64] This value agrees very well with the switching field shown in Figure 5.6, which is a clear indication that the Fe has not oxidized and is not contaminated by the electrolyte. A single

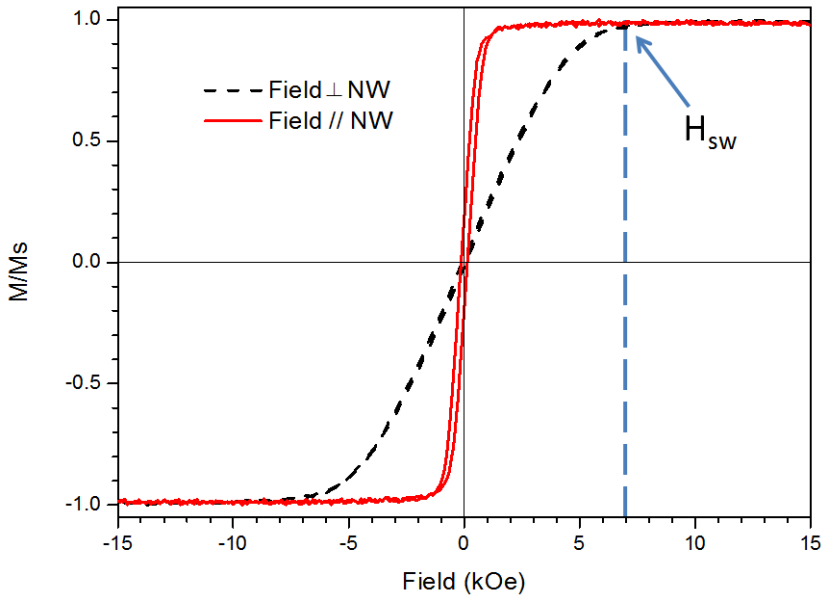

Figure 5.6. Hysteresis loops of 40-nm diameter Fe (120 nm)/Au (30 nm) NWs aligned parallel and perpendicular to the magnetic field applied.***

bath deposition ensured high-quality Fe segments. Although these NWs are inside an oxide template, aluminum is much lower on the Ellingham diagram than Fe, and therefore, Fe is unlikely to be oxidized while inside this well-insulating template, making these structures ideal for MRAM and STT-MRAM.

In the NW-based 3-D memory, nonmagnetic layers (e.g., Au) should be thick enough to hinder dipole interactions between magnetic layers (e.g., Fe) to avoid distortion in the stored data. The optimal lengths of Fe and Au segments will be studied in the future. Previously, we investigated the impact of length ratio for FeGa alloy and Cu segments with reduced dipole interactions between FeGa segments in order for FeGa/Cu multilayered NWs to have a high magnetostriction for sensors and actuators.[22,46]

In addition, Fe/Au NWs shown in Figure 5.5(b) have 400 bilayers of Fe and Au, meaning that these NWs provide 26 Tbit/in^2 if these NWs are used for memory devices since a pore density of commercial AAO with 40-nm pore diameter is 10^{10} /cm^2 (~ 6.5×10^{10} /in^2). The density would be higher if more stacks are made during electrodeposition, which is just a matter of time. Moreover, if two structural features introduced here are used together, and stamps with smaller line periods are used in double imprinting, the memory density can be even much higher.

5.4. Conclusions

The large-scale long-range ordered AAO and Fe/Au multilayered NWs presented here are interesting for many 3-D nanostructured material applications. Double imprinting could be the simplest and most cost-effective method to produce long-range ordered AAO. Many types of uniform Fe/Au multilayered NWs were fabricated simply by a Cu seed layer, galvanostatic control, and deposition time for Fe and Au layers within the single electrolyte bath. This method provides

a rapid and facile technique for multiple layers and lowers the risk of contamination. Also, through backscattered electron SEM, the uniformity of single NWs and NW arrays could be checked even up to 2 μm into the sample. These two techniques show potential for future high-density recording systems, such as 3-D magnetic memory, which require long-range ordered devices inside insulation to suppress crosstalk.

Chapter 6

Nanowire-based interconnects

6.1. Introduction

As process technology scales down, the resistivity of Cu interconnect has increased with decreasing dimensions, mainly due to electron scattering. It causes power loss and RC delays, and it gets worse with the skin effect. The skin effect is a tendency of alternating current to flow mostly near the outer surface of an electrical conductor compared to the core of the conductor. For example, in 5G networks (3.4 GHz – 66 GHz), which are just now coming into reality, a skin depth is 0.254 μm (for 66 GHz) – 1.12 μm (for 3.4 GHz).[122] This means that Cu interconnects with diameters larger than 1.12 μm cannot use a whole cross-section area for electrical conduction in 5G networks (i.e. some areas remain unused for electrical conduction). The effect becomes more and more apparent as the frequency in communication technology increases. Research and attempts to mitigate the increase in Cu resistivity have been extensively performed. But, experimental resistivities in literature are usually one or two orders of magnitude higher than that of bulk Cu because the sidewalls of the interconnects cause scattering. In this work, anodic aluminum oxide (AAO) as templates for nanowire (NW) growth was integrated on Si substrates. 20 nm diameter Cu and Ni NWs were grown inside the pores of the AAO on Si by electrochemical deposition. Then, DC resistance was measured more than 500 times for both Cu NWs with 1.7 μm length and Ni NWs with 1 μm length using nanoprobes. Next, statistical analysis was performed using Gaussian distributions and histograms of the measured data. Average resistances of Cu and

Ni NWs are 242.5 Ω and 469.2 Ω, respectively. Based on these values, the calculated average resistivities of Cu and Ni NWs are 4.5 μΩ-cm (about 2.7 times the bulk Cu, 1.68 μΩ-cm) and 14.7 μΩ-cm (about 2.1 times the bulk Ni, 6.99 μΩ-cm), respectively. These values are significantly smaller than the literature values. The diameters of both types of NWs are smaller than their experimental electron mean free paths, which means AAO is an excellent host matrix for interconnects with good insulation and smooth channel surfaces. Also, it means that NWs can be a good candidate for next-generation interconnects. Furthermore, a trend of Cu NW resistivity with diameter size is introduced based on our research group's works. Investigation on resistivity of Cu or Ni NWs with different diameters based on current work is ongoing.

6.2. Integration of AAO on Si substrates using TiW layer

AAO is nanoporous and inexpensive and has been used as a template to make various functional nanomaterials and nanodevices. In order to add more functionality to the nanomaterials and devices using semiconductor fabrication process and equipment, it is necessary to fabricate AAO on rigid substrates such as Si and to establish electrical contact at both the top and bottom of AAO.[123–125] But, the bottom of pores of AAO is electrically isolated from the substrate by a thin aluminum oxide barrier layer, which is made during anodizing process to convert Al film to porous AAO.[13,123–126]

To fabricate AAO on Si, metal layer (such as Au, Pt, or Cu) is deposited as an electrical contact and a base conducting substrate for nanomaterials or devices. Adhesion layer (such as Ti) can be used to enhance adhesion between Si and metal layer if necessary. After the metal layer deposition, Ti adhesion layer is usually deposited to increase adhesion between metal and Al layers in order to avoid AAO delamination occurred by the volume expansion during the conversion of

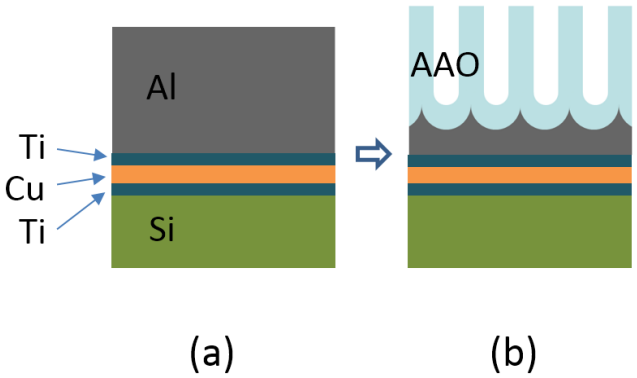

Figure 6.1. Schematic (not to scale) of film stacks on Si (a) before and (b) after Al anodization.

Al to AAO or the damaged metal layer from overanodization.[13,123] Then, Al layer is deposited and anodized to make AAO. A schematic of the structure made as mentioned above is shown in Figure 6.1. AAO has the insulating oxide barrier layer at the bottom of the pores and it should be etched to reach the underlying metal layer.

There are two current techniques to remove the barrier layer: decreasing the anodization voltage and electrochemical etching via reversed bias. However, decreasing the anodization voltage results in the dendritic pore channels near the barrier layer,[13] which are not uniformly straight vertical pores. Also, electrochemical etching via reversed bias (for inducing localized alumina dissolution to reveal the metal base) catalyzes the electrolysis of water and makes H_2 gas causing delamination of AAO from the substrate even with Ti adhesion layer.[13,124–126]

When Ti adhesion layer is used between metal layer and Al, Ti is also oxidized to TiO_2 under Al anodization conditions.[124,125] But, TiO_2 is another insulating oxide and it is hard to remove since it is chemically stable.[125] Also, when thin Ti (< 5 nm) is used as an adhesion promoter, then the whole Ti is easily converted to TiO_2 and its adhesion is lost.[124] And thick Ti (> 20 nm) usually forms a thick TiO_2 barrier layer which is hard to remove.[124] So, an intermediate Ti layer

(5-20 nm) is recommended by Holubowitch et al.[124] But, then electrochemical etching via reversed bias causing the AAO delamination is still required to remove the barrier layer.[124]

Oh and Thompson have used W (60 nm)/Ti (15 nm, as an adhesion layer between W and SiO_2) before Al deposition (Al/W/Ti/SiO_2/Si, from top to bottom), W was oxidized to WO_3 under Al anodization conditions penetrating the barrier layer of AAO, and WO_3 could be selectively removed from by a pH 7 phosphate buffer solution without pore widening which occurs by conventional chemical etching processes for AAO barrier layer removal.[125] This is a good technique if the pore size does not need to be changed after Al anodization. However, the pore of AAO is often widened purposely using chemical etching to make nanomaterials or nanodevices of different sizes. So, there is still a risk of AAO delamination from the substrate with this selective barrier removal technique using W/Ti if the pore widening is needed. It is because the W film between AAO (previously Al before anodization) and Ti is not an adhesion layer and the decreased contact area (= less adhesion) between the AAO and the W film by the chemical etching for pore widening could cause the AAO delamination.[125] Also, a 60-nm W is not thin relatively, and it cannot be solely used without an adhesion layer such as Ti. This makes devices thicker.

In order to enable removing barrier layer and widening pores of AAO on Si for various nanomaterials and devices without AAO delamination, in this work, TiW alloy ($Ti_{0.1}W_{0.9}$ or Ti 10/W 90 wt%) layer is used as an adhesion layer between Al and metal layer such as Cu. TiW is an adhesion layer, and when TiW is oxidized to TiW oxide in Al anodization, TiW oxide can be removed in aqueous solutions for electrical contact.

A schematic of the anodization and pore perforation with the structure including TiW is shown in Figure 6.2.

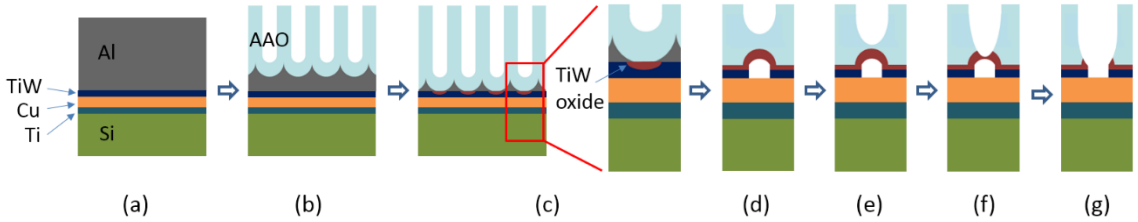

Figure 6.2. Schematic of anodization and pore perforation with structure including TiW adhesion layer. (a) structure with TiW, (b) Al anodization, (c) TiW oxide made by further anodization, (d) localized TiW oxide with inverted pore base, (e) barrier layer and (f) TiW oxide etched by over-anodization, and (g) pore widened by chemical etching.

When anodization process reaches the TiW layer, O^{2-} and OH^{-} anions in the anodizing solution are drawn through the barrier layer by the strong electric field and TiW then starts to be anodized to TiW oxide as in Figure 6.2(c).[124] TiW directly under the pore is anodized to TiW oxide, partial TiW under pore walls remains, and the barrier layer shape is changed due to the volume expansion stress of further anodization as in Figure 6.2(d).[13,124] Overanodization for 30 seconds to 2 minutes enables the anodizing solution to etch or break the barrier layer and TiW oxide in an attempt to reach the bottom metal layer as shown in Figure 6.2(e, f).[125,127] At this stage, the anodization current increases because most pores start to open together by overanodization and conductive area (=Cu layer) is increased rapidly. Further overanodization increases the current very rapidly and decreases after some time, resulting in damaged metal layer or dissolution of metal layer.[13,127] For example, the damaged Cu layer and delaminated AAO caused by overanodization are shown in Figure 6.3. So, the anodization should be stopped at the early stage of the current increased.

In order to complete pore perforation and widen the pores as needed as in Figure 6.2(g), the conventional chemical etching (e.g., 5 wt% H_3PO_4) is used since TiW oxide can be etched in aqueous solutions.

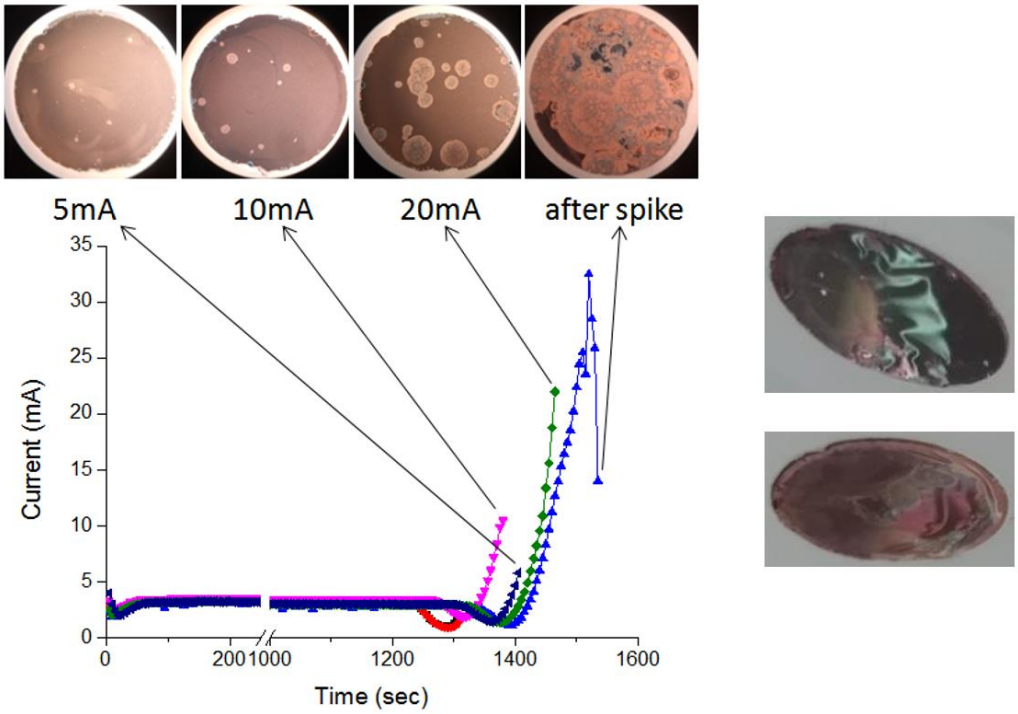

Figure 6.3. Optical microscopy images (top view) of samples (0.8 cm^2 area) with different anodization stop currents (left top). Plot of current change versus time for the different samples (left bottom). Photographs of delaminated AAOs (right).

Cu NWs grown in AAO integrated on Si using TiW layer is shown in Figure 6.4. Cu NWs cannot be grown with the barrier layer at the bottom of AAO.

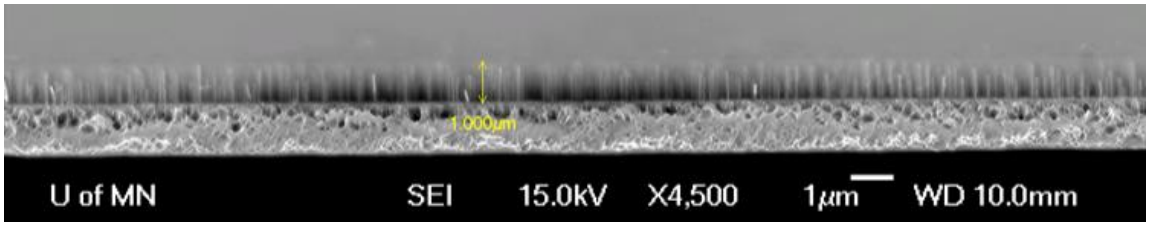

Figure 6.4. Cross-section SEM image of 1-µm AAO integrated on Si using TiW adhesion layer with electrodeposited Cu NWs (seen as white rods through AAO due to high acceleration voltage of 15 kV).

Using TiW adhesion layer allows us to integrate AAO on substrates, to remove barrier layer for electrical contact, and to widen pores of the AAO for various nanomaterials and devices without issues caused by using Ti and reverse bias-based etching (e.g., unremovable barrier layer or AAO delamination).

6.3. Experimental methods

6.3.1. Development of integrated AAO with nanowires

Table 6.1 shows an overview of whole process to make AAO on Si with NWs. Before deposition, Si wafer cleanliness is checked and Ti 40nm as an adhesion layer, Cu 850 nm as an electrical contact for anodization and electrodeposition and a base conducting substrate for NWs, and TiW as an adhesion layer and an anodization stop layer are deposited on Si by evaporation or sputtering. Then, Al 850 nm as a layer to be anodized is deposited on TiW layer on Si by evaporation. Si with films is cleaved into small pieces. Small piece is wrapped with an insulation tape except an area for anodization. Oxide growth rate by anodization at 40 V is about 80 nm/min, which means that anodization of Al 850 nm at 40 V would take 637.5 seconds. Additional 30 seconds to 2 minutes can be also considered for overanodization to thin or perforate barrier layer at the bottom of pores. During anodization, Al 850 nm becomes AAO 1 μm by volume expansion factor of 1.18-1.19.[13] It is note that one-step anodization is used for this work and AAO has a good ordered pores as shown in Figure 6.5. AAO by one-step anodization actually has better ordered pores as in Figure 6.5(b) than it seems as in Figure 6.5(a), which are pores at top surface of AAO. After anodization, pores are widened by submerging sample in 5 wt% H_3PO_4 to remove barrier layer and adjust pore size. A relationship between pore diameter and pore-widening time is $Pore\ diameter = 14\ nm + 0.38\ nm/min \times time$ since the pore size of as-anodized AAO is 14

Table 6.1. Overview of development of integrated AAO with NWs.

Step	Condition	Purpose
1. Deposit films on Si wafer	Si/Ti 40 nm/Cu 1 µm/ TiW 20 nm/Al 850 nm	Ti, TiW: adhesion Cu: electrical contact Al: layer to be anodized
2. Cleave Si wafer	Larger than 1.2 cm X 2.5 cm	Make reasonable sample size
3. Insulate sample	1 cm circular hole on insulation tape for anodization	Insulate sample except anodization area
4. Anodize Al	0.3 M $C_2H_2O_4$, 17 ˚C, 40 V, 637.5 sec (+ 30 sec - 2 min overanodization)	Produce oxide with ordered-pores
5. Widen pores	5 wt% H_3PO_4, 20 ˚C, Pore diameter = 14 nm + 0.38 nm/min X time	Remove barrier layer and adjust pore size
6. Rinse pores	Sonicate sample with DI water, 5 min	Remove residue in pores
7. Electrodeposit nanowires	Cu: 0.2 M $CuSO_4$, 0.2 M H_3BO_3, (pH 3, room temp) Ni: 0.85 M $NiSO_4$, 0.17 M $NiCl_2$, 0.65 M H_3BO_3 (pH 2.5, room temp)	Make vertical interconnects

nm in diameter. For example, pore widening for 16 min would yield about 20 nm diameter. Residue made of dissolved AAO with H_3PO_4 can remain in and block pores, hindering NW growth in electrodeposition as shown in Figure 6.6. So, sample should be sonicated in DI water for at least 5 minutes to remove the residue. Finally, NWs are made by filling pores in electrodeposition. The whole process is shown in Figure 6.7. After NW growth, if there are mushrooms made of NWs, they can be removed using Kimtech tissue for DC resistance measurement.

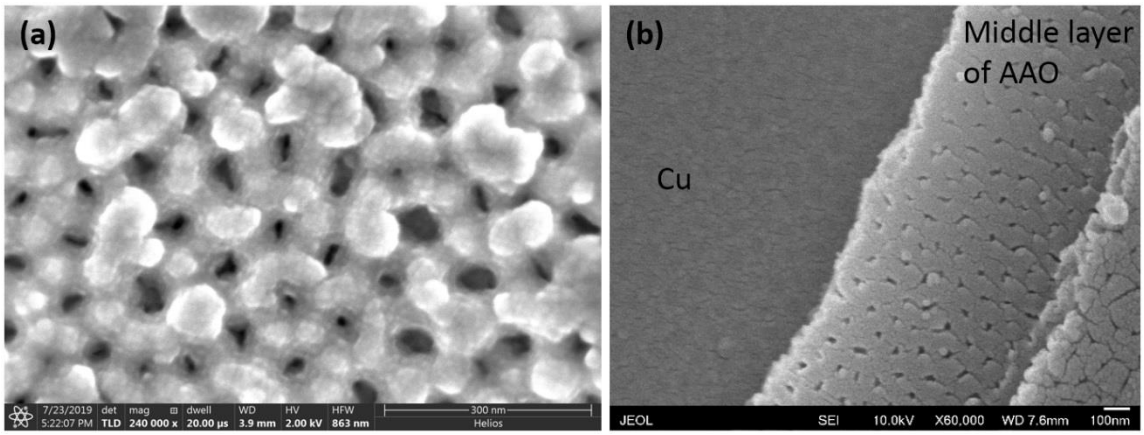

Figure 6.5. SEM images of (a) AAO surface and (b) middle layer of AAO (right image courtesy of Yali Zhang).

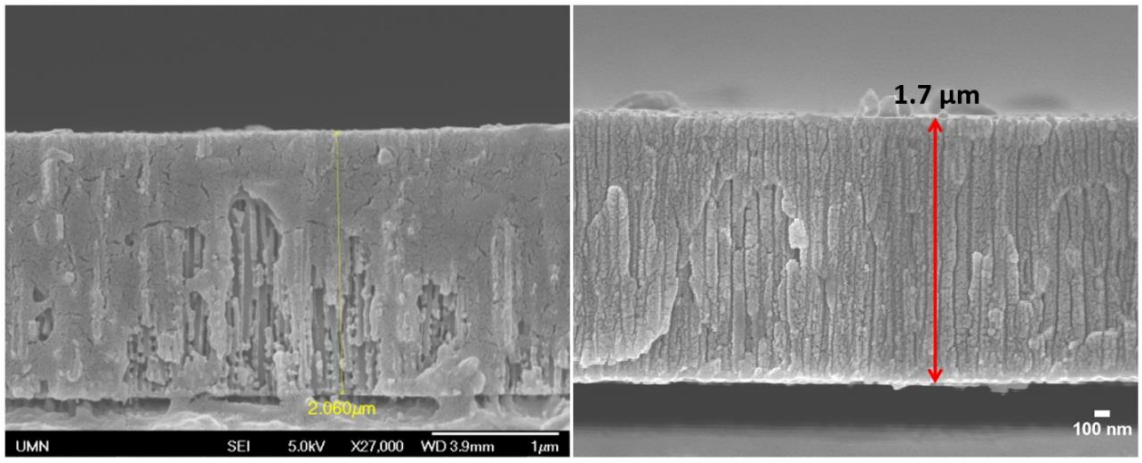

Figure 6.6. Cross-section SEM images of AAO with (right) and without (left) sonication with DI water after pore-widening step.

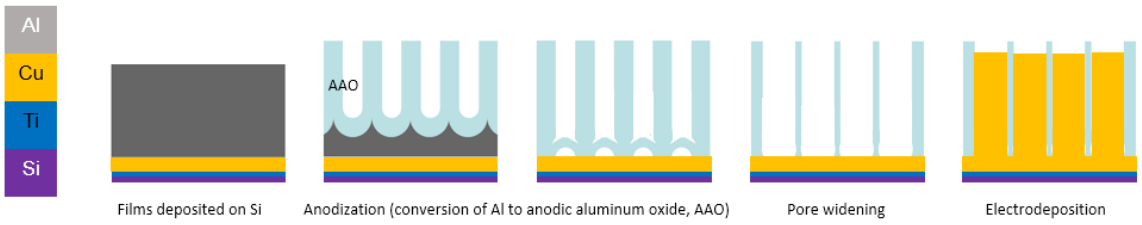

Figure 6.7. Schematic of development of integrated AAO with NWs.

6.3.2. Characterization of Cu nanowires grown in AAO on Si

After NW growth by electrodeposition, sample's cross-section can be characterized using SEM backscattered electrons (BSEs) without surface coating as shown in Figure 6.8. SEM BSE can show NW array up to 1–2 μm depth from AAO cross-section surface. Focus was on embedded NW array, so other things were out of focus. NWs seen as white rods were fairly uniform in distribution in AAO even under regions that don't have mushrooms.

6.3.3. Nanowire DC resistance measurement

Resistance of NWs can be measured using a system consisting of an Ag_2Ga nanoprobe (NaugaNeedle), a micropositioner (Newport), and a source measure unit (Keithley 2400) as shown in Figure 6.9. A four-wire sensing technique is used to eliminate the lead and contact resistance from the measurement.

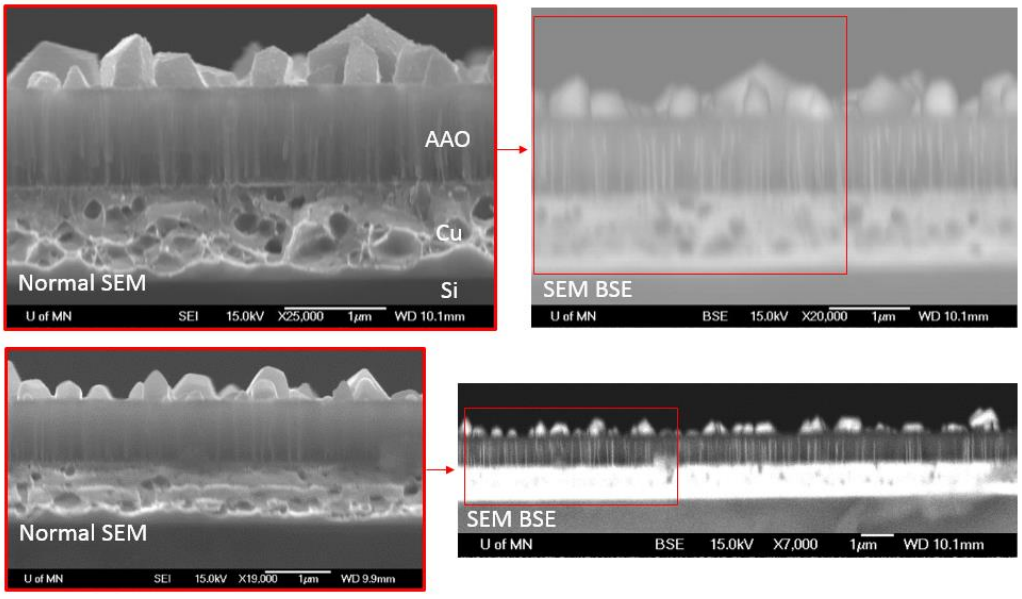

Figure 6.8. Cross-section SEM and SEM BSE images of AAO on Si with Cu NWs seen as white rods through AAO.

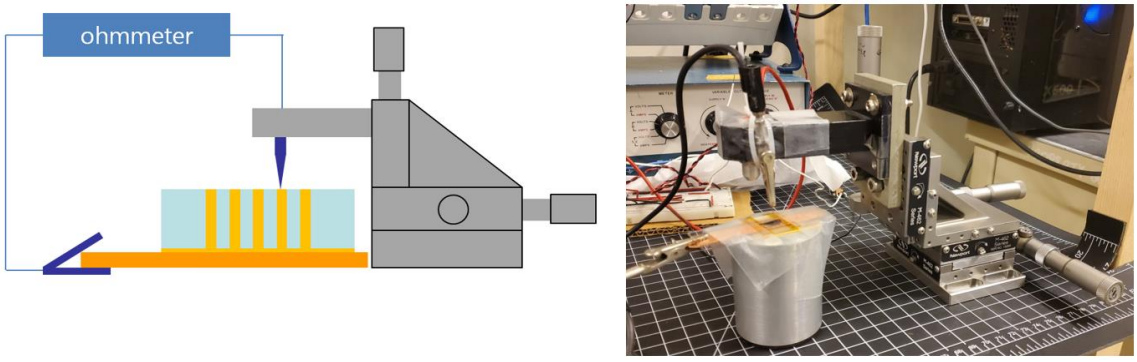

Figure 6.9. Schematic and photograph of NW DC resistance measurement.

With the nanoprobe, it is possible to land it on single NWs for DC resistance measurements as labeled with a red circle in Figure 6.10. Tip diameter of the nanoprobe is 25–100 nm. Cu layer under AAO is used as an electrode to anodize the Al, to electrodeposit NWs into the resulting AAO, and here, to probe the resistivity.

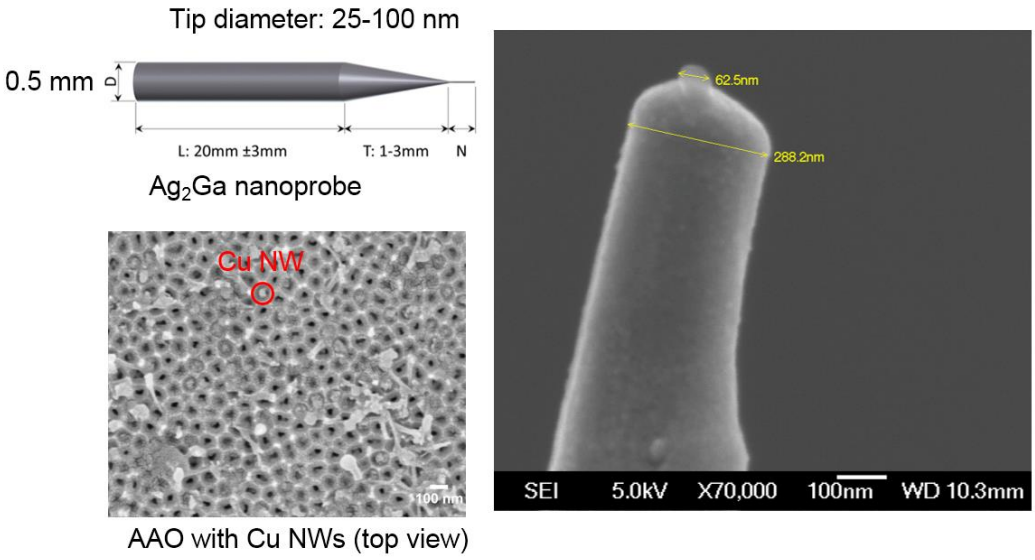

Figure 6.10. Schematic (left top) and SEM image (right) of nanoprobe and SEM image of AAO with Cu NWs with red circle for nanoprobe contact for DC resistance measurement (left bottom).

6.4. Results and discussion

6.4.1. Resistivity analysis using Gaussian function and resistivity equation

To verify this measurement, Cu NWs (40 nm diameter, 45 μm length, and 107 nm interwire distance) electrodeposited in commercial AAO were measured 56 times as a preliminary test. A histogram of the measured data is shown in Figure 6.11.

To analyze the histograms in this work, Origin software was used for nonlinear curve fitting with customized Gaussian function that can detect up to three Gaussians,

$$y = y_0 + \frac{A_0}{w_0\sqrt{\pi/2}}\, e^{-2\frac{(x-x_{c_0})^2}{{w_0}^2}} + y_1 + \frac{A_1}{w_1\sqrt{\pi/2}}\, e^{-2\frac{(x-x_{c_1})^2}{{w_1}^2}} + y_2 + \frac{A_2}{w_2\sqrt{\pi/2}}\, e^{-2\frac{(x-x_{c_2})^2}{{w_2}^2}}$$

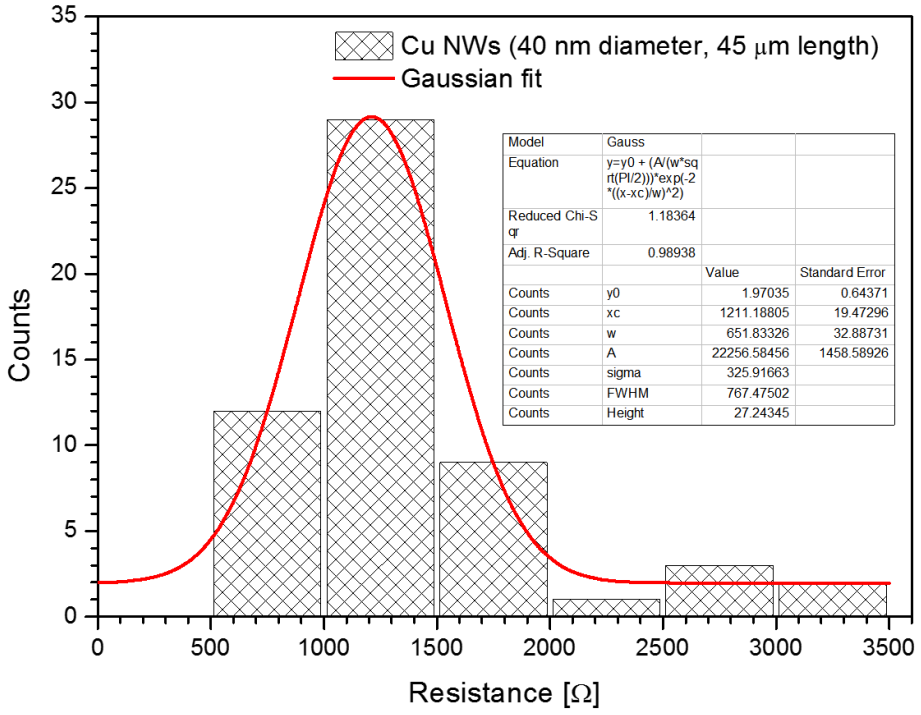

Model	Gauss		
Equation	y=y0 + (A/(w*sqrt(PI/2)))*exp(-2*((x-xc)/w)^2)		
Reduced Chi-Sqr	1.18364		
Adj. R-Square	0.98938		
		Value	Standard Error
Counts	y0	1.97035	0.64371
Counts	xc	1211.18805	19.47296
Counts	w	651.83326	32.88731
Counts	A	22256.58456	1458.58926
Counts	sigma	325.91663	
Counts	FWHM	767.47502	
Counts	Height	27.24345	

Figure 6.11. Histogram of DC resistance measurements for Cu NWs with 40 nm diameter and 45 μm length.

where y_0, y_1, and y_2 are offset, x_{c_0}, x_{c_1}, and x_{c_2} are center, w_0, w_1, and w_2 are full width at half maximum, and A_0, A_1, and A_2 are area. Histograms with the highest R-squared value (a statistical measure of how close the data are to the fitted line, $0 \leq R^2 \leq 1$) were used for analysis.

Resistivities in this work can be estimated using the measured resistance values and the relationship between them as shown in Figure 6.12.

In the preliminary test, an average resistance of Cu NWs with 40 nm diameter and 45 μm length was 1211.2 ± 325.9 Ω and estimated resistivity was 3.4 μΩ-cm, which is about twice that of bulk Cu (1.68 μΩ-cm). By doing the preliminary test measurements, it has been verified that this measurement method is reasonable and yields a fair histogram.

6.4.2. Resistivity analysis of Cu and Ni nanowires

Next, 500 measurements were made for 1.7 μm-long, 20 nm-diameter Cu NWs separated by 100 nm interwire distance. Ni NWs were measured 650 times, which have 1 μm-length, 20 nm-diameter, and 150 nm interwire distance. All measurements are shown in the histogram without binning, and it is clear that either 1 NW, 2 NWs, or more were contacted as shown in Figures 6.13

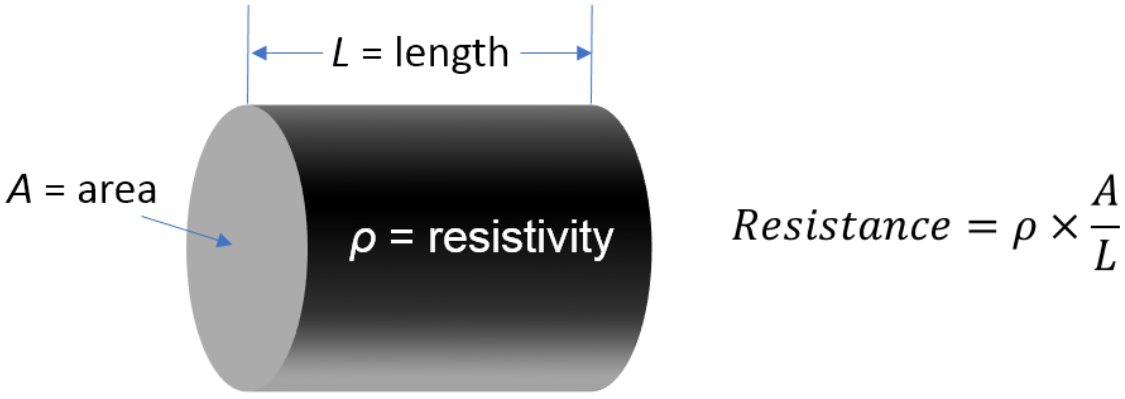

Figure 6.12. Resistance in a wire calculated with resistivity.

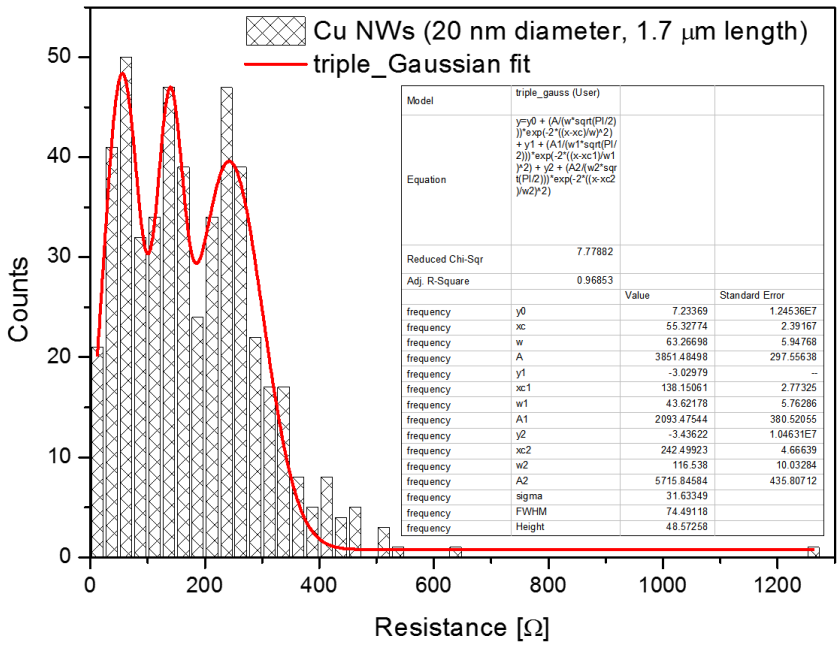

Model	triple_gauss (User)		
Equation	y=y0 + (A/(w*sqrt(PI/2)))*exp(-2*((x-xc)/w)^2) + y1 + (A1/(w1*sqrt(PI/2)))*exp(-2*((x-xc1)/w1)^2) + y2 + (A2/(w2*sqrt(PI/2)))*exp(-2*((x-xc2)/w2)^2)		
Reduced Chi-Sqr	7.77882		
Adj. R-Square	0.96853		
		Value	Standard Error
frequency	y0	7.23369	1.24536E7
frequency	xc	55.32774	2.39167
frequency	w	63.26698	5.94768
frequency	A	3851.48498	297.55638
frequency	y1	-3.02979	--
frequency	xc1	138.15061	2.77325
frequency	w1	43.62178	5.76286
frequency	A1	2093.47544	380.52055
frequency	y2	-3.43622	1.04631E7
frequency	xc2	242.49923	4.66639
frequency	w2	116.538	10.03284
frequency	A2	5715.84584	435.80712
frequency	sigma	31.63349	
frequency	FWHM	74.49118	
frequency	Height	48.57258	

Figure 6.13. Histogram of DC resistance measurements for Cu NWs with 20 nm diameter and 1.7 μm length.

and 6.14. Far-right peaks of both Cu and Ni NWs are for the case that single NWs were contacted, and only this case was considered for NW resistivity analysis.

An average resistance of Cu single NWs from the plot is 242.5 ± 58.3 Ω, which corresponds to an average resistivity of only 4.5 μΩ-cm, or about 2.7 times the bulk resistivity of Cu, 1.68 μΩ-cm. The grand challenge of interconnect resistivity exists because Cu interconnects can have resistivities that are one or two orders of magnitude higher than bulk when sidewalls cause scattering. The low resistivity found here is a repeatable result that has been measured before for 10 nm Cu NWs in AAO that is integrated onto Si, which is 5.4 μΩ-cm.[54] These diameters are smaller than the mean free path of the electrons in Cu (39 nm), which means AAO is an excellent host matrix for interconnects with good insulation and smooth channel surface.

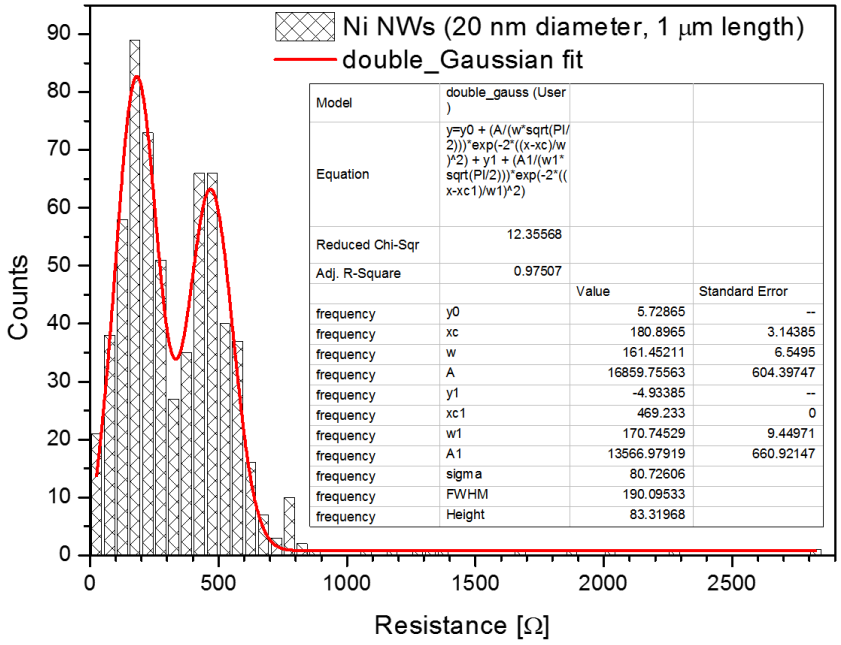

Model	double_gauss (User)		
Equation	y=y0 + (A/(w*sqrt(PI/2)))*exp(-2*((x-xc)/w)^2) + y1 + (A1/(w1*sqrt(PI/2)))*exp(-2*((x-xc1)/w1)^2)		
Reduced Chi-Sqr	12.35568		
Adj. R-Square	0.97507		
		Value	Standard Error
frequency	y0	5.72865	--
frequency	xc	180.8965	3.14385
frequency	w	161.45211	6.5495
frequency	A	16859.75563	604.39747
frequency	y1	-4.93385	--
frequency	xc1	469.233	0
frequency	w1	170.74529	9.44971
frequency	A1	13566.97919	660.92147
frequency	sigma	80.72606	
frequency	FWHM	190.09533	
frequency	Height	83.31968	

Figure 6.14. Histogram of DC resistance measurements for Ni NWs with 20 nm diameter and 1 μm length.

An average resistance of Ni single NWs from the plot is 469.2 ± 85.4 Ω. Using diameter and length, the estimated average resistivity of Ni NWs is 14.7 μΩ-cm, or about 2.1 times the bulk resistivity of Ni, 6.99 μΩ-cm.

Resistivity size effect stands out in NWs compared to bulk materials due to electron scattering from surfaces. A classical model to predict a resistivity considering the electron scattering at external surfaces is Fuchs and Sondheimer (FS) theory,

$$\rho = \rho_o \times (1 + \lambda \frac{3(1-p)}{4d})$$

where ρ_o is the bulk resistivity, λ is the mean free path of the electrons in bulk materials (39 nm for bulk Cu and 26 nm for bulk Ni, both values were experimentally determined), p is the surface scattering specularity, 0 (diffuse) – 1 (specular), a purely phenomenological parameter, and d is

the NW diameter.[54,128] By the FS theory, 20 nm-diameter Cu and Ni NWs would have resistivities of 4.1 μΩ-cm and 13.8 μΩ-cm, respectively. Our experimental values are slightly bigger than these values but are close to them. It is noted that FS theory cannot be used solely to estimate resistivities of nanosized interconnects because it underestimates the size effect and it is just one of many theories. Our measured resistivities are compared with the literature values from experiment and theory (simulation model) in Table 6.2.[54,128–134]

Our values are one or two orders of magnitude smaller than the experimental and even theoretical values in the literature. Using our measured resistivities and the value of Maqableh et al. (our research group), an experimental Cu NW resistivity trend was obtained as shown in Figure 6.15. This trend would be useful to estimate resistivities of Cu NWs with different diameters.

Table 6.2. Interconnect resistivity in the literature.[54,128–134]

Horizontal Nanowires					
Type	Resistivity (μΩ-cm)	Width (nm)	Height (nm)	Ref.	Data Type
Cu	4.5	40	230	Josell	Experiment
Cu	5	40	40	1 Steinhogl	Theory
Cu	3.75	50	50	2 Steinhogl	Experiment
Cu	6.3	40	40	Gall	Theory
Cu	13.8 - 141.3	20	40	Zhou	Theory
Cu	7.9 - 44.7	40	80	Zhou	Theory
Vertical Nanowires					
Type	Resistivity (μΩ-cm)	Diameter (nm)		Ref.	Data Type
Ni	1.15×10^4	20		Choi	Experiment
Cu	3.5	250		Xu	Experiment
Cu	5.4	10		Maqableh/Stadler	Experiment
Cu	3.4	40		This work	Experiment
Cu	4.5	20		This work	Experiment
Ni	14.7	20		This work	Experiment

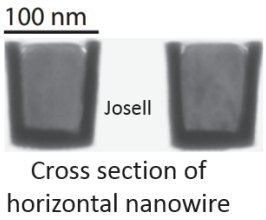

Cross section of horizontal nanowire

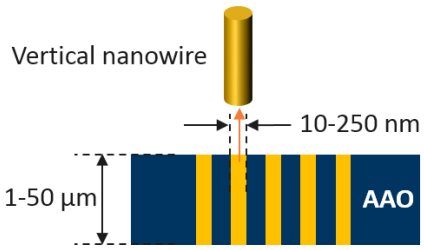

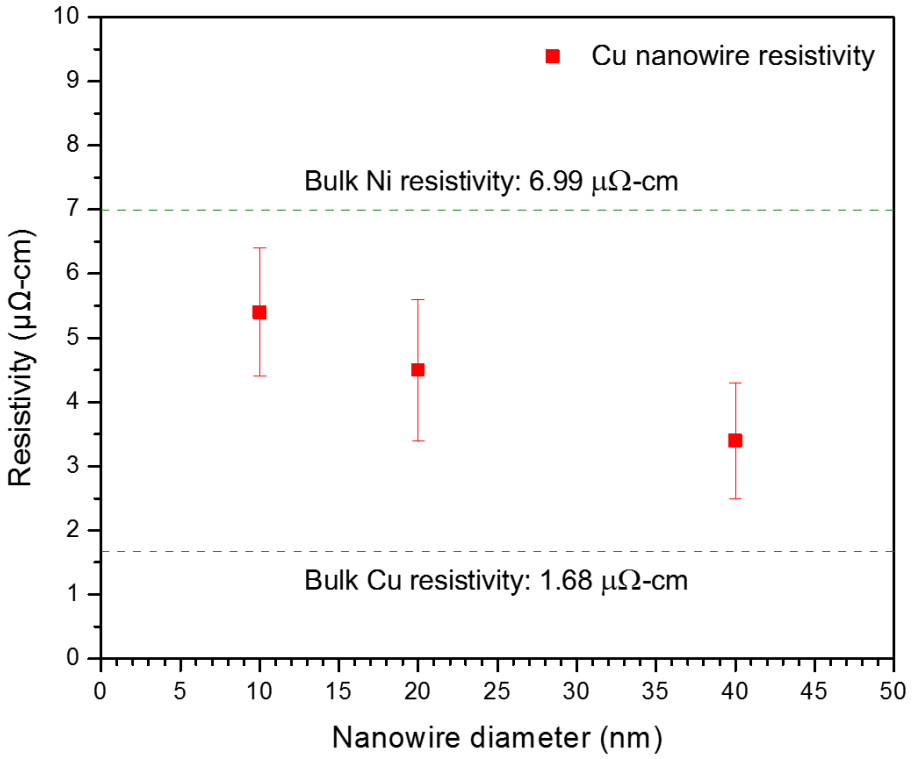

Figure 6.15. Experimental Cu NW resistivity trend with bulk Cu (red dashed line) and Ni (green dashed line) resistivities by Stadler-group at UMN.

6.5. Conclusions

DC resistance was measured for 20 nm-diameter Cu NWs (1.7 μm length) and Ni NWs (1 μm length) electrodeposited in AAO on Si using nanoprobes. Gaussian distributions and histograms of the measured data were used for statistical analysis. Estimated Cu NW's resistivity is 4.5 μΩ-cm based on Cu NW's average resistance of 242.5 Ω. Estimated Ni NW's resistivity is 14.7 μΩ-cm using Ni NW's average resistance of 469.2 Ω. These values are one or two orders of magnitude smaller than the literature values even though both NWs have diameters smaller than their experimental electron mean free path. This means that AAO has smooth channel surfaces and good insulation, thus an excellent host matrix for NW-based interconnects, and that NWs can

be applied as next-generation interconnects lowering power loss and RC delays. In addition, a trend of Cu NW resistivity was obtained based on this and previous works of our research group, which can be used as a guideline for further research about resistivities of Cu NWs with different diameters.

Chapter 7

Other nanowire-based applications

7.1. Magnetic nanowire-based circulators

Circulators are three-port passive devices whose primary function is to direct microwave signal flow within a circuit. They are a necessary element for communication, sensing, and detection devices. Conventional circulators require external magnets to set the magnetic field for nonreciprocal operation. This means that signal should go from port 1 to port 2 and the signal should not be reflected back from port 2 to port 1 at the same time. Otherwise, the original signal gets corrupted. Magnetic nanowire-based circulators, conversely, can operate without an external magnetic field because of the ability of magnetic nanowires to hold a magnetization direction due to their shape anisotropy.[86,98] Moreover, due to their tunability, integration capability, and the current high demand for small sized-devices, the nanowire-based circulators appear to be promising.

7.2. Exosome isolation using magnetic nanowires

Approximately 2 million Americans are diagnosed with cancer every year. Cancer, defined as abnormal cell growth with the potential to invade other parts of the body, has a high fatality rate and is typically characterized by the presence of tumors. Individual tumor cells secrete exosomes and these are called tumor-derived exosomes (TEX), which are membrane-bound

extracellular vesicles with a size range of 30-160 nm typically.[81,135–137] TEX can circulate freely in all body fluids and are used as cellular postmen that enable intercellular communication.[81,135–137] Currently, they are being studied as non-invasive biomarkers for early cancer detection and prognosis.[81,135–137] Unfortunately, current methods to isolate these TEX are expensive, require a long time and a laborious to provide results, and destroy the TEX in the process.[81,137] However, Nemati et al. simply utilized magnetic nanowires to isolate TEX without destroying their protein and RNA contents.[81,137] It is not yet clear how nanowires or nanowire fragments are internalized in TEX and how TEX attach to the nanowire surface. What is certain is that TEX can be tagged by magnetic nanowires and easily isolated by an external magnetic field of a magnet or a magnetic stand. Comparing TEX obtained by magnetic isolation using nanowires and conventional non-magnetic methods, the obtained TEX size distributions and yields in both cases were comparable, indicating that the magnetic isolation method can provide high TEX yields in a low-cost, efficient, and fast manner.[81,137] So, this method shows great promise in advancing cancer treatments by tracking cancer progression.

7.3. Ferrogels made of magnetic nanowires

A composite material composed of magnetic nanoparticles, nanorods, or nanowires embedded in a hydrogel matrix, a material similar to living tissue, is called FG (ferrogel).[85] FGs have attracted special attention in research fields where materials similar to natural tissues are required and utilized, such as regenerative medicine and magnetic biosensing, because they are sensitive to a magnetic field.[85] However, there are few studies on nanowire-based FGs compared to several studies on FGs containing spherical metal nanoparticles.[85] Also, unlike solid materials, methods for evaluating the structure of gels or FGs containing nanoparticles or nanorods and

nanowires have been much less studied.[85] So, there will be more work on FGs using nanomaterials such as magnetic nanowires.

Chapter 8

Summary and future work

8.1. Magnetic nanowire biolabels using ferromagnetic resonance identification

Nanomaterials have attracted attention from a variety of fields. For example, magnetic nanowires (MNWs) can be used to identify and/or distinguish objects using their magnetic signatures: first-order reversal curves, hysteresis curves, angle dependent coercivity, and ferromagnetic resonance (FMR). Among these, FMR is the fastest measurement, and it shows the potential to identify many high-frequency signatures simultaneously. In this work, Fe, Co, and Ni MNW samples were fabricated by template-assisted pulsed electrodeposition and were measured individually and in combination using an FMR identification (FMR-ID) labeling system. The FMR-ID system was then optimized using the FMR measurement results, the original and revised Kittel equations, and the magnetic properties of the MNWs. The most efficient FMR-ID detection was achieved with DC bias fields (0−15 kOe) that are parallel to the nanowires and microwave frequencies of 20 GHz or above. This MNW-based FMR-ID labeling system will be effective wherever small identification markers are needed beyond cell labeling.

To improve the MNW-based FMR-ID system, the following should be investigated. First, all the unexpected absorption nulls were either unsaturated or undefined. But it needs to be studied for clarification. Second, the absorption nulls with perpendicularly applied DC magnetic fields are so broad compared to those with parallel orientation in FMR measurements that it is hard to

distinguish them. It might be caused by broad field linewidths. Additional studies are required to figure out the reason of broad absorption nulls or field linewidths and to reduce them in order to achieve better sensitivity and detection in the system. Third, for various FMR signatures, it is good to try using many different types of nanowires made of ferromagnetic alloys or multilayered structures.

8.2. Fabrication of long-range ordered aluminum oxide and Fe/Au multilayered nanowires for 3-D magnetic memory

Large-scale long-range ordered anodic aluminum oxide and multilayered nanowires (NWs) are attractive to 3-D nanostructured material applications, such as high-density 3-D magnetic memory. This work demonstrated long-range ordered aluminum oxide made by simple and inexpensive double imprinting with the line-patterned stamp and uniform iron–gold multilayered NWs fabricated by galvanostatic electrochemical deposition with the single electrolyte bath. These two structural features show potential for future high-density recording systems that require long-range ordered devices separated from each other by insulation to eliminate crosstalk.

For this work to be widely applied, more work is needed on the anodization process. The mild anodization (MA) process used in this work usually has a slow AAO growth rate of 1–2 μm.[16,17] At this rate, it takes about more than one day to grow as thick as commercial AAO templates with 50 μm thickness. To increase the AAO growth rate, the hard anodization (HA) can be tried but it often produces severely burned or buckled surfaces with cracks and distorted pores, and it is very difficult to control the pore size, interpore distance, and the aspect ratio of the pores.[13] So, there is a need to develop a technique to grow AAO stably and rapidly.

8.3. Nanowire-based interconnects

In this work, vertical Cu nanowires have been shown to possess low electrical resistivity, compared to the literature values. To utilize their potential as nanowire-based interconnects for mm-wave and sub-mm-wave applications, this work presented the fabrication method for integrated nanoporous anodic aluminum oxide (AAO) on Si substrates and the DC resistance measurements and analysis of Cu and Ni nanowires grown in the AAO. Estimated resistivities of Cu and Ni nanowires with 20 nm-diameter were 4.5 μΩ-cm and 14.7 μΩ-cm, respectively. Also, a trend of Cu NW resistivity with diameter size was obtained.

Due to the nature of the thin AAOs integrated on Si substrates, it is difficult to have highly ordered pores, characteristic of AAOs made by two-step Al anodization. Therefore, if a simple method to fabricate the integrated AAOs on Si with highly ordered pore arrangement is developed, nanowire technology can be utilized more widely.

Bibliography

(1) Kuick Research. Global Nanoparticle Drug Delivery Market, Dosage, Price and Clinical Pipeline Outlook 2024 https://www.researchandmarkets.com/research/kn78v5/global_200?w=5.

(2) Pondman, K. M.; Maijenburg, A. W.; Celikkol, F. B.; Pathan, A. A.; Kishore, U.; Haken, B. ten; ten Elshof, J. E. Au Coated Ni Nanowires with Tuneable Dimensions for Biomedical Applications. *Journal of Materials Chemistry B* **2013**, *1* (44), 6129. https://doi.org/10.1039/c3tb20808g.

(3) Sharma, A.; Orlowski, G. M.; Zhu, Y.; Shore, D.; Kim, S. Y.; DiVito, M. D.; Hubel, A.; Stadler, B. J. H. Inducing Cells to Disperse Nickel Nanowires via Integrin-Mediated Responses. *Nanotechnology* **2015**, *26* (13), 135102. https://doi.org/10.1088/0957-4484/26/13/135102.

(4) Salem, A. K.; Searson, P. C.; Leong, K. W. Multifunctional Nanorods for Gene Delivery. *Nature Materials* **2003**, *2* (10), 668–671. https://doi.org/10.1038/nmat974.

(5) Hultgren, A.; Tanase, M.; Chen, C. S.; Meyer, G. J.; Reich, D. H. Cell Manipulation Using Magnetic Nanowires. *Journal of Applied Physics* **2003**, *93* (10), 7554–7556. https://doi.org/10.1063/1.1556204.

(6) Sharma, A.; Zhu, Y.; Thor, S.; Zhou, F.; Stadler, B.; Hubel, A. Magnetic Barcode Nanowires for Osteosarcoma Cell Control, Detection and Separation. *IEEE Trans. Magn.* **2013**, *49* (1), 453–456. https://doi.org/10.1109/TMAG.2012.2224647.

(7) IRDS. INTERNATIONAL ROADMAP FOR DEVICES AND SYSTEMS 2017 EDITION https://irds.ieee.org/images/files/pdf/2017/2017IRDS_MM.pdf.

(8) International Data Corporation. The Digitization of the World from Edge to Core https://www.seagate.com/files/www-content/our-story/trends/files/idc-seagate-dataage-whitepaper.pdf.

(9) Tewari, D.; Baul, S. 3D NAND Flash Memory Market https://www.alliedmarketresearch.com/3D-NAND-flash-memory-market.

(10) Stroeve, P.; Ileri, N. Biotechnical and Other Applications of Nanoporous Membranes. *Trends in Biotechnology* **2011**, *29* (6), 259–266. https://doi.org/10.1016/j.tibtech.2011.02.002.

(11) Apel, P.; Blonskaya, I.; Dmitriev, S.; Orelovitch, O.; Sartowska, B. Structure of Polycarbonate Track-Etch Membranes: Origin of the "Paradoxical" Pore Shape. *Journal of Membrane Science* **2006**, *282* (1–2), 393–400. https://doi.org/10.1016/j.memsci.2006.05.045.

(12) Prida, V. M.; Vega, V.; García, J.; Iglesias, L.; Hernando, B.; Minguez-Bacho, I. Electrochemical Methods for Template-Assisted Synthesis of Nanostructured Materials. In *Magnetic Nano- and Microwires*; Vázquez, M., Ed.; Elsevier, 2015; pp 3–39. https://doi.org/10.1016/B978-0-08-100164-6.00001-1.

(13) Lee, W.; Park, S.-J. Porous Anodic Aluminum Oxide: Anodization and Templated Synthesis of Functional Nanostructures. *Chem. Rev.* **2014**, *114* (15), 7487–7556. https://doi.org/10.1021/cr500002z.

(14) Tan, L. Templated Synthesis of Magnetic Nanowires by Electrochemical Deposition, University of Minnesota, 2008.

(15) Masuda, H.; Fukuda, K. Ordered Metal Nanohole Arrays Made by a Two-Step Replication of Honeycomb Structures of Anodic Alumina. *Science* **1995**, *268* (5216), 1466–1468. https://doi.org/10.1126/science.268.5216.1466.

(16) Lee, W.; Ji, R.; Gösele, U.; Nielsch, K. Fast Fabrication of Long-Range Ordered Porous Alumina Membranes by Hard Anodization. *Nature Materials* **2006**, *5* (9), 741–747. https://doi.org/10.1038/nmat1717.
(17) Um, J.; Zamani Kouhpanji, M. R.; Liu, S.; Nemati Porshokouh, Z.; Sung, S.-Y.; Kosel, J.; Stadler, B. Fabrication of Long-Range Ordered Aluminum Oxide and Fe/Au Multilayered Nanowires for 3-D Magnetic Memory. *IEEE Trans. Magn.* **2020**, *56* (2), 1–6. https://doi.org/10.1109/TMAG.2019.2942946.
(18) Ramazani, A.; Kashi, M. A.; Maleki, K.; Mohammadniaei, M. Self-Ordered Nanopore Arrays with 300–400 Nm Interpore Distances Formed by High Field Accelerated Mild Anodization. *Jpn. J. Appl. Phys.* **2011**, *50*, 035203. https://doi.org/10.1143/JJAP.50.035203.
(19) Yalçın, O. Ferromagnetic Resonance. In *Ferromagnetic Resonance - Theory and Applications*; Yalçın, O., Ed.; InTech, 2013. https://doi.org/10.5772/56134.
(20) Schönenberger, C.; van der Zande, B. M. I.; Fokkink, L. G. J.; Henny, M.; Schmid, C.; Krüger, M.; Bachtold, A.; Huber, R.; Birk, H.; Staufer, U. Template Synthesis of Nanowires in Porous Polycarbonate Membranes: Electrochemistry and Morphology. *J. Phys. Chem. B* **1997**, *101* (28), 5497–5505. https://doi.org/10.1021/jp963938g.
(21) Shin, S.; Kong, B.; Kim, B.; Kim, K.; Cho, H.; Cho, H. Over 95% of Large-Scale Length Uniformity in Template-Assisted Electrodeposited Nanowires by Subzero-Temperature Electrodeposition. *Nanoscale Res Lett* **2011**, *6* (1), 467. https://doi.org/10.1186/1556-276X-6-467.
(22) Reddy, K. S. M.; Park, J. J.; Na, S.-M.; Maqableh, M. M.; Flatau, A. B.; Stadler, B. J. H. Electrochemical Synthesis of Magnetostrictive Fe-Ga/Cu Multilayered Nanowire Arrays with Tailored Magnetic Response. *Advanced Functional Materials* **2011**, *21* (24), 4677–4683. https://doi.org/10.1002/adfm.201101390.
(23) Li, D.; Podlaha, E. Template-Assisted Electrodeposition of Fe-Ni-Co Nanowires: Effects of Electrolyte PH and Sodium Lauryl Sulfate. *J. Electrochem. Soc.* **2017**, *164* (13), D843–D851. https://doi.org/10.1149/2.0931713jes.
(24) Um, J.; Zhang, Y.; Zhou, W.; Zamani Kouhpanji, M. R.; Radu, C.; Franklin, R. R.; Stadler, B. J. H. Magnetic Nanowire Biolabels Using Ferromagnetic Resonance Identification. *ACS Appl. Nano Mater.* **2021**, *4* (4), 3557–3564. https://doi.org/10.1021/acsanm.1c00086.
(25) Darques, M.; Encinas, A.; Vila, L.; Piraux, L. Controlled Changes in the Microstructure and Magnetic Anisotropy in Arrays of Electrodeposited Co Nanowires Induced by the Solution PH. *Journal of Physics D: Applied Physics* **2004**, *37* (10), 1411–1416. https://doi.org/10.1088/0022-3727/37/10/001.
(26) Rose, I.; Whittington, C. *Nickel Plating Handbook*; Nickel Institute, 2014.
(27) Graham, L. M.; Cho, S.; Kim, S. K.; Noked, M.; Lee, S. B. Role of Boric Acid in Nickel Nanotube Electrodeposition: A Surface-Directed Growth Mechanism. *Chem. Commun.* **2014**, *50* (5), 527–529. https://doi.org/10.1039/C3CC47183G.
(28) Ji, J.; Cooper, W. C.; Dreisinger, D. B.; Peters, E. Surface PH Measurements during Nickel Electrodeposition. *J Appl Electrochem* **1995**, *25* (7), 642–650. https://doi.org/10.1007/BF00241925.
(29) Vibrating-sample magnetometer https://en.wikipedia.org/wiki/Vibrating-sample_magnetometer.
(30) O'handley, R. C. *Modern Magnetic Materials: Principles and Applications*; Wiley, 2000.

(31) McGary, P. D.; Stadler, B. J. H. Electrochemical Deposition of Fe1−xGax Nanowire Arrays. *Journal of Applied Physics* **2005**, *97* (10), 10R503. https://doi.org/10.1063/1.1851435.
(32) Stadler, B.; Reddy, M.; Basantkumar, R.; McGary, P.; Estrine, E.; Huang, X.; Sung, S.; Tan, L.; Zou, J.; Maqableh, M.; Shore, D.; Gage, T.; Um, J.; Hein, M.; Sharma, A. Galfenol Thin Films and Nanowires. *Sensors* **2018**, *18* (8), 2643. https://doi.org/10.3390/s18082643.
(33) Estrine, E. C.; Robbins, W. P.; Maqableh, M. M.; Stadler, B. J. H. Electrodeposition and Characterization of Magnetostrictive Galfenol (FeGa) Thin Films for Use in Microelectromechanical Systems. *Journal of Applied Physics* **2013**, *113* (17), 17A937. https://doi.org/10.1063/1.4799775.
(34) Estrine, E. C.; Hein, M.; Robbins, W. P.; Stadler, B. J. H. Composition and Crystallinity in Electrochemically Deposited Magnetostrictive Galfenol (FeGa). *Journal of Applied Physics* **2014**, *115* (17), 17A918. https://doi.org/10.1063/1.4865318.
(35) McGary, P. D.; Tan, L.; Zou, J.; Stadler, B. J. H.; Downey, P. R.; Flatau, A. B. Magnetic Nanowires for Acoustic Sensors (Invited). *Journal of Applied Physics* **2006**, *99* (8), 08B310. https://doi.org/10.1063/1.2167332.
(36) McGary, P. D.; Reddy, K. S. M.; Haugstad, G. D.; Stadler, B. J. H. Combinatorial Electrodeposition of Magnetostrictive Fe[Sub 1−x]Ga[Sub x]. *Journal of The Electrochemical Society* **2010**, *157* (12), D656. https://doi.org/10.1149/1.3497355.
(37) Reddy, K. S. M.; Estrine, E. C.; Lim, D.-H.; Smyrl, W. H.; Stadler, B. J. H. Controlled Electrochemical Deposition of Magnetostrictive Fe1−xGax Alloys. *Electrochemistry Communications* **2012**, *18*, 127–130. https://doi.org/10.1016/j.elecom.2012.02.039.
(38) Reddy, K. S. M.; Maqableh, M. M.; Stadler, B. J. H. Epitaxial $Fe_{(1-x)}Ga_{x}$/GaAs Structures via Electrochemistry for Spintronics Applications. *Journal of Applied Physics* **2012**, *111* (7), 07E502. https://doi.org/10.1063/1.3670514.
(39) Park, J. J.; Estrine, E. C.; Madhukar Reddy, S.; Stadler, B. J. H.; Flatau, A. B. Technique for Measurement of Magnetostriction in an Individual Nanowire Using Atomic Force Microscopy. *Journal of Applied Physics* **2014**, *115* (17), 17A919. https://doi.org/10.1063/1.4864433.
(40) Downey, P. R.; Flatau, A. B.; McGary, P. D.; Stadler, B. J. H. Effect of Magnetic Field on the Mechanical Properties of Magnetostrictive Iron-Gallium Nanowires. *Journal of Applied Physics* **2008**, *103* (7), 07D305. https://doi.org/10.1063/1.2837276.
(41) Grutter, A. J.; Krycka, K. L.; Tartakovskaya, E. V.; Borchers, J. A.; Reddy, K. S. M.; Ortega, E.; Ponce, A.; Stadler, B. J. H. Complex Three-Dimensional Magnetic Ordering in Segmented Nanowire Arrays. *ACS Nano* **2017**, *11* (8), 8311–8319. https://doi.org/10.1021/acsnano.7b03488.
(42) Ortega, E.; Reddy, S. M.; Betancourt, I.; Roughani, S.; Stadler, B. J. H.; Ponce, A. Magnetic Ordering in 45 Nm-Diameter Multisegmented FeGa/Cu Nanowires: Single Nanowires and Arrays. *Journal of Materials Chemistry C* **2017**, *5* (30), 7546–7552. https://doi.org/10.1039/C7TC02314F.
(43) Park, J. J.; Reddy, M.; Mudivarthi, C.; Downey, P. R.; Stadler, B. J. H.; Flatau, A. B. Characterization of the Magnetic Properties of Multilayer Magnetostrictive Iron-Gallium Nanowires. *Journal of Applied Physics* **2010**, *107* (9), 09A954. https://doi.org/10.1063/1.3359852.
(44) Park, J. J.; Reddy, M.; Stadler, B. J. H.; Flatau, A. B. Hysteresis Measurement of Individual Multilayered Fe-Ga/Cu Nanowires Using Magnetic Force Microscopy. *Journal of Applied Physics* **2013**, *113* (17), 17A331. https://doi.org/10.1063/1.4795818.

(45) Park, J. J.; Reddy, K. S. M.; Stadler, B.; Flatau, A. Magnetostrictive Fe–Ga/Cu Nanowires Array With GMR Sensor for Sensing Applied Pressure. *IEEE Sensors Journal* **2017**, *17* (7), 2015–2020. https://doi.org/10.1109/JSEN.2017.2657789.
(46) Reddy, K. S. M.; Jin Park, J.; Maqableh, M. M.; Flatau, A. B.; Stadler, B. J. H. Magnetization Reversal Mechanisms in 35-Nm Diameter $Fe_{1-x}Ga_x$/Cu Multilayered Nanowires. *Journal of Applied Physics* **2012**, *111* (7), 07A920. https://doi.org/10.1063/1.3673823.
(47) Sun, L.; Hao, Y.; Chien, C.-L.; Searson, P. C. Tuning the Properties of Magnetic Nanowires. *IBM Journal of Research and Development* **2005**, *49* (1), 79–102. https://doi.org/10.1147/rd.491.0079.
(48) Ghemes, A.; Dragos-Pinzaru, O.; Chiriac, H.; Lupu, N.; Grigoras, M.; Shore, D.; Stadler, B.; Tabakovic, I. Controlled Electrodeposition and Magnetic Properties of $Co_{35}Fe_{65}$ Nanowires with High Saturation Magnetization. *Journal of The Electrochemical Society* **2017**, *164* (2), D13–D22. https://doi.org/10.1149/2.0441702jes.
(49) Hein, M. A.; Maqableh, M. M.; Delahunt, M. J.; Tondra, M.; Flatau, A. B.; Shield, C. K.; Stadler, B. J. H. Fabrication of BioInspired Inorganic Nanocilia Sensors. *IEEE Trans. Magn.* **2013**, *49* (1), 191–196. https://doi.org/10.1109/TMAG.2012.2224852.
(50) Tan, L.; Stadler, B. J. H. Fabrication and Magnetic Behavior of Co/Cu Multilayered Nanowires. *Journal of Materials Research* **2006**, *21* (11), 2870–2875. https://doi.org/10.1557/jmr.2006.0348.
(51) Cantu-Valle, J.; Betancourt, I.; Sanchez, J. E.; Ruiz-Zepeda, F.; Maqableh, M. M.; Mendoza-Santoyo, F.; Stadler, B. J. H.; Ponce, A. Mapping the Magnetic and Crystal Structure in Cobalt Nanowires. *Journal of Applied Physics* **2015**, *118* (2), 024302. https://doi.org/10.1063/1.4923745.
(52) Tan, L.; McGary, P. D.; Stadler, B. J. H. Controlling the Angular Response of Magnetoresistance in Co/Cu Multilayered Nanowires Using Co Crystallographic Orientation. *Journal of Applied Physics* **2008**, *103* (7), 07B504. https://doi.org/10.1063/1.2829901.
(53) InRedox LLC. Data Sheet with Detailed Specifications for Standard Products.
(54) Maqableh, M. M.; Huang, X.; Sung, S.-Y.; Reddy, K. S. M.; Norby, G.; Victora, R. H.; Stadler, B. J. H. Low-Resistivity 10 Nm Diameter Magnetic Sensors. *Nano Letters* **2012**, *12* (8), 4102–4109. https://doi.org/10.1021/nl301610z.
(55) Maqableh, M. M.; Tan, L.; Huang, X.; Cobian, R.; Norby, G.; Victora, R. H.; Stadler, B. J. H. CPP GMR Through Nanowires. *IEEE Trans. Magn.* **2012**, *48* (5), 1744–1750. https://doi.org/10.1109/TMAG.2011.2174975.
(56) Sung, S.-Y.; Maqableh, M. M.; Huang, X.; Sai Madhukar Reddy, K.; Victora, R. H.; Stadler, B. J. H. Metallic 10 Nm Diameter Magnetic Sensors and Large-Scale Ordered Arrays. *IEEE Trans. Magn.* **2014**, *50* (11), 1–5. https://doi.org/10.1109/TMAG.2014.2325944.
(57) Darques, M.; Piraux, L.; Encinas, A. Influence of the Diameter and Growth Conditions on the Magnetic Properties of Cobalt Nanowires. *IEEE Transactions on Magnetics* **2005**, *41* (10), 3415–3417. https://doi.org/10.1109/TMAG.2005.855221.
(58) Hernández, S.; Tan, L.; Stadler, B. J. H.; Victora, R. H. Micromagnetic Calculation of Spin Transfer Torque in Co/Cu Multilayer Nanowires. *Journal of Applied Physics* **2011**, *109* (7), 07C916. https://doi.org/10.1063/1.3562924.
(59) Huang, X.; Tan, L.; Cho, H.; Stadler, B. J. H. Magnetoresistance and Spin Transfer Torque in Electrodeposited Co/Cu Multilayered Nanowire Arrays with Small

Diameters. *Journal of Applied Physics* **2009**, *105* (7), 07D128. https://doi.org/10.1063/1.3075990.
(60) Plouffe, B. D.; Murthy, S. K.; Lewis, L. H. Fundamentals and Application of Magnetic Particles in Cell Isolation and Enrichment: A Review. *Reports on Progress in Physics* **2015**, *78* (1), 016601. https://doi.org/10.1088/0034-4885/78/1/016601.
(61) Ventola, C. L. Progress in Nanomedicine: Approved and Investigational Nanodrugs. *Pharmacy and Therapeutics* **2017**, *42* (12), 742.
(62) Sharma, A.; DiVito, M. D.; Shore, D. E.; Block, A. D.; Pollock, K.; Solheid, P.; Feinberg, J. M.; Modiano, J.; Lam, C. H.; Hubel, A.; Stadler, B. J. H. Alignment of Collagen Matrices Using Magnetic Nanowires and Magnetic Barcode Readout Using First Order Reversal Curves (FORC) (Invited). *Journal of Magnetism and Magnetic Materials* **2018**, *459*, 176–181. https://doi.org/10.1016/j.jmmm.2017.11.035.
(63) Shore, D. E.; Dileepan, T.; Modiano, J. F.; Jenkins, M. K.; Stadler, B. J. H. Enrichment and Quantification of Epitope-Specific CD4+ T Lymphocytes Using Ferromagnetic Iron-Gold and Nickel Nanowires. *Sci Rep* **2018**, *8* (1), 15696. https://doi.org/10.1038/s41598-018-33910-0.
(64) Zhou, W.; Um, J.; Zhang, Y.; Nelson, A. P.; Nemati, Z.; Modiano, J.; Stadler, B.; Franklin, R. Development of a Biolabeling System Using Ferromagnetic Nanowires. *IEEE J. Electromagn. RF Microw. Med. Biol.* **2019**, *3* (2), 134–142. https://doi.org/10.1109/JERM.2018.2889049.
(65) Dobrotă, C.-I.; Stancu, A. What Does a First-Order Reversal Curve Diagram Really Mean? A Study Case: Array of Ferromagnetic Nanowires. *Journal of Applied Physics* **2013**, *113* (4), 043928. https://doi.org/10.1063/1.4789613.
(66) Sharma, M.; Pathak, S.; Sharm, M. FMR Measurements of Magnetic Nanostructures. In *Ferromagnetic Resonance - Theory and Applications*; Yalçın, O., Ed.; IntechOpen, 2013. https://doi.org/10.5772/56615.
(67) Shore, D.; Pailloux, S. L.; Zhang, J.; Gage, T.; Flannigan, D. J.; Garwood, M.; Pierre, V. C.; Stadler, B. J. H. Electrodeposited Fe and Fe–Au Nanowires as MRI Contrast Agents. *Chemical Communications* **2016**, *52* (85), 12634–12637. https://doi.org/10.1039/C6CC06991F.
(68) Shore, D.; Ghemes, A.; Dragos-Pinzaru, O.; Gao, Z.; Shao, Q.; Sharma, A.; Um, J.; Tabakovic, I.; Bischof, J. C.; Stadler, B. J. H. Nanowarming Using Au-Tipped $Co_{35}Fe_{65}$ Ferromagnetic Nanowires. *Nanoscale* **2019**, *11* (31), 14607–14615. https://doi.org/10.1039/C9NR01182J.
(69) Estrine, E. C.; Riemer, S.; Venkatasamy, V.; Stadler, B. J. H.; Tabakovic, I. Mechanism and Stability Study of Gold Electrodeposition from Thiosulfate-Sulfite Solution. *Journal of The Electrochemical Society* **2014**, *161* (12), D687–D696. https://doi.org/10.1149/2.0411412jes.
(70) Vargas-Estevez, C.; Blanquer, A.; Dulal, P.; Pérez del Real, R.; Duch, M.; Ibáñez, E.; Barrios, L.; Murillo, G.; Torras, N.; Nogués, C.; Stadler, B. J. H.; Plaza, J. A.; Esteve, J. Study of Galfenol Direct Cytotoxicity and Remote Microactuation in Cells. *Biomaterials* **2017**, *139*, 67–74. https://doi.org/10.1016/j.biomaterials.2017.05.049.
(71) Choi, J.; Nielsch, K.; Reiche, M.; Wehrspohn, R. B.; Gösele, U. Fabrication of Monodomain Alumina Pore Arrays with an Interpore Distance Smaller than the Lattice Constant of the Imprint Stamp. *Journal of Vacuum Science & Technology B: Microelectronics and Nanometer Structures* **2003**, *21* (2), 763. https://doi.org/10.1116/1.1556397.

(72) Zou, J.; Qi, X.; Tan, L.; Stadler, B. J. H. Large-Scale Ordering of Porous Si Using Anodic Aluminum Oxide Grown by Directed Self-Assembly. *Applied Physics Letters* **2006**, *89* (9), 093106. https://doi.org/10.1063/1.2337560.

(73) Pathak, R.; Joshi, S. Multi-Scale Modeling and Analysis of Nano-RFID Systems on HPC Setup. In *Contemporary Computing*; Ranka, S., Aluru, S., Buyya, R., Chung, Y.-C., Dua, S., Grama, A., Gupta, S. K. S., Kumar, R., Phoha, V. V., Eds.; Springer Berlin Heidelberg: Berlin, Heidelberg, 2009; pp 649–659.

(74) Kim, J.; Wang, Z.; Kim, W. S. Stretchable RFID for Wireless Strain Sensing With Silver Nano Ink. *IEEE Sensors J.* **2014**, *14* (12), 4395–4401. https://doi.org/10.1109/JSEN.2014.2335743.

(75) Singh, R.; Singh, E.; Nalwa, H. S. Inkjet Printed Nanomaterial Based Flexible Radio Frequency Identification (RFID) Tag Sensors for the Internet of Nano Things. *RSC Adv.* **2017**, *7* (77), 48597–48630. https://doi.org/10.1039/C7RA07191D.

(76) Farokhzad, O. C.; Langer, R. Impact of Nanotechnology on Drug Delivery. *ACS Nano* **2009**, *3* (1), 16–20. https://doi.org/10.1021/nn900002m.

(77) Kumar, C. S. S. R.; Mohammad, F. Magnetic Nanomaterials for Hyperthermia-Based Therapy and Controlled Drug Delivery. *Advanced Drug Delivery Reviews* **2011**, *63* (9), 789–808. https://doi.org/10.1016/j.addr.2011.03.008.

(78) Laurent, S.; Dutz, S.; Häfeli, U. O.; Mahmoudi, M. Magnetic Fluid Hyperthermia: Focus on Superparamagnetic Iron Oxide Nanoparticles. *Advances in Colloid and Interface Science* **2011**, *166* (1–2), 8–23. https://doi.org/10.1016/j.cis.2011.04.003.

(79) Park, J. H.; Yang, S. H.; Lee, J.; Ko, E. H.; Hong, D.; Choi, I. S. Nanocoating of Single Cells: From Maintenance of Cell Viability to Manipulation of Cellular Activities. *Advanced Materials* **2014**, *26* (13), 2001–2010. https://doi.org/10.1002/adma.201304568.

(80) Liu, C.; Stakenborg, T.; Peeters, S.; Lagae, L. Cell Manipulation with Magnetic Particles toward Microfluidic Cytometry. *Journal of Applied Physics* **2009**, *105* (10), 102014. https://doi.org/10.1063/1.3116091.

(81) Nemati, Z.; Zamani Kouhpanji, M. R.; Zhou, F.; Das, R.; Makielski, K.; Um, J.; Phan, M.-H.; Muela, A.; Fdez-Gubieda, M. L.; Franklin, R. R.; Stadler, B. J. H.; Modiano, J. F.; Alonso, J. Isolation of Cancer-Derived Exosomes Using a Variety of Magnetic Nanostructures: From Fe3O4 Nanoparticles to Ni Nanowires. *Nanomaterials* **2020**, *10* (9), 1662. https://doi.org/10.3390/nano10091662.

(82) Lewis, J. K.; Bischof, J. C.; Braslavsky, I.; Brockbank, K. G. M.; Fahy, G. M.; Fuller, B. J.; Rabin, Y.; Tocchio, A.; Woods, E. J.; Wowk, B. G.; Acker, J. P.; Giwa, S. The Grand Challenges of Organ Banking: Proceedings from the First Global Summit on Complex Tissue Cryopreservation. *Cryobiology* **2016**, *72* (2), 169–182. https://doi.org/10.1016/j.cryobiol.2015.12.001.

(83) Khosla, K.; Wang, Y.; Hagedorn, M.; Qin, Z.; Bischof, J. Gold Nanorod Induced Warming of Embryos from the Cryogenic State Enhances Viability. *ACS Nano* **2017**, *11* (8), 7869–7878. https://doi.org/10.1021/acsnano.7b02216.

(84) Rao, W.; Huang, H.; Wang, H.; Zhao, S.; Dumbleton, J.; Zhao, G.; He, X. Nanoparticle-Mediated Intracellular Delivery Enables Cryopreservation of Human Adipose-Derived Stem Cells Using Trehalose as the Sole Cryoprotectant. *ACS Applied Materials & Interfaces* **2015**, *7* (8), 5017–5028. https://doi.org/10.1021/acsami.5b00655.

(85) Safronov, A. P.; Stadler, B. J. H.; Um, J.; Zamani Kouhpanji, M. R.; Alonso Masa, J.; Galyas, A. G.; Kurlyandskaya, G. V. Polyacrylamide Ferrogels with Ni Nanowires. *Materials* **2019**, *12* (16), 2582. https://doi.org/10.3390/ma12162582.

(86) Zhou, W.; Um, J.; Stadler, B.; Franklin, R. Design of Self-Biased Coplanar Circulator with Ferromagnetic Nanowires. In *2018 IEEE Radio and Wireless Symposium (RWS)*; IEEE: Anaheim, CA, 2018; pp 240–242. https://doi.org/10.1109/RWS.2018.8304998.
(87) Um, J.; Park, J. J.; Flatau, A.; Zhou, W.; Zhang, Y.; Franklin, R.; Reddy, K. S. M.; Tan, L.; Sharma, A.; Sung, S.-Y.; Zou, J.; Stadler, B. 22 - Template-Assisted Electrodeposited Magnetic Nanowires and Their Properties for Applications. In *Magnetic Nano- and Microwires (Second Edition)*; Vázquez, M., Ed.; Woodhead Publishing Series in Electronic and Optical Materials; Woodhead Publishing, 2020; pp 675–695. https://doi.org/10.1016/B978-0-08-102832-2.00022-0.
(88) Zamani Kouhpanji, M. R.; Um, J.; Stadler, B. J. H. Demultiplexing of Magnetic Nanowires with Overlapping Signatures for Tagged Biological Species. *ACS Applied Nano Materials* **2020**, *3* (3), 3080–3087. https://doi.org/10.1021/acsanm.0c00593.
(89) Rodbell, D. S. Ferromagnetic Resonance of Iron Whisker Crystals. *Journal of Applied Physics* **1959**, *30* (4), S187–S188. https://doi.org/10.1063/1.2185880.
(90) Kambersky, V. Ferromagnetic Resonance in Iron Whiskers. *Can. J. Phys.* **1970**, *48* (9), 1103–1104. https://doi.org/10.1139/p70-142.
(91) Heinrich, B.; Arrott, A. S. Low Field Ferromagnetic Resonance in Iron Whiskers near Tc. *Journal of Magnetism and Magnetic Materials* **1983**, *31–34*, 669–671. https://doi.org/10.1016/0304-8853(83)90630-3.
(92) Ebels, U.; Duvail, J.-L.; Wigen, P. E.; Piraux, L.; Buda, L. D.; Ounadjela, K. Ferromagnetic Resonance Studies of Ni Nanowire Arrays. *Phys. Rev. B* **2001**, *64* (14), 144421. https://doi.org/10.1103/PhysRevB.64.144421.
(93) Encinas-Oropesa, A.; Demand, M.; Piraux, L.; Huynen, I.; Ebels, U. Dipolar Interactions in Arrays of Nickel Nanowires Studied by Ferromagnetic Resonance. *Phys. Rev. B* **2001**, *63* (10), 104415. https://doi.org/10.1103/PhysRevB.63.104415.
(94) Demand, M.; Encinas-Oropesa, A.; Kenane, S.; Ebels, U.; Huynen, I.; Piraux, L. Ferromagnetic Resonance Studies of Nickel and Permalloy Nanowire Arrays. *Journal of Magnetism and Magnetic Materials* **2002**, *249* (1–2), 228–233. https://doi.org/10.1016/S0304-8853(02)00535-8.
(95) Yalçın, O.; Yıldız, F.; Özdemir, M.; Aktaş, B.; Köseoğlu, Y.; Bal, M.; Tuominen, M. T. Ferromagnetic Resonance Studies of Co Nanowire Arrays. *Journal of Magnetism and Magnetic Materials* **2004**, *272–276*, 1684–1685. https://doi.org/10.1016/j.jmmm.2003.12.561.
(96) Darques, M.; Bogaert, A.-S.; Elhoussine, F.; Michotte, S.; De la Torre Medina, J.; Encinas, A.; Piraux, L. Controlled Growth of CoCu Nanowires and Application to Multilayered CoCu/Cu Nanowires with Selected Anisotropy. *Journal of Physics D: Applied Physics* **2006**, *39* (23), 5025–5032. https://doi.org/10.1088/0022-3727/39/23/019.
(97) Yamaguchi, A.; Motoi, K.; Hirohata, A.; Miyajima, H.; Miyashita, Y.; Sanada, Y. Broadband Ferromagnetic Resonance of Ni 81 Fe 19 Wires Using a Rectifying Effect. *Phys. Rev. B* **2008**, *78* (10), 104401. https://doi.org/10.1103/PhysRevB.78.104401.
(98) Darques, M.; Spiegel, J.; De la Torre Medina, J.; Huynen, I.; Piraux, L. Ferromagnetic Nanowire-Loaded Membranes for Microwave Electronics. *Journal of Magnetism and Magnetic Materials* **2009**, *321* (14), 2055–2065. https://doi.org/10.1016/j.jmmm.2008.03.060.
(99) Kartopu, G.; Yalçın, O.; Kazan, S.; Aktaş, B. Preparation and FMR Analysis of Co Nanowires in Alumina Templates. *Journal of Magnetism and Magnetic Materials* **2009**, *321* (9), 1142–1147. https://doi.org/10.1016/j.jmmm.2008.10.039.

(100) Carignan, L.-P.; Boucher, V.; Kodera, T.; Caloz, C.; Yelon, A.; Ménard, D. Double Ferromagnetic Resonance in Nanowire Arrays. *Applied Physics Letters* **2009**, *95* (6), 062504. https://doi.org/10.1063/1.3194296.
(101) Kraus, L.; Infante, G.; Frait, Z.; Vázquez, M. Ferromagnetic Resonance in Microwires and Nanowires. *Phys. Rev. B* **2011**, *83* (17), 174438. https://doi.org/10.1103/PhysRevB.83.174438.
(102) Yuan, L.; Meng, S.; Shi, Y.; Zhang, Y.; Yue, Z.; Li, L. Dual Band Microwave Ferromagnetic Resonance Absorption in Annealed Cobalt Nanowire Arrays. *Applied Physics Letters* **2014**, *105* (18), 182407. https://doi.org/10.1063/1.4901271.
(103) Aphesteguy, J.; Jacobo, S.; Lezama, L.; Kurlyandskaya, G.; Schegoleva, N. Microwave Resonant and Zero-Field Absorption Study of Doped Magnetite Prepared by a Co-Precipitation Method. *Molecules* **2014**, *19* (6), 8387–8401. https://doi.org/10.3390/molecules19068387.
(104) Aslam, S.; Khanna, M.; Kuanr, B. K.; Celinski, Z. One Dimensional $Fe_x Co_{1-x}$ Nanowires; Ferromagnetic Resonance and Magnetization Dynamics. *AIP Advances* **2017**, *7* (5), 056027. https://doi.org/10.1063/1.4977724.
(105) Kraus, L.; Lynnyk, A.; Azamat, D.; Drahokoupil, J.; Kopeček, J.; Rameš, M. Multi-Peak Ferromagnetic Resonance in Co Nanowires Array. *Journal of Magnetism and Magnetic Materials* **2017**, *421*, 241–249. https://doi.org/10.1016/j.jmmm.2016.08.018.
(106) Zhang, Y.; Um, J.; Zhou, W.; Stadler, B.; Franklin, R. Magnetic Nanowires for RF Applications: Ferromagnetic Resonance and Permeability Characterization. In *2019 IEEE MTT-S International Microwave Symposium (IMS)*; IEEE: Boston, MA, USA, 2019; pp 1100–1103. https://doi.org/10.1109/MWSYM.2019.8700826.
(107) Kittel, C. On the Theory of Ferromagnetic Resonance Absorption. *Physical Review* **1948**, *73* (2), 155–161. https://doi.org/10.1103/PhysRev.73.155.
(108) Schoen, M. A. W.; Lucassen, J.; Nembach, H. T.; Silva, T. J.; Koopmans, B.; Back, C. H.; Shaw, J. M. Magnetic Properties of Ultrathin 3 d Transition-Metal Binary Alloys. I. Spin and Orbital Moments, Anisotropy, and Confirmation of Slater-Pauling Behavior. *Phys. Rev. B* **2017**, *95* (13), 134410. https://doi.org/10.1103/PhysRevB.95.134410.
(109) Ivanov, Y. P.; Chuvilin, A.; Lopatin, S.; Kosel, J. Modulated Magnetic Nanowires for Controlling Domain Wall Motion: Toward 3D Magnetic Memories. *ACS Nano* **2016**, *10* (5), 5326–5332. https://doi.org/10.1021/acsnano.6b01337.
(110) Agramunt-Puig, S.; Del-Valle, N.; Pellicer, E.; Zhang, J.; Nogués, J.; Navau, C.; Sanchez, A.; Sort, J. Modeling the Collective Magnetic Behavior of Highly-Packed Arrays of Multi-Segmented Nanowires. *New Journal of Physics* **2016**, *18* (1), 013026. https://doi.org/10.1088/1367-2630/18/1/013026.
(111) Masuda, H.; Yamada, H.; Satoh, M.; Asoh, H.; Nakao, M.; Tamamura, T. Highly Ordered Nanochannel-Array Architecture in Anodic Alumina. *Applied Physics Letters* **1997**, *71* (19), 2770–2772. https://doi.org/10.1063/1.120128.
(112) Lee, J. H.; Wu, J. H.; Liu, H. L.; Cho, J. U.; Cho, M. K.; An, B. H.; Min, J. H.; Noh, S. J.; Kim, Y. K. Iron–Gold Barcode Nanowires. *Angewandte Chemie International Edition* **2007**, *46* (20), 3663–3667. https://doi.org/10.1002/anie.200605136.
(113) Cho, J. U.; Wu, J.-H.; Min, J. H.; Lee, J. H.; Liu, H.-L.; Kim, Y. K. Effect of Field Deposition and Pore Size on Co/Cu Barcode Nanowires by Electrodeposition. *Journal of Magnetism and Magnetic Materials* **2007**, *310* (2), 2420–2422. https://doi.org/10.1016/j.jmmm.2006.10.809.

(114) Jeon, I. T.; Yoon, S. J.; Kim, B. G.; Lee, J. S.; An, B. H.; Ju, J.-S.; Wu, J. H.; Kim, Y. K. Magnetic NiFe/Au Barcode Nanowires with Self-Powered Motion. *Journal of Applied Physics* **2012**, *111* (7), 07B513. https://doi.org/10.1063/1.3676062.
(115) Kim, B. G.; Yoon, S. J.; Jeon, I. T.; Kim, K. H.; Wu, J. H.; Kim, Y. K. Dimensional Dependence of Magnetic Properties in Arrays of CoFe/Au Barcode Nanowire. *IEEE Transactions on Magnetics* **2012**, *48* (11), 3929–3932. https://doi.org/10.1109/TMAG.2012.2202101.
(116) García, J.; Vega, V.; Iglesias, L.; Prida, V. M.; Hernando, B.; Barriga-Castro, E. D.; Mendoza-Reséndez, R.; Luna, C.; Görlitz, D.; Nielsch, K. Template-Assisted Co-Ni Alloys and Multisegmented Nanowires with Tuned Magnetic Anisotropy: Co-Ni Alloys and Multisegmented NWs with Tuned Magnetic Anisotropy. *physica status solidi (a)* **2014**, *211* (5), 1041–1047. https://doi.org/10.1002/pssa.201300731.
(117) Özkale, B.; Shamsudhin, N.; Chatzipirpiridis, G.; Hoop, M.; Gramm, F.; Chen, X.; Martí, X.; Sort, J.; Pellicer, E.; Pané, S. Multisegmented FeCo/Cu Nanowires: Electrosynthesis, Characterization, and Magnetic Control of Biomolecule Desorption. *ACS Applied Materials & Interfaces* **2015**, *7* (13), 7389–7396. https://doi.org/10.1021/acsami.5b01143.
(118) Serrà, A.; Vázquez-Mariño, G.; García-Torres, J.; Bosch, M.; Vallés, E. Magnetic Actuation of Multifunctional Nanorobotic Platforms to Induce Cancer Cell Death. *Advanced Biosystems* **2018**, *2* (2), 1700220. https://doi.org/10.1002/adbi.201700220.
(119) Marozzi, C. A.; Chialvo, A. C. Development of Electrode Morphologies of Interest in Electrocatalysis. Part 1: Electrodeposited Porous Nickel Electrodes. *Electrochimica Acta* **2000**, *45* (13), 2111–2120. https://doi.org/10.1016/S0013-4686(99)00422-3.
(120) Azevedo, J.; Sousa, C. T.; Mendes, A.; Araújo, J. P. Influence of the Rest Pulse Duration in Pulsed Electrodeposition of Fe Nanowires. *Journal of Nanoscience and Nanotechnology* **2012**, *12* (12), 9112–9117. https://doi.org/10.1166/jnn.2012.6769.
(121) Jang, B.; Pellicer, E.; Guerrero, M.; Chen, X.; Choi, H.; Nelson, B. J.; Sort, J.; Pané, S. Fabrication of Segmented Au/Co/Au Nanowires: Insights in the Quality of Co/Au Junctions. *ACS Applied Materials & Interfaces* **2014**, *6* (16), 14583–14589. https://doi.org/10.1021/am5038998.
(122) Pasternack. Skin Depth Calculator https://www.pasternack.com/t-calculator-skin-depth.aspx.
(123) Rabin, O.; Herz, P. R.; Lin, Y.-M.; Akinwande, A. I.; Cronin, S. B.; Dresselhaus, M. S. Formation of Thick Porous Anodic Alumina Films and Nanowire Arrays on Silicon Wafers and Glass. *Adv. Funct. Mater.* **2003**, *13* (8), 631–638. https://doi.org/10.1002/adfm.200304394.
(124) Holubowitch, N.; Nagle, L. C.; Rohan, J. F. Porous Alumina Thin Films on Conductive Substrates for Templated 1-Dimensional Nanostructuring. *Solid State Ionics* **2012**, *216*, 110–113. https://doi.org/10.1016/j.ssi.2012.03.016.
(125) Oh, J.; Thompson, C. V. Selective Barrier Perforation in Porous Alumina Anodized on Substrates. *Adv. Mater.* **2008**, *20* (7), 1368–1372. https://doi.org/10.1002/adma.200701719.
(126) Tian, M.; Xu, S.; Wang, J.; Kumar, N.; Wertz, E.; Li, Q.; Campbell, P. M.; Chan, M. H. W.; Mallouk, T. E. Penetrating the Oxide Barrier in Situ and Separating Freestanding Porous Anodic Alumina Films in One Step. *Nano Lett.* **2005**, *5* (4), 697–703. https://doi.org/10.1021/nl0501112.
(127) Al-Maqablah, M. M. Magnetic Multilayered Nanowires by Electrodeposition for Spintronic Applications, University of Minnesota, 2013.

(128) Gall, D. The Search for the Most Conductive Metal for Narrow Interconnect Lines. *Journal of Applied Physics* **2020**, *127* (5), 050901. https://doi.org/10.1063/1.5133671.
(129) Josell, D.; Brongersma, S. H.; Tőkei, Z. Size-Dependent Resistivity in Nanoscale Interconnects. *Annu. Rev. Mater. Res.* **2009**, *39* (1), 231–254. https://doi.org/10.1146/annurev-matsci-082908-145415.
(130) Steinhögl, W.; Schindler, G.; Steinlesberger, G.; Engelhardt, M. Size-Dependent Resistivity of Metallic Wires in the Mesoscopic Range. *Phys. Rev. B* **2002**, *66* (7), 075414. https://doi.org/10.1103/PhysRevB.66.075414.
(131) Steinhögl, W.; Schindler, G.; Steinlesberger, G.; Traving, M.; Engelhardt, M. Comprehensive Study of the Resistivity of Copper Wires with Lateral Dimensions of 100 Nm and Smaller. *Journal of Applied Physics* **2005**, *97* (2), 023706. https://doi.org/10.1063/1.1834982.
(132) Zhou, T.; Lanzillo, N. A.; Bhosale, P.; Gall, D.; Quon, R. A First-Principles Analysis of Ballistic Conductance, Grain Boundary Scattering and Vertical Resistance in Aluminum Interconnects. *AIP Advances* **2018**, *8* (5), 055127. https://doi.org/10.1063/1.5027084.
(133) Choi, D. S.; Rheem, Y.; Yoo, B.; Myung, N. V.; Kim, Y. K. I–V Characteristics of a Vertical Single Ni Nanowire by Voltage-Applied Atomic Force Microscopy. *Current Applied Physics* **2010**, *10* (4), 1037–1040. https://doi.org/10.1016/j.cap.2009.12.036.
(134) Xu, W.-H.; Wang, L.; Guo, Z.; Chen, X.; Liu, J.; Huang, X.-J. Copper Nanowires as Nanoscale Interconnects: Their Stability, Electrical Transport, and Mechanical Properties. *ACS Nano* **2015**, *9* (1), 241–250. https://doi.org/10.1021/nn506583e.
(135) Whiteside, T. L. The Potential of Tumor-Derived Exosomes for Noninvasive Cancer Monitoring: An Update. *Expert Review of Molecular Diagnostics* **2018**, *18* (12), 1029–1040. https://doi.org/10.1080/14737159.2018.1544494.
(136) Hofmann, L.; Ludwig, S.; Vahl, J. M.; Brunner, C.; Hoffmann, T. K.; Theodoraki, M.-N. The Emerging Role of Exosomes in Diagnosis, Prognosis, and Therapy in Head and Neck Cancer. *IJMS* **2020**, *21* (11), 4072. https://doi.org/10.3390/ijms21114072.
(137) Nemati, Z.; Um, J.; Zamani Kouhpanji, M. R.; Zhou, F.; Gage, T.; Shore, D.; Makielski, K.; Donnelly, A.; Alonso, J. Magnetic Isolation of Cancer-Derived Exosomes Using Fe/Au Magnetic Nanowires. *ACS Appl. Nano Mater.* **2020**, *3* (2), 2058–2069. https://doi.org/10.1021/acsanm.0c00263.